



HAL
open science

Characterization of heavy precipitation on Corsica

Phillip Scheffknecht

► **To cite this version:**

Phillip Scheffknecht. Characterization of heavy precipitation on Corsica. Climatology. Université Paul Sabatier - Toulouse III, 2016. English. NNT : 2016TOU30339 . tel-01767474

HAL Id: tel-01767474

<https://theses.hal.science/tel-01767474>

Submitted on 16 Apr 2018

HAL is a multi-disciplinary open access archive for the deposit and dissemination of scientific research documents, whether they are published or not. The documents may come from teaching and research institutions in France or abroad, or from public or private research centers.

L'archive ouverte pluridisciplinaire **HAL**, est destinée au dépôt et à la diffusion de documents scientifiques de niveau recherche, publiés ou non, émanant des établissements d'enseignement et de recherche français ou étrangers, des laboratoires publics ou privés.



THÈSE

En vue de l'obtention du

DOCTORAT DE L'UNIVERSITÉ DE TOULOUSE

Délivré par : *l'Université Toulouse 3 Paul Sabatier (UT3 Paul Sabatier)*

Présentée et soutenue le *25/11/2016* par :
Phillip SCHEFFKNECHT

Characterization of Heavy Precipitation on Corsica

JURY

SYLVAIN COQUILLAT
SILVIO DAVOLIO
DANIEL KIRSHBAUM

CHANTAL CLAUD
VÉRONIQUE DUCROCQ

LA, Toulouse
ISAC-CNR, Bologna
McGill University,
Montréal
LMD, Paris
CNRM-GAME, Toulouse

President du Jury
Rapporteur
Rapporteur
Examinatrice
Invitée

École doctorale et spécialité :

SDU2E : Océan, Atmosphère, Climat

Unité de Recherche :

Laboratoire d'Aérodologie (UMR 5560)

Directeur(s) de Thèse :

Dominique LAMBERT et Evelyne RICHARD

Rapporteurs :

Silvio Davolio et Daniel Kirshbaum

Karin, this is for you

Acknowledgements

First of all, I want to thank my supervisors Dr. Evelyne Richard and Dr. Dominique Lambert, who guided my work throughout this large endeavor. Thank you for the tips, the help and the guidance but also thank you for the funny moments we had during our meetings and for all the help during my early time in Toulouse. Special thanks to Evelyne for giving me my first home away from home in her house when I arrived in France. And thank you to Dominique for sending me on a trip to Corsica, so I could see the island about which I was writing for more than three years.

I would like to thank the members of my jury, starting with the president Prof. Sylvain Cocquillat. I thank Dr. Silvio Davolio and Prof. Daniel Kirshbaum for reviewing and evaluating my thesis. Their comments helped to further improve the manuscript for this final version. Thanks to the jury members Dr. Claude Chantal and Dr. Véronique Ducrocq as well as the members of my comité de thèse, Dr. Véronique Ducrocq and Dr. Andreas Wieser, who provided additional guidance.

Thanks to Prof. Daniel Kirshbaum for supervising my internship at McGill University in Montreal, which was a great experience. Special thanks to his wife, Rachel Shafts, without whom I might never have made it through the the bureaucracy of the immigration process. Also, thank you to the anonymous Canadian customs officer at the Montreal airport who decided to give me my work permit on the spot instead of sending me back home, when I arrived in Canada before having received the official work permit.

Thank you to Thibaut Dauhut for the countless discussions, great evenings and the visit in Montreal. I met him as a colleague but he became a good friend. Thank you to those who shared my office, Michaël Faivre, Allan Hally, and Daria Kuznetzova for the discussions, on and off-topic. Thanks to Thibaut Dauhut and

Jean-François Ribaud for helping me with buying and building all my furniture and thanks to David Baqué for helping me to move twice.

In addition, I want to thank the two Meso-NH wizards at the Laboratoire d'Aérodologie, Juan Escobar and Didier Gazin, as well as Christine Lac, Gaëlle Delautier and Soline Bielli from Meso-NH support for patiently answering all my questions. Thank you to all Ph.D. students, post-docs, permanents and others with whom I shared a beautiful time at the Laboratoire d'Aérodologie and in Toulouse and thank you all for the beautiful gifts I received on the day of my defense.

I thank my parents and my brother for supporting me through all my life and all my decisions, and last but not most of all I want to thank my girlfriend, Karin. I left you to live abroad for 1251 days, yet you, Karin, kept supporting me. You are everything I could ever wish for!

Contents

Résumé de l'introduction en français	1
Contexte géographique	2
Contexte géographique	3
Objectifs du travail et plan de la thèse	4
1 General Introduction	5
1.1 Geographical Context - The Mediterranean Basin	6
1.2 The HyMeX Program	9
1.3 Numerical Weather Prediction	11
1.3.1 The Beginning of Numerical Weather Prediction	11
1.3.2 Atmospheric Scales - Synoptic, Meso- and Microscale	13
1.4 The Physics of Heavy Precipitation Events	15
1.4.1 Convective Instability	15
1.4.2 Orography and its Effect on Air Flow and Precipitation	19
1.4.3 Heavy Precipitation Events in the Mediterranean	23
1.4.4 Heavy Precipitation Events over Corsica	27
1.5 Goals and Outline of this Thesis	29
2 Climatology of Rainfall on Corsica	31
2.1 The Climate of the Mediterranean	32

2.2	Methodology	35
2.2.1	EOFs and Principal Components	35
2.2.2	The <i>k</i> -means algorithm	36
2.3	Seasonal Distribution, Frequency and Composite Fields	38
2.4	EOFs	40
2.5	Clusters	42
2.6	Physical Interpretation of the Clusters	44
2.6.1	Mean Fields	44
2.6.2	Precipitation Distribution	48
2.7	Discussion	52
2.8	Conclusions	54
3	Numerical Tools and Used Observations	57
3.1	Meso-NH Simulations	57
3.1.1	Model Configuration	57
3.1.2	Simulation Ensembles	59
3.1.3	Experiments with Modified Orography	62
3.2	Observational Data and Comparison Methods	63
3.2.1	Precipitation - Surface Stations and Radar	64
3.2.2	Satellite Data	66
3.2.3	Radiosoundings	67
3.3	Statistical Methods	68
3.4	A Simple Cyclone Tracking Algorithm	72
4	Case 1: 4 September 2012 - A Quasi-Stationary Cyclone	75
4.1	Synoptic Situation	75
4.2	Observed Evolution	78
4.2.1	Satellite Images	78

4.2.2	Observed Precipitation	78
4.3	Initial Condition Ensemble	83
4.3.1	Spatial Distribution of 24 Hour Accumulated Precipitation	83
4.3.2	Quantitative Precipitation Verification	87
4.4	Cyclone Tracks	91
4.5	Evolution of the HPE in the Reference Simulation	94
4.6	Sensitivity to Horizontal Grid Spacing	96
4.6.1	Impact on Precipitation Distribution	97
4.6.2	Convergence Zones	99
4.7	Test over Flat Orography	102
4.8	Conclusions	103
5	Case 2: 31 October 2012 (IOP 18) - A Fast Moving Cyclone	105
5.1	Synoptic Situation	105
5.2	Observed Evolution	108
5.2.1	Satellite Images	108
5.2.2	Observed Precipitation	108
5.3	Initial Condition Ensemble	112
5.3.1	Spatial Distribution of 24 Hour Accumulated Precipitation	112
5.4	Quantitative Precipitation Verification	117
5.5	Cyclone Tracks	120
5.6	San Giuliano Radiosoundings	122
5.7	Evolution of the HPE in the Reference Simulation	126
5.8	High Resolution Simulation	129
5.8.1	Impact on Precipitation Distribution	129
5.9	Test over Flat Orography	131
5.10	Conclusions	133

6	Case 3: 23 October 2012 (IOP 15c) - A Highly Localized Convective Event	135
6.1	Synoptic Situation	136
6.2	Observed Evolution	137
6.2.1	Satellite Images	137
6.2.2	Observed Precipitation	139
6.3	Predictability and Sensitivity to Input Data Set and Initialization Time	141
6.4	High Resolution Simulations	146
6.4.1	Qualitative Comparison and Evolution of the HPE	148
6.4.2	Impact of the Mixing Length Formulation	154
6.5	Sensitivity to physical parametrizations	161
6.6	Physical Process Study	164
6.6.1	Analysis Departures	164
6.6.2	Role of the Corsican Orography	169
6.6.3	Role of the Gap Flows	171
6.7	Quantitative Precipitation Verification	173
6.8	Conclusions	175
7	Conclusions and Outlook	179
7.1	Results	179
7.1.1	Climatology and Clustering	179
7.1.2	Results of the Case Studies	181
7.2	Outlook	184
	Résumé de la conclusion en français	187
	Climatologie et classification des épisodes précipitants	187
	Études de cas	189

Perspectives 190

Résumé de l'introduction en français

La pluie est essentielle pour la vie en général et les humains en particulier. Tout au long de l'histoire les centres de civilisation se sont implantés près des rivières, des fleuves, des lacs ou de la mer. Bien que la présence d'eau réponde à un besoin élémentaire, elle est en même temps un facteur de risque. Les précipitations intenses - et les inondations qui en découlent - causent régulièrement d'importants dégâts matériels, voire de nombreuses victimes. Il est donc important de bien comprendre les processus physiques impliqués dans ces événements afin de mieux les prévoir et de permettre aux populations concernées de prendre les précautions nécessaires.

De telles préoccupations sont au coeur du programme de recherche international HyMeX (Hydrological Cycle of the Mediterranean Experiment)¹ dédié à l'étude du cycle hydrologique dans le bassin méditerranéen (Drobinski et al., 2014). En France, HyMeX constitue une des composantes du meta-programme MISTRALS² (Mediterranean Integrated STudies at Regional And Local Scales). Durant l'automne 2012, la communauté HyMeX a organisé une vaste campagne de mesures spécifiquement consacrée aux précipitations intenses (Ducrocq et al.,

¹<http://www.hymex.org>

²<http://www.mistrals-home.org>

2014). Celle-ci a permis de documenter de nombreux évènements ayant affecté les côtes espagnoles, françaises et italiennes

Les travaux menés dans cette thèse s’inscrivent dans le cadre général d’HyMeX. Ils sont focalisés sur les évènements précipitants intenses qui affectent la Corse. Ceux-ci possèdent en effet des spécificités qui leurs sont propres en raison du caractère à la fois montagneux et insulaire de la région impactée. L’approche utilisée repose sur la confrontation de simulations numériques conduites avec le modèle Més0-NH aux observations recueillies pendant la campagne HyMeX de l’automne 2012.

Contexte géographique

Le bassin méditerranéen est situé entre l’Afrique au sud, l’Asie à l’est et l’Europe au nord. Ses côtes sont densément peuplées et donc vulnérables. Son climat est très contrasté avec des zones désertiques au sud et des zones tempérées au nord. Les contrastes pluviométriques sont particulièrement marqués entre les rives sud du bassin très arides et les côtes est de l’Adriatique où sont enregistrées des précipitations annuelles supérieures à 3000 mm qui en font une des régions les plus pluvieuses d’Europe. Une autre caractéristique majeure du bassin méditerranéen réside dans la présence de nombreux reliefs côtiers qui induisent un système de vents locaux complexe. Les zones côtières exposées au flux marins sont fréquemment frappées par des fortes pluies qui sont principalement observées en automne dans l’ouest du bassin et davantage en hiver dans sa partie orientale (see, e.g., Froidurot et al., 2016; Jansa et al., 2000, 2001; Morel and Sénési, 2002a,b; Ricard et al., 2012; Rysman et al., 2016; Trigo et al., 2002). Dans la perspective d’une augmentation de la fréquence de ces évènements intenses (Blanchet et al., 2016;

Homar et al., 2010; Gao et al., 2006), de gros efforts sont pour mieux comprendre les mécanismes impliqués et la façon dont ils interagissent.

Située dans le bassin nord occidentale, la Corse (Fig. 1.2) est une île montagneuse qui culmine à 2706m au Monte Cinto et dont près de 120 sommets dépassent les 2000 m. La chaîne de montagne centrale, globalement orientée nord sud, constitue un obstacle au vent zonal. Durant la campagne HyMeX, différents sites instrumentés ont été déployés en Corse. La Corse possède en effet le double intérêt d'être une zone cible (susceptible d'être impactée par de fortes précipitations) et une zone amont (permettant d'observer les précurseurs des systèmes précipitants qui vont impacter les côtes du sud-est de la France et de l'ouest de l'Italie). Par ailleurs, du fait de son caractère insulaire, la Corse constitue un laboratoire naturel pour observer les interactions entre des flux marins peu perturbés et une orographie complexe.

Les mécanismes physiques

Les précipitations intenses sont associées au phénomène de convection profonde qui conduit à des systèmes nuageux à fort développement vertical. Ce phénomène nécessite trois ingrédients majeurs: une colonne atmosphérique conditionnellement instable, une fort apport d'humidité ainsi qu'un mécanisme de soulèvement. Ce dernier peut avoir des causes multiples telles que le soulèvement orogrographique ou la présence de zones de convergence d'origine thermique ou dynamique qui peuvent agir isolément mais aussi se combiner. Les nombreux travaux réalisés jusqu'alors illustrent parfaitement la complexité des interactions possibles entre convection et orographie ainsi que les nombreux défis qu'elles posent aux modèles de prévision du temps.

Objectifs du travail et plan de la thèse

L'objectif central est d'améliorer la connaissance des processus physiques impliqués dans les événements de fortes pluies en Corse et de mieux comprendre leur interaction avec la topographie complexe de l'île. Afin de mieux caractériser ces événements nous nous intéressons tout d'abord à leur climatologie. L'étude porte sur 31 ans d'observations pluviométriques et de réanalyses météorologiques. Les méthodes utilisées reposent sur une analyse en composantes principales et un algorithme de classification. Le travail se poursuit par l'étude détaillée des trois épisodes qui ont affecté la Corse durant l'automne 2012. Le premier (4 septembre 2012) est associé à une profonde dépression quasi-stationnaire. Il a généré de très fortes précipitations principalement le long de la côte est de l'île. Le second cas d'étude (31 octobre 2012) se caractérise par une dépression qui s'est rapidement déplacée depuis les îles Baléares vers le nord de la Corse. Enfin Le cas du 23 Octobre 2012 correspond à un épisode de convection profonde quasi-stationnaire qui s'est développée sur une ligne de convergence située en mer au sud-ouest de la Corse. Chaque cas est discuté dans le contexte de la climatologie puis simulé avec le modèle Mésoscale-NH. L'approche est systématique et consiste à réaliser des ensembles de simulations initialisées à partir de différents jeux de conditions initiales et de couplage aux frontières latérales. En outre, la sensibilité à la résolution horizontale du modèle est étudiée en comparant les résultats obtenus aux résolutions de 2.5 et 0.5 km. Différents tests de sensibilité pour lesquels la topographie du modèle a été modifiée complètent l'étude.

Chapter 1

General Introduction

Rain is an essential factor for human civilization. Cities have always been built where access to fresh water was available and over the course of history long term shifts in precipitation patterns have caused the dawn and downfall of entire empires. However, over shorter time spans precipitation can also vary greatly depending on the location. Droughts can eradicate harvests and cause famines and shortage of fresh water for humans, animals and plants alike. On the other end of the spectrum, heavy precipitation events (HPEs) are capable of devastating areas of up to thousands of square kilometers, endangering the lives of countless people and causing enormous economic damage. HPEs can cause landslides, flooding, erosion, and damage to buildings and infrastructure, e.g. roads, train lines, electricity grids, and freshwater supply. Thus a deep understanding of precipitation and the involved mechanisms is of the utmost importance for any populated area around the world.

As part of the HyMeX (Hydrological Cycle of the Mediterranean Experiment)¹ program, this work aims to provide a better understanding of the mechanisms of heavy precipitation on the Mediterranean island of Corsica. The primary tools

¹<http://www.hymex.org>

are numerical simulations of the events and the comparison to observations gathered during the respective events. This chapter represents a general introduction by presenting the geographical context of the studies, the HyMeX program and a short history of numerical weather prediction. The atmospheric scales are explained and their implications for the challenges in current weather models are presented shortly. In addition, the basic physical processes of convective instability and the mechanisms of heavy precipitation are presented, with a focus on orographic precipitation and the interaction of convection with underlying terrain. This is followed by a selection of literature on HPEs focusing on the Mediterranean basin and in particular on Corsica. Lastly, the goals and outline of this work are presented, concluding the general introduction.

1.1 Geographical Context - The Mediterranean Basin

For thousands of years, the Mediterranean sea (see Fig. 1.1) has been one of the centers of civilization and it has a densely populated coast with complex orography and a diverse climate. The Mediterranean sea is located between Europe in the north, Asia in the east, Africa in the south, and the Atlantic ocean in the west, to which it is connected through the strait of Gibraltar. It lies between the temperate regions of western and central Europe in the north and the Sahara desert in the south. In fact, the Mediterranean climate is extremely diverse, ranging from arid conditions in north Africa (see, e.g., Thornes et al., 1998) to one of the wettest regions of Europe along the mountain ranges east of the Adriatic (see, e.g. Mehta and Yang, 2008). During the summer, the weather is relatively dry with regular heat waves (more than once per year on average between 1950 and 1995, Thornes et al., 1998).

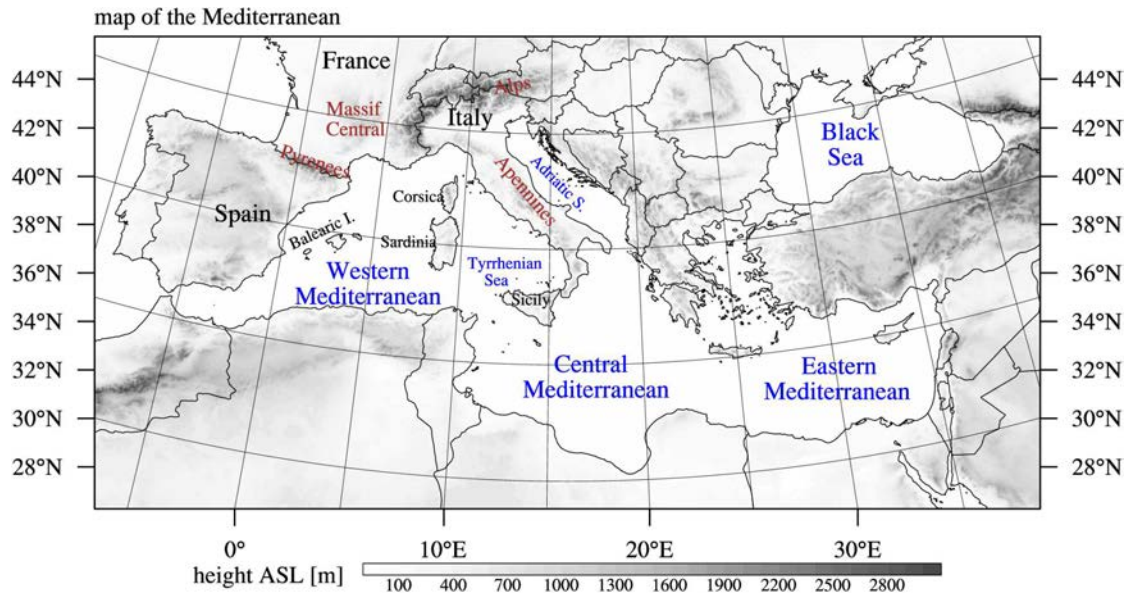


Figure 1.1: Map of the Mediterranean with geographical references and terrain height contours.

The Mediterranean is split into three main basins. The western Mediterranean is located between the Iberic peninsula, France, Italy and north Africa, the central Mediterranean is located south of Italy and southwest of Greece and the eastern Mediterranean is located between Greece, Turkey, Egypt and Libya. In the north-east the Mediterranean is connected to the Black sea via the Bosphorus, which separates Europe and Asia. A smaller side arm, the Adriatic, extends north between Italy and Croatia, Montenegro, Albania, and Greece.

In addition to the diverse climate, the orography around the Mediterranean, and also on some of its larger islands, is highly complex. Several mountain ranges border the sea, the most important ones around the north of the western Mediterranean basin being the Apennines in Italy, the Alps in central Europe, the Massif Central in southern France, and the Pyrenees at the border between Spain and France. These mountain ranges impact the air flow into the western Mediterranean

1.1. GEOGRAPHICAL CONTEXT

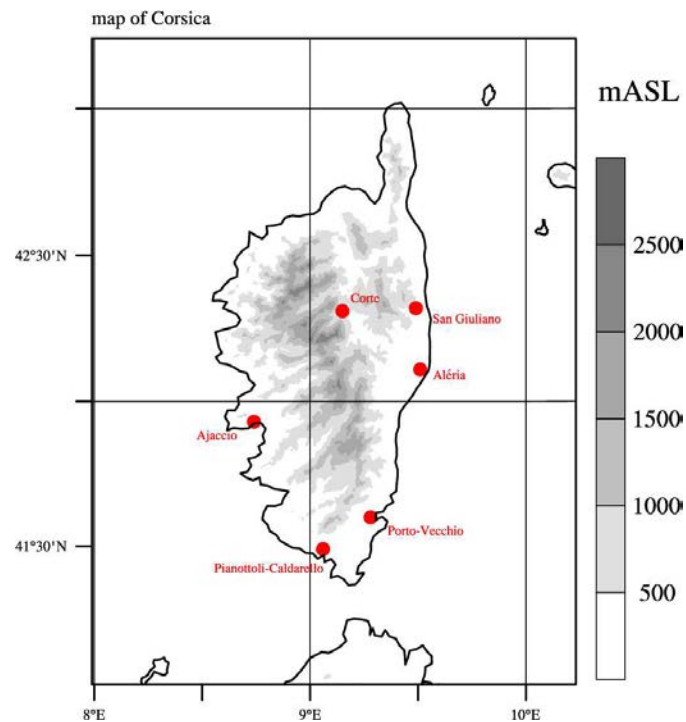


Figure 1.2: Map of Corsica with geographical references and terrain height contours.

basin and, depending on the wind direction, can directly impact the upstream conditions of HPEs.

Corsica (Fig. 1.2) is located in the north of the western Mediterranean, between Italy in the north and east, Sardinia in the South, and continental France in the northwest. Corsica has a north-south extent of about 180 km and an east-west extent of about 80 km. A mountain range covers the island in north-south direction. Its highest peak, Monte Cinto, is 2706 m high and around 120 other summits are higher than 2000 m.

The coasts and islands of the Mediterranean basin are often struck by devastating high precipitation events (HPEs), which occur predominantly in autumn (winter) over the western (eastern) Mediterranean (see, e.g., Froidurot et al., 2016; Jansa et al., 2000, 2001; Morel and Sénési, 2002a,b; Ricard et al., 2012; Rysman

et al., 2016; Trigo et al., 2002). In the prospect of a probable increase of such HPEs (Blanchet et al., 2016; Homar et al., 2010; Gao et al., 2006), a considerable amount of effort is made to better understand the involved mechanisms.

1.2 The HyMeX Program

The HyMeX program (Ducrocq et al., 2014) is an international program aimed at a better understanding of the hydrological cycle of the Mediterranean sea. It is part of the MISTRALS² (Mediterranean Integrated STudies at Regional And Local Scales) program. One central aspect of HyMeX is the exploration of the mechanisms behind HPEs. In addition, the impact of climate change on the Mediterranean is explored, since this region is one of the hot-spots of climate change, facing both, an increase in HPEs and droughts. In the framework of the program, a database³ was set up to host a large amount of operational and program-specific observations as well as the output of multiple numerical models.

Part of the HyMeX program is a large field campaign in the Mediterranean. The long observation period (LOP) takes place from 2010 until 2020, spanning about 10 years, and its goal is to gather long-term hydrological, oceanographic, and meteorological observation throughout the entire Mediterranean basin. An enhanced observation period (EOP) took place from mid 2011 to mid 2015, with an emphasis on research observations. During autumn 2012 and spring 2013, two special observation periods (SOPs) took place. Their focus lay in the northwestern Mediterranean, particularly the Spanish and French coasts, Italy, the Balearic Islands, Corsica, and Sardinia. SOP 1 (5 September to 6 November 2012) was dedicated to the observation and modeling of HPEs and SOP 2 (1 February to 15 March 2013) was dedicated to the observation of strong winds and their impact

²<http://www.mistrals-home.org>

³<http://mistrals.sedoo.fr/HyMeX/>

on the ocean mixed layer, dense water formation and ocean convection. The SOPs are divided into multiple intense observation periods (IOPs), which are associated with the individual events observed during each SOP. An IOP is thus limited to the region where the HPE occurred. In addition, IOPs can be split into multiple parts if the same system moved over multiple regions, e.g. IOPs 15a, b, and c, which took place over Catalonia, the Cévennes, and Corsica from 20 to 23 October 2012.

During SOP 1, instruments were deployed all along the northwestern coast of the Mediterranean. On Corsica, the Karlsruher Institut für Technologie (KIT) deployed a number of instruments. Their KIT-Cube, a collection of instruments dedicated to the exploration of the turbulence, moisture, and aerosols of the boundary layer, was located in Corte, in the north of Corsica (see Fig. 1.2). In addition, the KIT provided multiple atmospheric soundings a day during several IOPs. The balloons were launched in San Giuliano at the east coast, where an X-band research radar was also deployed by the KIT (Fig. 1.2), among other instruments. These instruments complement the operational network on Corsica, which consists of roughly 125 surface station, an operational weather radar in Aléria and the operational radiosoundings from Ajaccio (at 00 and 12 UTZ, see red markers in Fig. 1.2).

The atmospheric observatory CORSiCA⁴ (Corsican Observatory for Research and Studies on Climate and Atmosphere-ocean environment, Lambert et al., 2011) was set up on Corsica, serving both HyMeX and the Chemistry-Aerosol Mediterranean Experiment (ChArMeX). Lastly, the SAETTA (Suivi de l'Activité Electrique Tridimensionnelle Totale de l'Atmosphère) has been deployed on Corsica since 2014 in the framework of CORSiCA . All these programs are aimed toward

⁴<http://www.obs-mip.fr/corsica>

a better understanding of the Atmosphere and the Ocean in the Mediterranean, continuing an effort that has been going on for centuries.

1.3 Numerical Weather Prediction

This thesis relies heavily on the usage of numerical simulations of high precipitation events. With regard to this focus, a short history of numerical weather prediction as well as current challenges are presented in this section. While the increasing availability of computational resources greatly increased the potential for the usage of numerical models, it also comes with new challenges, which are explained below.

1.3.1 The Beginning of Numerical Weather Prediction

Even though the first attempts at weather prediction were made more than 2000 years ago, the bulk of the knowledge about precipitation and its prediction has been acquired during the last century. Specifically, the succession of low and high pressure which accompanies the changing weather in the mid latitudes was only understood as recently as around 100 years ago. The atmosphere is a large dynamic system and its accurate description requires the knowledge of its state, which is only obtained by observations at multiple locations over a large area. These have to be sufficiently dense in space and time (see, e.g., Bjerknes, 1919). Because of this, meteorology was one of the first disciplines which made wide use of the early means of telecommunication.

Vilhelm Bjerknes (1916) was the first to explain cyclones as resulting from disturbances in the westerly winds, which are often found in the mid-latitudes. His work was then validated by his son, who developed an empirical model of a mid-latitude cyclone based on surface observations (Bjerknes, 1919) and described rain as result of lifting processes along fronts and orographic barriers (Bjerknes

and Solberg, 1921). They also explained mid latitude cyclones as resulting from disturbances in the polar front and provided the first schematic model of the mid-latitude circulation (Bjerknes and Solberg, 1922).

The idea and attempt of numerical weather prediction predate the advent of the first computers by more than two decades. Undergoing the process of discretizing the thermal and dynamical fields of the atmosphere and their governing equations in space and time requires a large number of calculations, making it impossible to do even in real time without the help of computers. The first attempt, however, was done by Richardson (1922). He attempted a 6-hour forecast of the surface pressure using a set of discretized equations. It took Richardson 6 weeks to calculate just two vertical columns and he estimated that for a horizontal grid size of 200 km *"64000 computers [referring to persons doing the calculations manually, author's note] would be needed to race the weather for the whole globe"* (Richardson, 1922, p. 219). Unfortunately, his forecast for the change in surface pressure was wrong by two orders of magnitude due to an imbalance of wind and pressure in his initial conditions. Removing these imbalances would take another 20 years.

The upper level structure of the mid-latitude atmosphere was described by Rossby et al. (1939), who developed the theory of what we nowadays know as barotropic Rossby-waves. This theory was refined by accounting for the earth's curvature (Haurwitz, 1940) and extended to a baroclinic atmosphere (Bjerknes and Holmboe, 1944). Based on their work, Charney (1947) presented a way to remove acoustic waves and shearing-gravitational oscillations from the perturbation equations, eliminating the problems that prevented the success of Richardson in 1922. These equations formed the basis of later work (Charney, 1949; Charney and Eliassen, 1949), which led to the first successful computer-based numerical weather forecast (Charney et al., 1950), obtained by numerical integration of the barotropic vorticity equation. Over the following decades, computational power

has grown exponentially, allowing smaller grid spacings and time steps, the use of more complete sets of equations and more sophisticated parametrizations for subgrid processes such as microphysics and turbulence. However, this progress has its challenges.

1.3.2 Atmospheric Scales - Synoptic, Meso- and Micro-scale

Weather models are based on the equations that govern the evolution of a given state (pressure, temperature, moisture, wind) of the atmosphere over time. Values of the fields are discretized onto a number of points which are distributed on a grid that covers either the entire globe or a limited region. Typically, the values at a certain grid point are then viewed as representative for the entire grid cell. A basic property of the computational grid is the distance between its points which equates to the grid cell size.

For global models, the grid spacing is often in the tens of kilometers while for localized weather models in research applications the horizontal grid spacing can reach less than 100 m. Atmospheric phenomena also have typical scales. Rossby waves span over thousands of kilometers and the surface low and high pressure systems can become equally large. On the other end of the scale, turbulent eddies are found everywhere in the atmosphere with sizes down to the fraction of a millimeter. Between the synoptic (large) and the microscale a range of phenomena can be found in the mesoscale (Orlanski, 1975), like frontal circulations, convective systems, orographically induced circulations or sea and land breeze systems. Depending on the phenomenon, a grid spacing of few kilometers down to around 100 m is necessary to capture the relevant processes. As a result, certain mesoscale phenomena are sometimes represented by a limited number of grid points or they might fall entirely within just one grid cell.

In order to fully capture all relevant motions of turbulent flow in a simulation, one would have to resolve all scales of motion. The minimum size of turbulent eddies which have to be resolved does have a lower limit (Kolmogorov, 1941), but unfortunately it is beyond any reasonable grid spacing currently achievable in weather models. The scale of these eddies, the Kolmogorov-microscale, depends on the kinematic viscosity ν and is given by

$$\eta = \left(\frac{\nu^3}{\epsilon} \right)^{\frac{1}{4}}, \quad (1.1)$$

where $\epsilon = u^3/l$, and u and l are the velocity and length scale of the energy containing eddies (Bryan et al., 2003; Kolmogorov, 1941). The turbulent eddies which would need to be resolved in deep moist convection are of the size of approximately $3 \cdot 10^{-4}$ m, requiring grid spacings of around 0.1 mm (Bryan et al., 2003), which would allow the direct numerical simulation (DNS) of turbulent flow. A 50 by 50 by 20 km domain for the simulation of an isolated convective cell would have $5 \cdot 10^{16}$ - in words: ten quadrillion - grid points.

To circumvent these extreme resolution requirements, turbulent processes are parametrized. There are two main approaches, the first one being large eddy simulations (LES), which depend on the explicit representation of an inertial subrange (energy containing scale). This is generally not accomplished with grid spacings much larger than 100 m. The second approach is to parametrize processes which are not represented at grid spacings of several kilometers and more. Such parametrizations primarily handle planetary boundary layer processes like vertical mixing, turbulence and heat flux. Between 100 m and several kilometers is a gap, for which no appropriate turbulence parametrizations exist (Bryan et al., 2003; Wyngaard, 2004). Within this range, processes included in the parametrization schemes begin to be explicitly represented in the simulations. Nevertheless, mod-

els are regularly used at grid spacings within this gray zone (Wyngaard, 2004) and despite the shortcomings in model design they produce valuable results.

1.4 The Physics of Heavy Precipitation Events

Deep moist convection (DMC) is involved in a large number of Mediterranean HPEs (see, e.g. Davolio et al., 2009; Doswell et al., 1998; Ferretti et al., 2000; Jansa et al., 2000, 2001; Lambert and Argence, 2008; S en esi et al., 1996; Tapiador et al., 2012; Trapero et al., 2013). For deep moist convection to occur, three ingredients are required: conditional instability, low level moisture, and lift (Doswell et al., 1996; Doswell, 1987).

1.4.1 Convective Instability

In this work, instability refers to the stability of the atmosphere with respect to the vertical displacement of an air parcel. This section gives a short overview of convective instability in the atmosphere (for a comprehensive explanation, see, e.g. Holton, 2004, p. 289–298). Due to the vertical pressure gradient in the atmosphere a dry vertically displaced air parcel cools down as it ascends. The cooling rate is given by the dry adiabatic lapse rate

$$-\frac{dT}{dz} = \frac{g}{c_p} = \Gamma_d, \quad (1.2)$$

where $g = 9.81 \text{ m s}^{-2}$ is the the gravitational acceleration and $c_p = 1005 \text{ J kg}^{-1}$ is the heat capacity of air at constant pressure. In the lower atmosphere Γ_d is approximately constant at 9.76 K km^{-1} . If the vertical temperature lapse rate $-dT/dz$ is larger than Γ_d , i.e. the atmosphere is statically unstable, any upward (downward) displaced parcel will become positively (negatively) buoyant and con-

tinue to ascend (descend). However, if the atmosphere is statically stable any upward (downward) displacement will cause the parcel to become negatively (positively) buoyant and buoyancy will act as a restoring force, pushing the parcel back to its original level. This restoring force can lead to buoyancy oscillations in the atmosphere. The frequency of these oscillations is given by

$$N^2 = g \frac{d \ln \theta}{dz} = \frac{g}{\theta} \frac{d\theta}{dz}, \quad (1.3)$$

where N^2 is called the Brunt Väisälä frequency, θ is the potential temperature, and z is the altitude. In summary, static stability in a dry atmosphere depends on the vertical temperature gradient

$$-\frac{dT}{dz} \begin{cases} > \Gamma_d, N^2 < 0 & \text{statically unstable} \\ = \Gamma_d, N^2 = 0 & \text{statically neutral} \\ < \Gamma_d, N^2 > 0 & \text{statically stable} \end{cases} \quad (1.4)$$

With the addition of moisture, latent heat has to be considered. If a moist parcel is lifted, it will cool until its temperature is equal to its dew point, at which point the water vapor will begin to condense. The level at which this happens is called lifting condensation level (LCL). The condensation of water vapor converts latent energy into sensible heat, thereby slowing down the cooling of the parcel as it ascends. The lapse rate at which the parcel cools is called the pseudoadiabatic lapse rate

$$\Gamma_s = -\frac{dT}{dz} = \Gamma_d \frac{1 + L_c/(RT)}{1 + \epsilon L_c^2 q_s / (c_p RT^2)} \quad (1.5)$$

where $\epsilon=0.622$, q_s is the saturation mixing ratio, R is the gas constant for dry air, and $L_c \approx 2.5 \cdot 10^5 \text{ J kg}^{-1}$ is the latent heat of condensation. In the lower atmosphere, Γ_s is approximately 6 to 7 K km⁻¹. For a lapse rate $\Gamma_s < \Gamma < \Gamma_d$

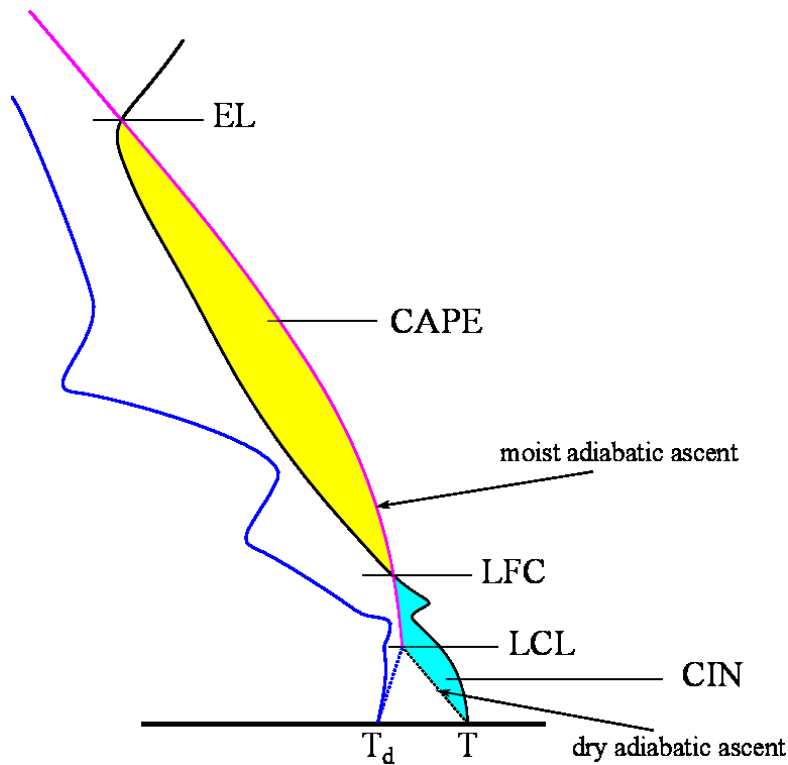


Figure 1.3: Simple example of the vertical profile of a conditionally unstable atmosphere. Temperature T (dew point T_d) of the environment are shown by the black (blue) lines. The black and blue dashed lines show T and T_d for the dry adiabatic ascent of a parcel from the surface, the pink line shows the moist adiabatic ascent above the LFC.

the atmosphere is stable to vertical displacement of unsaturated air parcels but unstable to the vertical displacement of saturated parcels. Saturation is a necessary condition for this instability, which is therefore called conditional instability. We call θ_e^* the equivalent potential temperature of a hypothetically saturated parcel. The use of θ_e^* is to underline the necessary condition (saturation), because while θ_e is well defined for unsaturated parcels, the statements on stability do not apply without saturation being present. For Γ_s it follows that $d\theta_e^*/dz = 0$.

$$\frac{d\theta_e^*}{dz} \begin{cases} < 0 & \text{conditionally unstable} \\ = 0 & \text{saturated neutral} \\ > 0 & \text{conditionally stable} \end{cases} \quad (1.6)$$

From its origin, a lifted parcel undergoes dry adiabatic ascent (dashed black in Fig. 1.3) as long as it is unsaturated. As it reaches its LCL, the freed latent energy slows down the cooling and it continues its moist adiabatic ascent (conserving θ_e , pink in Fig. 1.3). During the first part of its ascent, the parcel is cooler than its environment and negatively buoyant. The energy necessary to overcome this phase is called convective inhibition (CIN), and it has to be provided by external forces. Above the level of free convection (LFC), the temperature of the parcel is higher than that of the environment, allowing it to rise on its own. The parcel continues to accelerate until it reaches the equilibrium level (EL), sometimes also referred to as level of neutral buoyancy (LNB). Convective clouds often show an overshooting top where rising air moves past its EL before slowing down and descending again. Integrating buoyancy force along the parcel's path between the LFC and the EL yields the convective available potential energy (CAPE). CAPE and CIN are given by

$$CAPE = \int_{z_{LFC}}^{z_{EL}} g \frac{T_{parcel} - T_{env}}{T_{parcel}} \quad \text{and} \quad CIN = \int_{z_0}^{z_{LFC}} g \frac{T_{parcel} - T_{env}}{T_{parcel}} \quad (1.7)$$

By this definition, CAPE is positive and CIN is negative. However, both are usually given in absolute values. In the simplified skew-T diagram (Fig. 1.3), CIN (CAPE) is represented by the cyan (yellow) area. For deep moist convection to occur, initial lift is necessary to overcome convective inhibition and reach the LFC. This initial lift can come from orographic lifting or lifting above a convergence zone. Diurnal heating can also heat the boundary layer and gradually erode CIN

until deep convection is initiated. Often a combination of such processes will act. Assuming a perfect energy conversion, the upper limit imposed on the vertical velocity by CAPE is

$$w_{max} = \sqrt{2CAPE}. \quad (1.8)$$

In practice, entrainment (mixing of cool dry air into the convective plume) and friction will prevent any rising parcel from reaching w_{max} . The initiation of deep moist convection is difficult to predict because the initial lifting can happen due to small scale processes which are not resolved in numerical models.

1.4.2 Orography and its Effect on Air Flow and Precipitation

Since the Mediterranean is surrounded by multiple high mountain ranges and some islands have mountains in excess of 2000 m, orographic effects play an essential role in Mediterranean HPEs. The interaction between orography and air flow has been repeatedly studied for decades, but even idealized mountain shapes and constantly stratified layers of dry air introduce a number of different phenomena. In the simple 2D case (an infinitely long ridge) and homogeneous cross-mountain flow the effect is limited to relatively simple topographic waves. Variation of the cross-mountain wind or the stability with height allows the formation of lee waves which can extend hundreds of kilometers downstream of mountains (Durrán, 1990). When air flow encounters a mountain, one primary question is whether the flow will traverse the obstacle or be blocked by it. The parameter that helps to determine the answer is the Froude number

$$Fr^2 = \frac{\bar{u}^2}{c^2} = \frac{\bar{u}^2}{gL_c}, \quad (1.9)$$

where \bar{u} is the mean environmental wind speed, c^2 is the shallow water wave speed (see, e.g. Holton, 2004, p. 287), and L_c is the characteristic length. The Froude

number Fr can be understood as the ratio of kinetic and potential energy. For $Fr < 1$ (subcritical) flow will tend to be blocked by an obstacle while for $Fr > 1$ (supercritical) the flow will pass over the obstacle. For $Fr \approx 1$ the linear solution breaks down. The flow is subcritical upstream of the obstacle, turns supercritical above the obstacle and tends to form a downslope windstorm in the lee with a hydraulic-jump-like feature, where the flow adjusts back from super- to subcritical in a turbulent zone (Durrán, 1990). In real case scenarios, the applicability of these concepts is somewhat limited, as the atmosphere is neither homogeneously stratified nor is the flow horizontally or vertically homogeneous. Reinecke and Durrán (2008) presented a way to estimate the resulting flow regime for real cases. They use the mountain height normalized by a scale for the vertical wavelength of a linear 2D hydrostatic mountain wave, sometimes also called inverse Froude number (see also Smith, 1989a)

$$\hat{h} = \frac{Nh}{u}, \quad (1.10)$$

where N is the Brunt Väisälä frequency, h is the mountain height and u is the cross mountain wind speed. One method to determine \hat{h} proposed by Reinecke and Durrán (2008) is to measure u and N below the mountain height and then take the average over the layer below h to calculate \hat{h} .

Even in dry homogeneous flow, simple setups can produce complex solutions, such as stagnation points (Smith, 1989b), lee vortices, wakes (Schär and Smith, 1993a) and vortex streets (Schär and Smith, 1993b). The above mentioned phenomena are also observed in the atmosphere, such as the wake of Madeira (Grubišić et al., 2015), and they can also be relevant for regional weather phenomena, like the cyclogenesis supported by Alpine blocking (Egger, 1988; Pichler et al., 1990), which also occurs over the Gulf of Genoa (Trigo et al., 2002).

Taking moisture into account introduces a number of additional mechanisms, which happen primarily due to the conversion between latent and sensible heat. If

the lifting is sufficient to produce clouds, latent heat is converted into sensible heat, changing the stability profile. If rain forms, it will fall out of the cloud into the unsaturated layer below and start evaporating, thereby cooling the air beneath the cloud and forming a cold pool. Even over an idealized 2D mountain a simple setup such as a moist nearly neutral flow with constant u can lead to complex effects, such as downslope windstorms, convective cells and upstream mid-level drying (Miglietta and Rotunno, 2005). In conditionally unstable flow, rain was found upstream and downstream of the 2D mountain for weak and intermediate u (2.5 and 10 m s⁻¹) and over the mountain for strong u (20 m s⁻¹). Convection initiated along the windward slope produced a cold pool which propagated upstream when u was weak (Miglietta and Rotunno, 2009). The highest rainfall amount was seen for simulations where u balanced the upstream propagation of the cold pool, resulting in quasi-stationary convection which allowed large accumulations of rain (Miglietta and Rotunno, 2009, 2010). It was also found that a sheared profile with cross mountain wind in the boundary layer and weaker or no cross mountain wind aloft allows the formation of deeper and more intense convective cells (Miglietta and Rotunno, 2014). Real cases are vastly more complex because the terrain, airflow and moisture are inhomogeneous 3D fields which change over time.

A comprehensive review of orographic effects on rain is available in Houze (2012). Figure 1.4 shows schematic illustrations of orographic mechanisms. Moist air which encounters orography and follows its slope upward forms an orographic cloud when stable (Fig. 1.4a) or convective cells when unstable (Fig. 1.4b). In addition, the terrain itself may induce diurnal wind systems which in turn can lead to the formation of clouds. During the day, heating causes warm upslope flows (Fig. 1.4c) and during the night, radiative cooling along the surface induces downslope flows, which can lead to convergence along the base of the mountain (Fig. 1.4d). A mountain may also locally directly enhance precipitation by orographic lifting (Fig.

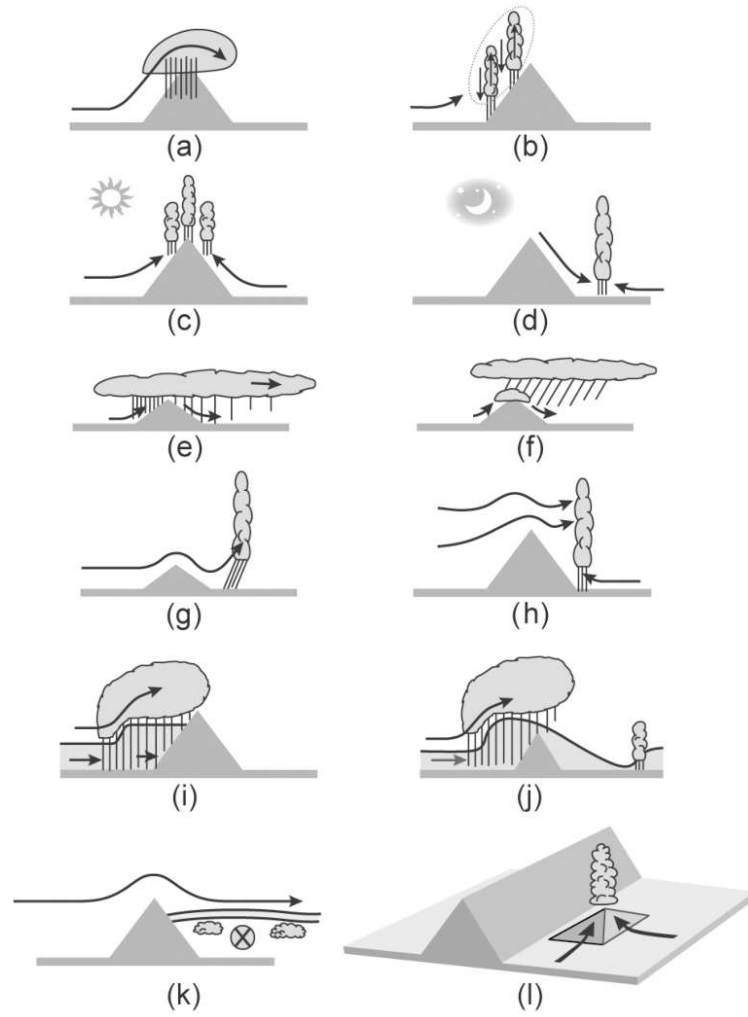


Figure 1.4: Examples for orographic precipitation (Houze, 2012)

1.4e) or increase precipitation originating from a higher non-orographic cloud, the "seeder" (Fig. 1.4f), where the lower cloud is referred to as "feeder". Topographic waves may trigger convective cells downstream of the mountain (Fig. 1.4g) or locally enhance preexisting convection (Fig. 1.4h). A cold pool forming beneath a precipitating cloud can be fully (Fig. 1.4i) or partially (Fig. 1.4j) blocked and act as an obstacle which provides lift. Figure 1.4k shows a mechanism by which dry flow over a mountain can result in a capping inversion, which allows conditional instability to build up. Figure 1.4l shows one possible way to release this built up instability by overcoming convective inhibition via warm upslope flow over a hill.

Considering the wide range of mechanisms which can work together to influence the formation of clouds, convective cells and precipitation, it is not surprising that the detailed explanation of such events can be difficult. The precise forecasting of orographic precipitation also poses a challenge, especially if it occurs in connection with DMC (see, e.g. Hanley et al., 2011).

1.4.3 Heavy Precipitation Events in the Mediterranean

Ricard et al. (2012) showed that long-lasting HPEs over southern continental France and Corsica are mostly associated with quasi-stationary trough-ridge patterns, high CAPE values over the western Mediterranean and a moist troposphere. Low level jets (LLJ) advect moisture from the sea toward the coast, where the HPEs occur. These unstable inflows together with lifting above orography or along convergence lines lead to DMC, which can either occur alone or embedded into larger, stratiform precipitation systems.

Duffourg and Ducrocq (2011) analyzed recent events over southern France in an attempt to explore the origin of the moisture supply. They found that the main sources of moisture for the studied HPEs were evaporation over the Mediterranean and advection from the Atlantic. Ducrocq et al. (2008) looked at three

HPES over southern France and analyzed the mesoscale ingredients for stationary events. They identified orographic lift and lifting along the edge of cold pools as primary lifting mechanisms. In all cases, a conditionally unstable LLJ was impinging on an obstacle, supplying the convective system with moisture and an inflow of potentially unstable air.

Numerical models can help tremendously in understanding single events as well as the involved processes. Before the wide availability of mesoscale models, Ducrocq et al. (2002) found that models with a grid spacing of 2.5 km are well capable of outperforming low resolution (10 km) models. However, this improvement required that the initial conditions were well captured. They even found that poorly captured initial conditions could reverse the results, causing the high resolution simulations to perform worse than the low resolution simulations. Since then, the availability of computational resources has increased drastically and grid spacings of 2.5 km and less have become feasible even for operational purposes. Nevertheless, small changes in initial conditions can cause large differences on the mesoscale, especially when convection is involved. Thus, large efforts have been made to explore and improve the capability of such high resolution models. Hally et al. (2014a,b) explored the potential of a stochastic ensemble by adding random perturbations to model physics. They analyzed their results in terms of dispersion of the precipitation forecast and found that this approach has the potential to assess the sensitivity of HPES. However, they also found the initial conditions to be the most important criterion. Fresnay et al. (2012) used the same method, including tests with a grid spacing of 500 m. They found that at this higher resolution the ensemble shows a larger sensitivity to perturbations in model physics. Instead of perturbing only one microphysical scheme, Tapiador et al. (2012) created an ensemble by using different schemes not only for microphysics but also for cumulus parametrization and the land surface. In addition, they tested perturbed

initial conditions. Their results show that using multiple schemes resulted in a larger spread than the perturbed initial conditions.

Numerous case studies using numerical models have been conducted to learn more about the details of HPEs in the Mediterranean region. Doswell et al. (1998) showed that heavy precipitation in the Mediterranean region can be associated with different processes, such as DMC but also orographic enhancement of precipitation below a relatively stable air mass. Sénési et al. (1996) studied the Vaison-La-Romaine flash-flood event in southern France. They found that a cut-off low and its slowly moving cold front led to a squall line. The slow movement of the system led to large precipitation accumulations. Trapero et al. (2013) studied a catastrophic 1982 flash-flood event in the Pyrenees, which affected Spain, Andorra, and France. They found a quasi-stationary extratropical cyclone advecting moist air toward the Pyrenees. Buzzi et al. (1998) studied a HPE over the Piedmont in northwestern Italy in 1994. They determined the local orography as an important factor, which influences precipitation by forcing orographic lifting. Buzzi et al. (1998) also conducted sensitivity tests by deleting parts of the orography and changing model physics. They found that removing the terrain caused the HPE to shift downstream while changes in evaporative cooling and latent heating controlled the formation of cold pools and the capability of the air to move over orography, respectively. Ferretti et al. (2000) confirmed the importance of orography and orographic lifting for that particular event. It was later found that the 1994 Piedmont flash flood was intensified by dryer air from the east which was blocked by the Alps and deflected westward, increasing convergence beneath the convective cells (Rotunno and Ferretti, 2001). Davolio et al. (2009) studied a HPE which occurred at the Adriatic coast. It was caused by convergence of a northeasterly barrier jet along the Alps and a southeasterly moist LLJ from the Adriatic sea. In a comprehensive analysis of multiple events, Davolio et al. (2016) found

that the precipitation distribution over northeastern Italy depended heavily on the thermodynamic profile of the incoming flow. Flow over the Alps tends to produce heavy precipitation over the orography whereas blocked flow leads to the formation of a barrier jet and upstream convergence, displacing the precipitation and convection over the flat terrain of the Po valley. Further east, similar events can occur. Kotroni et al. (1999) studied a HPE which occurred in 1997 over Greece. They also found DMC as a result of orographic lifting ahead of the cold front to be responsible.

All these events were associated with a cyclone and all of them were characterized by DMC. The interaction between orography and moist LLJs also plays a crucial role in the above mentioned cases. These ingredients common for HPEs along the coast of the Mediterranean and over its islands, however, they are not exclusive to the Mediterranean. Lin et al. (2001) found that very moist low level jets, conditionally unstable flow impinging on orography, steep mountains, and quasi-stationary synoptic systems are ingredients common to HPEs worldwide. One example in a different region would be the Madison County flash flood of 1995, which was analyzed by Pontrelli et al. (1999) and which was also caused by the simultaneous occurrence of a moist LLJ, orographic forcing, and synoptic forcing due to a short wave trough. The processes mentioned above show how complex such events can be. In many cases the involved mechanisms stretch over multiple orders of magnitude starting from synoptic systems with hundreds up to thousands of kilometers in size via regional topography and air mass variations to the paths of individual embedded convective cells and updrafts measuring only hundreds of meters to a few kilometers. The task of unraveling the interactions between scales and processes is challenging.

1.4.4 Heavy Precipitation Events over Corsica

From a composite analysis of 8 HPEs over Corsica, Ricard et al. (2012) showed that moisture and CAPE were generally high between Sardinia and continental Italy. According to their findings, the main source of moisture lies to the south of the island with southerly flow in the boundary layer being the dominant direction during HPEs over Corsica. The island and its interaction with precipitating systems were the subject of several studies during the recent years. Lambert and Argence (2008) did a preliminary study of the HPE of 14 September 2006. They demonstrated one of the difficulties with current mesoscale case studies, namely that the verification of the simulation output is difficult. While obtaining clearly different results with two different input data sets, no conclusion was reached as to which simulation was better than the other. They also encountered problems when trying to reproduce the fine scale features of the event even though the large scale was well captured in both their experiments.

A more in-depth analysis was performed by Barthlott and Kirshbaum (2013), who analyzed isolated convection which occurred on 26 August 2009. The event was characterized by DMC over Corsica and Sardinia. They simulated the case using different stretching factors for the terrain height between 0 and 1.3 and also without islands. Their modeling experiments indicate that the mountains influenced the formation of convection via their diurnal circulation. However, even the temperature gradients between a flat island and the sea would have been sufficient for initiation of DMC due to convergence along the sea-breeze front. Only the complete removal of the islands from the simulation completely suppressed deep convection. This shows that different factors contribute to the formation of convection, including but not limited to sea-breeze, land-breeze and orographic circulations.

The role of Sardinia in DMC over Corsica was investigated by Ehmele et al. (2015), who looked at six events and conducted tests with standard orography as well as flat and deleted Sardinia. They found a decrease in precipitation for cases with strong synoptic forcing and no systematic change for cases with weak synoptic forcing. The role of Sardinia consists of blocking or deviating the large scale flow and modification of convection over Corsica via cold pools generated by convection over Sardinia.

An idealized study was conducted by Metzger et al. (2014), who placed Corsica as an isolated island in homogeneous flow. They used vertical profiles to initialize their simulations and varied the wind direction in 15° steps. The tests were conducted using constant winds of 2 and 5 m s⁻¹. They also tested the effect of increased instability and a reduced saturation deficit between 900 and 400 hPa. For the cases where DMC was simulated, it occurred on the lee side of the island, initiated by convergence. Metzger et al. (2014) found that lower wind speeds are more reliable in initiating DMC. For the higher (5 m s⁻¹) wind speed they found that northerly and southerly winds are capable of producing convection while easterly and westerly winds were not. Their conditions were highly idealized. Nevertheless, their findings show that convection can form in the lee of Corsican orography.

For the study of HPEs, the island of Corsica, forms a natural observatory in the northwestern Mediterranean Sea. It lies off the coast of northwestern Italy and on many occasions the upstream conditions for precipitation events in Liguria and Tuscany and even southern continental France can be measured on Corsica. On the island, a mountain range stretches from the north to the south with altitudes of over 2700 m above sea level (ASL). This makes Corsica the ideal place to study the influence of mountains on previously relatively undisturbed inflow into precipitating systems and their interaction with orography.

1.5 Goals and Outline of this Thesis

This work aims to contribute a better understanding of the processes which lead to the formation of HPEs over Corsica. To provide context, a climatology of HPEs is presented in Chapter 2, which is obtained by applying well established methods within the geographical context of Corsica and the Mediterranean, in order to produce a highly specialized climatology and classification of events. In addition, we present three heavy precipitation events which occurred during SOP1 of the HyMeX program in autumn of 2012. Each of these events represents a different class of event. The case of 4 September 2012 (Chapter 4) was caused by a quasi-stationary cyclone east of Corsica. The case of 31 October 2012 (Chapter 5) was caused by a fast moving cyclone which approached the island from the west. The case of 23 October (Chapter 6) was caused by localized quasi-stationary DMC which formed along a convergence line over the southeast of Corsica. Each case is discussed within the context of the climatology and their analysis yields examples for mechanisms which contribute to HPEs over Corsica. To account for the uncertainties in model design at the mesoscale, each case is tested for its sensitivity to model resolution by comparing simulations at 2.5 km and 500 m horizontal grid spacing. Lastly, Chapter 7 contains a summary of the results and an outlook on future research based on the findings in this thesis.

Chapter 2

Climatology of Rainfall on Corsica

This chapter presents a 31 year (1985–2015) climatology of HPEs (>100 mm within 24 h) over Corsica. It seeks to answer the questions of how common such events are on Corsica and to analyze their seasonal cycle. In addition, a principal component analysis (Hannachi et al., 2007; Wilks, 2011) is performed on the ECMWF analysis data over the western Mediterranean to classify the HPEs. Three classes of events are identified and described. The methods used in this section are well established in atmospheric science. Here, they are applied to the western Mediterranean in an attempt to classify HPE over Corsica according to their geopotential and equivalent potential temperature θ_e fields and spatial distribution of precipitation. Section 2.1 contains a brief description of the climate in the Mediterranean and on Corsica, with focus on precipitation. The method used in this chapter is briefly explained in Section 2.2. Section 2.3 presents the seasonal distribution and mean fields, the EOFs and clusters are presented in sections 2.4 and 2.5, respectively. The physical interpretation of the clusters follows in section 2.6. The results are discussed in Section 2.7 and the conclusions are presented in Section 2.8.

2.1 Current Knowledge on the Climate of the Mediterranean

Precipitation in the Mediterranean follows a seasonal cycle. The summers are generally dry and during the late summer precipitation increases in the west, where cyclogenesis is most often found over the Iberian peninsula (Trigo et al., 2002). During September, October and December, the heaviest precipitation moves gradually east (see, e.g. Kelley et al., 2012; Mehta and Yang, 2008; Trigo et al., 2002). For Corsica, the maximum is found from September to December. The region around Corsica also has an exceptionally high cyclone track density (Alpert et al., 1990; Nissen et al., 2010) with the Gulf of Genoa just north of the island being the most active cyclogenesis region from November to February (Trigo et al., 2002).

Mehta and Yang (2008) obtained a precipitation climatology for the Mediterranean basin based on 10 years (1998 - 2007) of TRMM measurements. They found that the highest precipitation is found over the mountainous regions of Europe, namely the Pyrenees, the Alps, the Apennines and the mountain ranges east of the Adriatic, in Slovenia, Croatia, Bosnia and Herzegovina, Montenegro and Albania. In these mountains, the average precipitation is between 2 and 4 mm d⁻¹. On the other end of the scale, north Africa receives only around 0.1 mm d⁻¹. However, the precipitation over the Mediterranean basin shows a seasonal cycle in intensity and location. Mehta and Yang (2008) found that the strongest precipitation occurs from September to March, with the peak months being October to January. While the peak month for the western Mediterranean (5-10°E) is in November, the peak occurs later further east (November and December at 10°E and December to January at 30°E). In meridional direction, precipitation is located further north in the Summer (values of >2 mm d⁻¹ north of 45°N), the strongest precipitation moves south until it peaks around 37°N in November and December.

Even though this cycle is well known, there are still considerable difficulties in its accurate representation. Kelley et al. (2012) simulated the weather over the Mediterranean from 1950 to 2000 using the Coupled Model Intercomparison Project phase 5 (CMIP5) and evaluated its results using observations. In their simulation, they found the typical seasonal cycle of higher precipitation in winter and lower precipitation in summer. However, their model showed a drying throughout the seasons with the strongest trend seen in March, April and May. The observations, on the other hand, show drying predominantly during winter. Gao et al. (2006) attempted to estimate the change in precipitation toward the end of this century by simulating the 1961-1990 and 2071-2100 periods using the IPCC A2 (highest) emission scenario. They found an increase of precipitation over the northern Mediterranean, primarily from December to January, mostly over the French coast, around Genoa and the northern Adriatic. They also found a moderate increase for the September to November period mostly over the western Mediterranean. Their results also indicate an increase in extreme precipitation events over the northern Mediterranean.

A composite analysis for HPEs in the Mediterranean was done by Ricard et al. (2012). They examined the monthly distribution of HPEs ($>150 \text{ mm day}^{-1}$) from 1967 to 2006 and found that the majority of events (70%) occur from August to December with 20% in October alone. In addition, Ricard et al. (2012) examined the mesoscale environment of HPEs in four regions around the western Mediterranean (Languedoc-Roussillon, Cévennes-Vivarais, South Alps, and Corsica) based on a five year (2002-2006) climatology. For this period, they found a similar monthly distribution of events. They focused on the autumn period (August to December), and their analysis includes 40 HPEs observed from 2002 to 2006, 8 of which were located over Corsica.

Their composite analysis identified a trough over the British islands and Spain with southwesterly flow aloft as an important ingredient to HPEs in the western Mediterranean. They found a moist LLJ over the western Mediterranean impinging on the orography along the northern coast and conditionally unstable air upstream of the HPEs. For Corsica, their composite analysis revealed that the highest moisture and instability is usually found southeast of the island, over the Tyrrhenian sea between Corsica, Sardinia, Italy and Sicily. A trough is located over eastern Spain and a surface low is found centered north of the Balearic islands. The moist LLJ is found primarily east of Sardinia and Corsica, advecting warm and moist air from the Tyrrhenian sea toward the Corsican orography.

Cyclones are the primary cause of HPEs and their distribution over the Mediterranean has been repeatedly explored (see, e.g. Alpert et al., 1990; Campins et al., 2011; Maheras et al., 2001; Nissen et al., 2010; Trigo et al., 2002). Cyclone tracking algorithms tend to also identify relatively weak thermal lows, increasing the number of detected cyclones substantially. Most of these thermal lows are weak, short lived, and stationary. Their occurrence shows a well detectable diurnal cycle (Campins et al., 2011). This is especially true for the summer, when such lows form predominantly over the Sahara and the Iberian peninsula (Alpert et al., 1990; Campins et al., 2011; Trigo et al., 2002). In winter, cyclogenesis happens predominantly due to synoptic disturbances interacting with the baroclinicity found along the northern coast between the cold land and the relatively warm sea (Trigo et al., 2002). The Gulf of Genoa is the most active cyclogenesis region in the western Mediterranean, especially during winter (Alpert et al., 1990; Nissen et al., 2010; Trigo et al., 2002). The cyclones forming in the Gulf of Genoa show little to no diurnal cycle, deepen faster and are more intense than those of other cyclogenesis regions (Maheras et al., 2001), and are often associated with lee cyclones

caused by Alpine blocking (Trigo et al., 2002). In the eastern Mediterranean most cyclogenesis occurs over Cyprus (Alpert et al., 1990).

2.2 Methodology

2.2.1 EOFs and Principal Components

In a meteorological context, fields such as temperature, pressure, moisture, etc. are often given as discrete points in time and space. Longer sequences of measurements at multiple locations can be given as a matrix with time along one direction and space along the other. In linear algebra, there are ways to decompose matrices in order to simplify them. One of these ways is based on the set of vectors which are made up by the lines of a matrix. This set of n vectors with m components, if linearly independent, are the basis of a vector space. It is possible to obtain a different basis for the same vector space which consists of all orthogonal pairwise different vectors. In addition, the basis can be defined such that the original matrix can be as closely as possible represented by a linear combination of as few basis vectors as possible. The method of obtaining such a basis is the calculation of equivalent orthogonal functions (EOFs) and principal components (PCs).

This section shall not go into detail on how the calculation is done, but the curious reader can find a short but detailed summary of the usage of EOFs in meteorology in Hannachi et al. (2007) (for a more comprehensive explanation, see, e.g., Wilks, 2011). The main goal of the calculation of EOFs and PCs is to reduce the dimensionality of the problem. In meteorology, most data sets have a large number of data points and this method can help to identify underlying patterns which can be described using a largely reduced number of dimensions. When reconstructing the original fields, the contribution of additional EOFs change the outcome gradually less, allowing in many cases a sufficiently accurate description

of the full fields using a relatively (to the number of measurements) limited number of EOFs instead of the full data set.

In this section, multiple variables are used to account for multiple aspects of HPEs. The EOFs are calculated based on the 500 and 950 hPa geopotential and 950 hPa θ_e fields over the western Mediterranean. The atmospheric conditions are taken from ERA Interim (ECMWF re-analysis) data. For each of the fields the temporally averaged field for the corresponding date is used (00, 06, 12, and 18 UTC). Since the fields of geopotential and θ_e differ in their magnitude and variability, they are normalized before using them to calculate the EOFs. This is accomplished by subtracting the temporal mean and then dividing the data at each location by the standard deviation of the respective time series. The built in function of the NCAR¹ Command Language (NCL)² is then used to calculate the EOFs and PCs.

2.2.2 The k -means algorithm

The first two principal components form a two-dimensional vector for each event, equivalent to a point cloud in \mathbb{R}^2 . A clustering algorithm can then be used to find groups of points within this cloud. The algorithm chosen for the current climatology is the k -means algorithm (Hartigan and Wong, 1979), which is an iterative algorithm based on the distance between the points (see, e.g., MacQueen, 1967). The number of clusters has to be chosen beforehand (3 in this work). Before the first iteration, each of the n clusters is assigned a random centroid c_k . In the

¹National Center for Atmospheric Research

²<http://www.ncl.ucar.edu/>

first iteration, each point is assigned to the cluster of the closest centroid. After that, each iteration recalculates the position of each centroid such that

$$c_{n+1} = \frac{1}{K} \sum_{k=0}^K x_k, \quad (2.1)$$

where c_n is the centroid of the cluster at iteration n and x_k are the k members of the cluster. At each iteration the centroid is set to the mean of the cluster. After this operation, the distance of each point x_k to each centroid is checked and each point is assigned to the cluster whose centroid is closest to it. This process is repeated until no points change clusters. The energy of cluster n , E_n , is given by

$$E_n = \sum_{k=1}^K (x_k - c_k)^2 \quad (2.2)$$

and the total energy is

$$E_{tot} = \sum_{n=1}^N E_n, \quad (2.3)$$

where N is the total number of clusters. Each time the algorithm finds a configuration where no point changes clusters, the cluster configuration represents a local minimum of the function $E_{tot}(c_1, c_2, \dots, c_k)$. However, it is not necessarily the absolute minimum of the function. In fact, different initial configurations of the randomized centroids often lead to different configurations of the clusters with different values of E_{tot} . Usually, the aim is to obtain a robust configuration of clusters. One way to do this, is to repeatedly run the algorithm with different initial values (given by random seeds) and analyze the results with respect to their E_{tot} and the number of occurrences of each configuration. Both can be used as an objective measure of the robustness of the clustering. For this particular case, k -means was used with 100 different random seeds, all of which produced identical clusters.

2.3. SEASONAL DISTRIBUTION, FREQUENCY AND COMPOSITE FIELDS

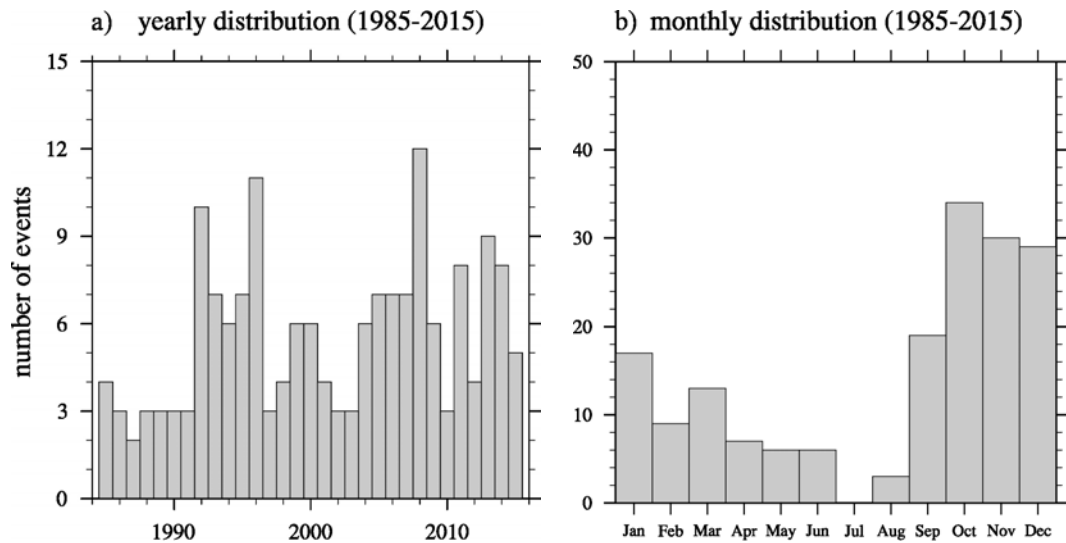


Figure 2.1: (a) Number of HPEs observed on Corsica each year from 1985-2015 and (b) monthly distribution. Total number of events $N = 173$.

2.3 Seasonal Distribution, Frequency and Composite Meteorological Fields

From 1985 to 2015 (31 years), 173 HPEs were identified. The criterion for an HPE is chosen at 100 mm of 06 to 06 UTC 24 hour accumulated precipitation observed by at least one surface station on Corsica. The analysis is limited to the 24 hour accumulated precipitation because the greater number of 24-hourly reporting stations provides a substantially larger sample (120-125 stations, depending on the year and event) compared to the hourly reporting stations (only around 25 stations). Each year between 2 and 12 events occurred with an average of 5.6 events per year (Fig. 2.1a). When viewed monthly (Fig. 2.1b), the typical distribution for a location in the Mediterranean emerges. Most of the events are observed in autumn and early winter, with October showing 34 events (19.6%). Of all events, 95 (55%) were observed between October and December (consistent with the findings of Gao et al., 2006; Kelley et al., 2012; Ricard et al., 2012).

2.3. COMPOSITE ANALYSIS AND HPE FREQUENCY

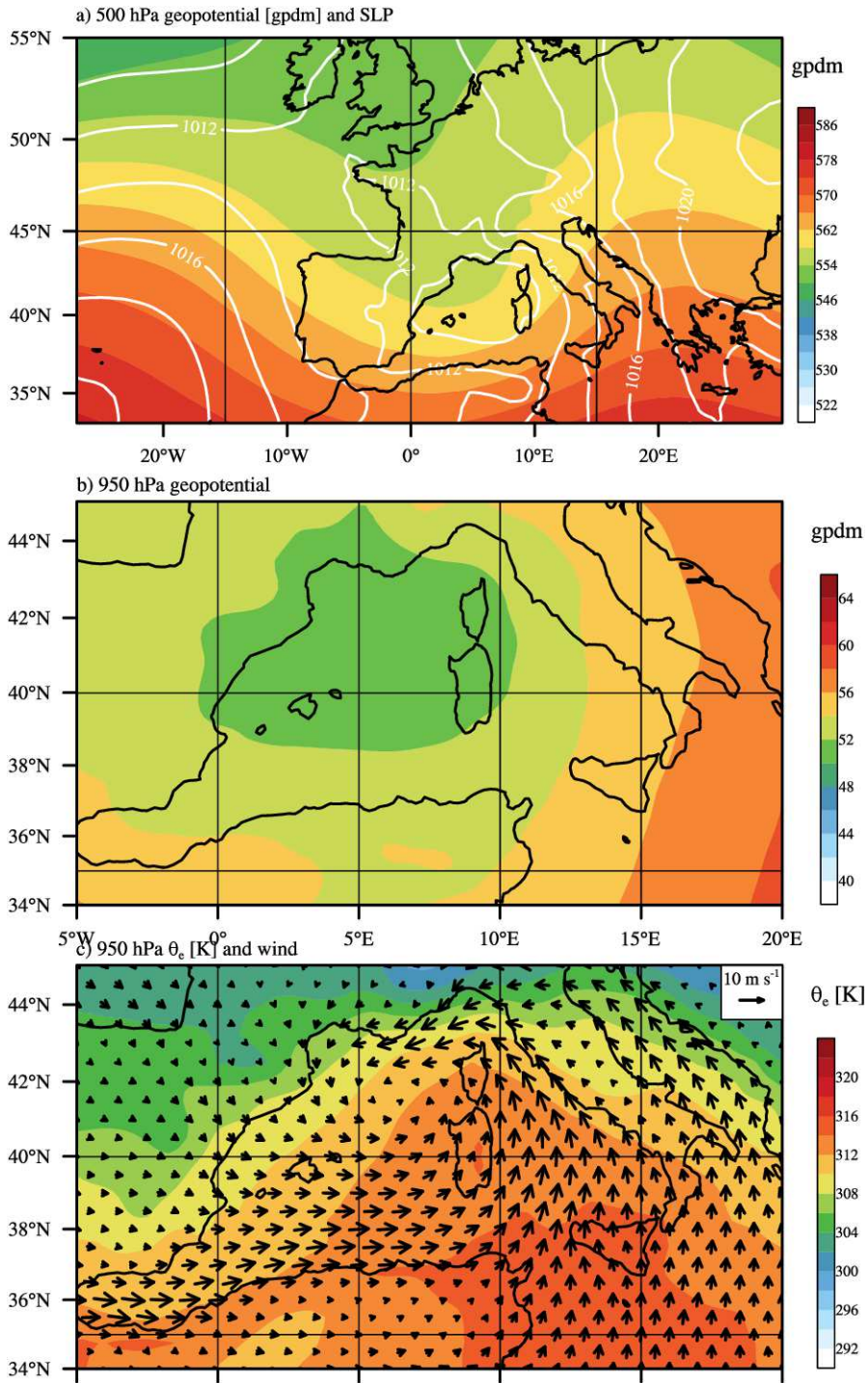


Figure 2.2: Composite fields for all 173 HPEs, (a) 500 hPa geopotential (color) and MSLP (white contours), (b) 950 hPa geopotential, and (c) 950 hPa θ_e (color) and wind (vectors).

For a direct comparison with the results of Ricard et al. (2012), Fig. 2.2 shows the composite fields, obtained by averaging the fields of all 173 events. The 500 hPa geopotential (Fig. 2.2a) shows a trough with its axis over western France and the Balearic islands. The trough in Ricard et al. (2012) was narrower and located further west. The surface low is located between Corsica, Sardinia and the Balearic islands. It is relatively weak, indicating a composite of lows at different positions which partly cancel each other. However, the composite field shows that the low is located west of Corsica in the majority of HPEs. The 950 hPa low (Fig. 2.2b) agrees well with the mean sea level pressure (MSLP) low. The corresponding circulation (Fig. 2.2c) induces a southerly wind over the Tyrrhenian sea, which advects warm and moist air north toward Corsica. The fields presented in Fig. 2.2 are less sharp than those found in the analysis of Ricard et al. (2012). This is due to a combination of factors, namely, the analysis of Ricard et al. (2012) was based on 8 events, whereas the fields in Fig. 2.2 are based on 173 events. The 8 events in Ricard et al. (2012) were observed from September to December, whereas the 173 events from this analysis are spread throughout the entire year.

2.4 EOFs

EOFs are obtained by purely geometric means and the physical interpretability of EOFs is greatly limited. In addition, they are generated using three normalized and equally weighed variables, resulting in values between -1 and 1, where the sign does not depend on the sign of the actual field (e.g. a low in a certain location can occur as a high in one of the EOFs). Nevertheless, the EOFs often contain interpretable information.

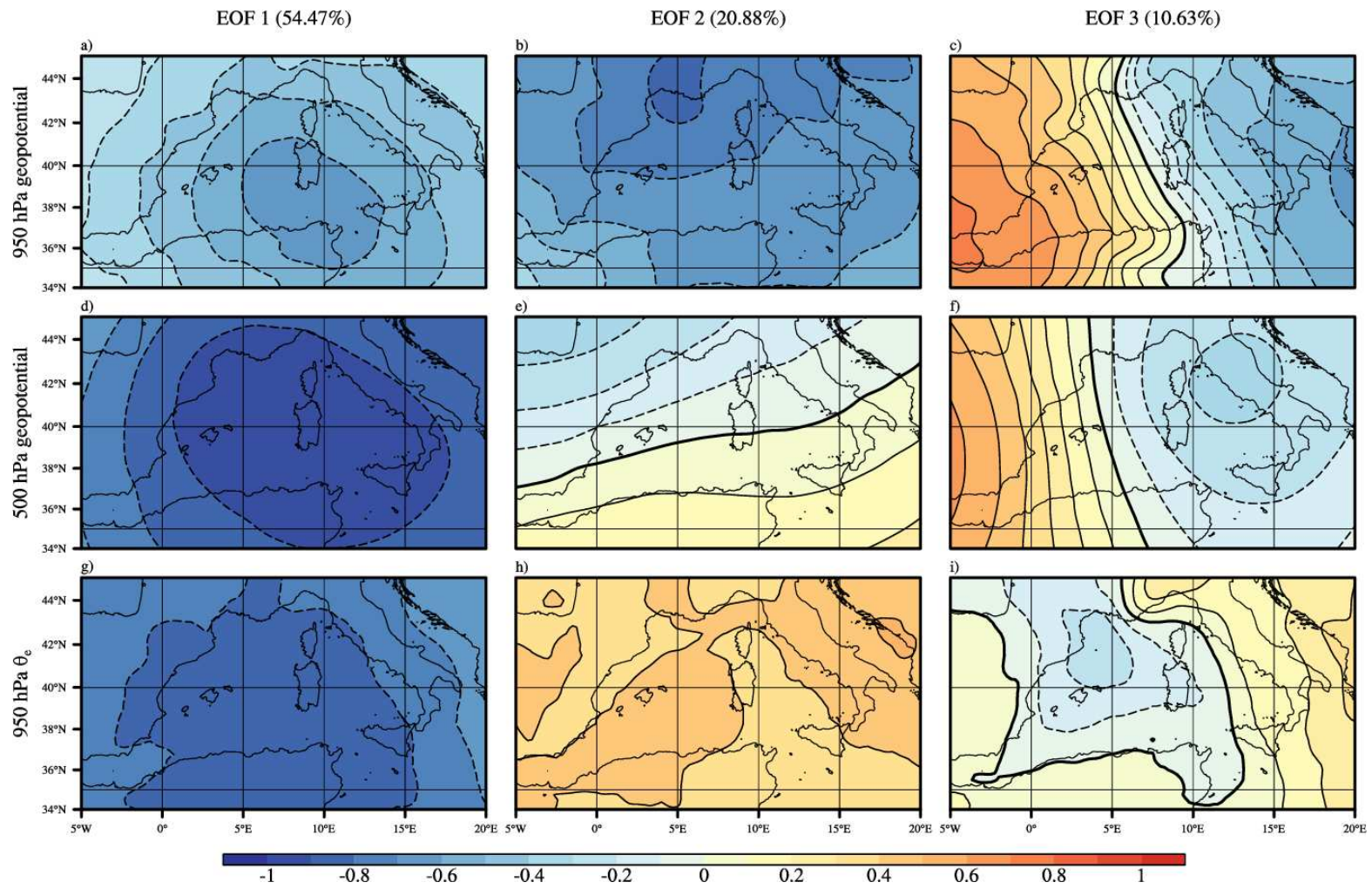


Figure 2.3: EOFs calculated from the normalized 950 (a,b,c) and 500 (d,e,f) hPa geopotential and 950 hPa θ_e (g,h,i) fields.

The first three EOFs calculated from each of the 3 fields are shown (Fig. 2.3). EOF1 (Fig. 2.3a, d, g) accounts for 54.47% of the variability and shows the 950 hPa cyclone south of Corsica with a cut-off over the western Mediterranean. EOF1 for θ_e shows an anomaly over the western Mediterranean with an inverted sign, since θ_e is usually higher over the sea during HPEs. EOF2 accounts for 20.88% of the variability. The 950 hPa EOF2 shows a low over the Gulf of Lion and southern France, whereas the 500 hPa EOF2 represents an upper level westerly flow over the western Mediterranean. The θ_e EOF 2 shows a positive anomaly extending from the strait of Gibraltar to the Gulf of Genoa and from there farther southeast over Italy and the Adriatic. EOF3 (Fig. 2.3c, f, i) only accounts for 10.63% of the variability. For the two geopotential fields a dipole indicates a contribution in the east-west position of the geopotential features, suggesting the predominant movement direction of cyclones and troughs. For θ_e EOF3 shows a cold anomaly over the Gulf of Lion which extends over large parts of the western Mediterranean, indicating a combination of the cold sector of Mediterranean cyclones and the mistral which is often observed when pressure over the western Mediterranean is low.

2.5 Clusters

Based on these EOFs and their first two principal components (Fig. 2.4), three clusters physically interpretable clusters were identified. All events are visualized as points in the normalized parameter space of their two principal components. In Fig. 2.4, the clusters are called Cluster 1 to 3, represented by the colors red, blue and green, respectively. Table 2.1 shows a list of the clusters with some key figures. The average precipitation in tab. 2.1 is the average over all 24 hour accumulated precipitation measurements from all HPEs of the cluster and all stations

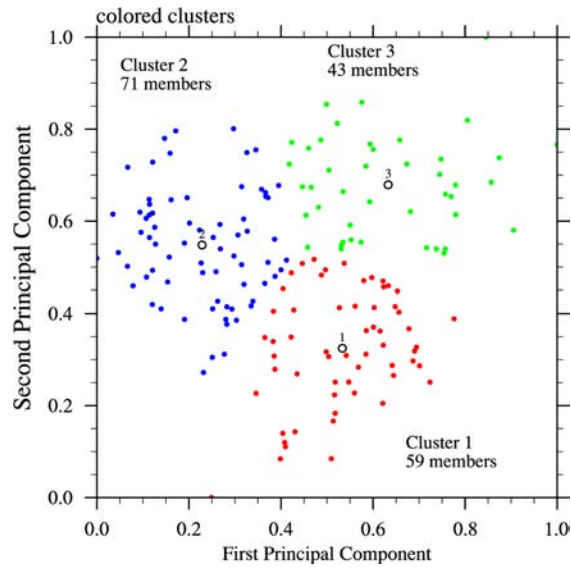


Figure 2.4: Clusters as found by k -means. The centroid of each cluster is marked by the black circular marker and the cluster number is indicated for each centroid.

on Corsica. The average maximum precipitation is the average of the highest observed precipitation for each event, i.e. the station with the highest value for each event. The last column shows the all time maximum observed precipitation for each cluster. While the autumn cluster produces the highest maximum values, the mixed cluster produces the highest average values.

The monthly distribution can be analyzed for each cluster separately (Fig. 2.5), which reveals seasonal differences between the clusters. Cluster 1 shows a clear peak in December (29.6%) with most events observed from November to January (63.4%). Cluster 2 shows most events observed from September to November (83.1%). In contrast to the clear seasonal peak of clusters 1 and 2, cluster 3 is relatively evenly distributed from October to May, placing its events mostly in winter and spring. Referring to this seasonal distribution, the cluster 1, 2, and 3 are named winter, autumn, and mixed cluster, respectively. The seasonal distribution shows that the events from cluster 2 are located over the warmest sea

2.6. PHYSICAL INTERPRETATION OF THE CLUSTERS

n	color	name	K	AP	AMP	MP
1	red	winter cluster	59 (34.1%)	29.1	152.4	247.6
2	blue	autumn cluster	71 (41.0%)	30.2	166.0	405.8
3	green	mixed cluster	43 (24.9%)	34.7	146.4	326.7

Table 2.1: List of clusters identified by k -means for the full sample (173 events in total), listing their average precipitation (AP), average maximum precipitation (AMP), and maximum precipitation (MP) in mm.

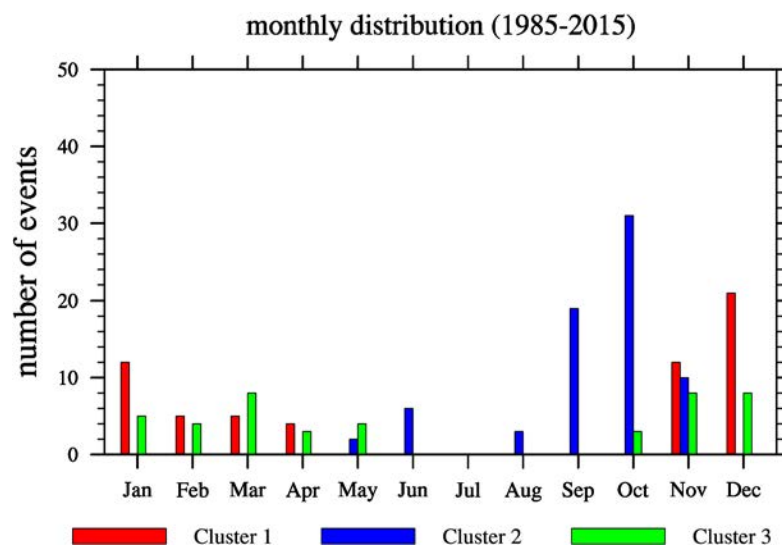


Figure 2.5: Number of HPEs (>100 mm) observed each month by cluster.

surface temperatures (SSTs), whereas the events in cluster 3 predominantly occur over low SSTs.

2.6 Physical Interpretation of the Clusters

2.6.1 Mean Fields

To physically interpret the clusters, their mean meteorological fields can be analyzed. Fig. 2.6 shows the 950 hPa composite fields averaged over all members of each cluster. All three clusters show a low over the western Mediterranean. The

low in the cluster 1 (Fig. 2.6a) is located east of the Balearic islands and shows multiple closed isohypses, pointing to a dominance of localized Mediterranean lows. In contrast, cluster 2 (Fig. 2.6b) shows its low over the Gulf of Lion, but it is open toward the northwest, indicating a stronger link to Atlantic lows. Cluster 3 (Fig. 2.6c) also shows a low over the Gulf of Lion. However, it is deeper than the low in cluster 2 and shows a weaker link to the low over the Atlantic.

Fig. 2.7 shows the 500 hPa geopotential and sea level pressure averaged over all members of each cluster. Note that this figure shows the fields beyond the limits used in the calculation of the EOFs, to provide a better overview of the synoptic situation. Cluster 1 (Fig. 2.7a), the winter cluster, shows a MSLP low centered just west of the Balearic islands which is on the eastern side of a trough over France and eastern Spain. The 500 hPa geopotential field shows weak gradients over western and central Europe, indicating a higher variability and partial canceling between the fields. The sea level pressure field for the autumn cluster (Fig. 2.7b) shows that the low over the Gulf of Lion is embedded in a larger low, which extends north over the British isles and the north Atlantic. The associated trough lies over western France and eastern Spain. Cluster 3 (Fig. 2.7c), the mixed cluster, shows a deeper low over the Gulf of Lion than cluster 2 (1003 hPa for cluster 3 vs. 1012 hPa for cluster 2), embedded within a larger low over France and the south of the British isles. This is in accordance with Trigo et al. (2002), who also found that cyclones over the Mediterranean often form due to a larger scale disturbances. The MSLP low is not only deeper but also larger, extending to the borders of the map in all directions. While the associated trough is at the same longitude as in the other two clusters, it is wider and its geopotential values are lower than in clusters 1 and 2. In summary, the events over warm SSTs (autumn cluster) are more localized and the cyclones are mostly found along the northern coast, while the mixed cluster is more strongly linked to large scale lows.

2.6. CLUSTER INTERPRETATION

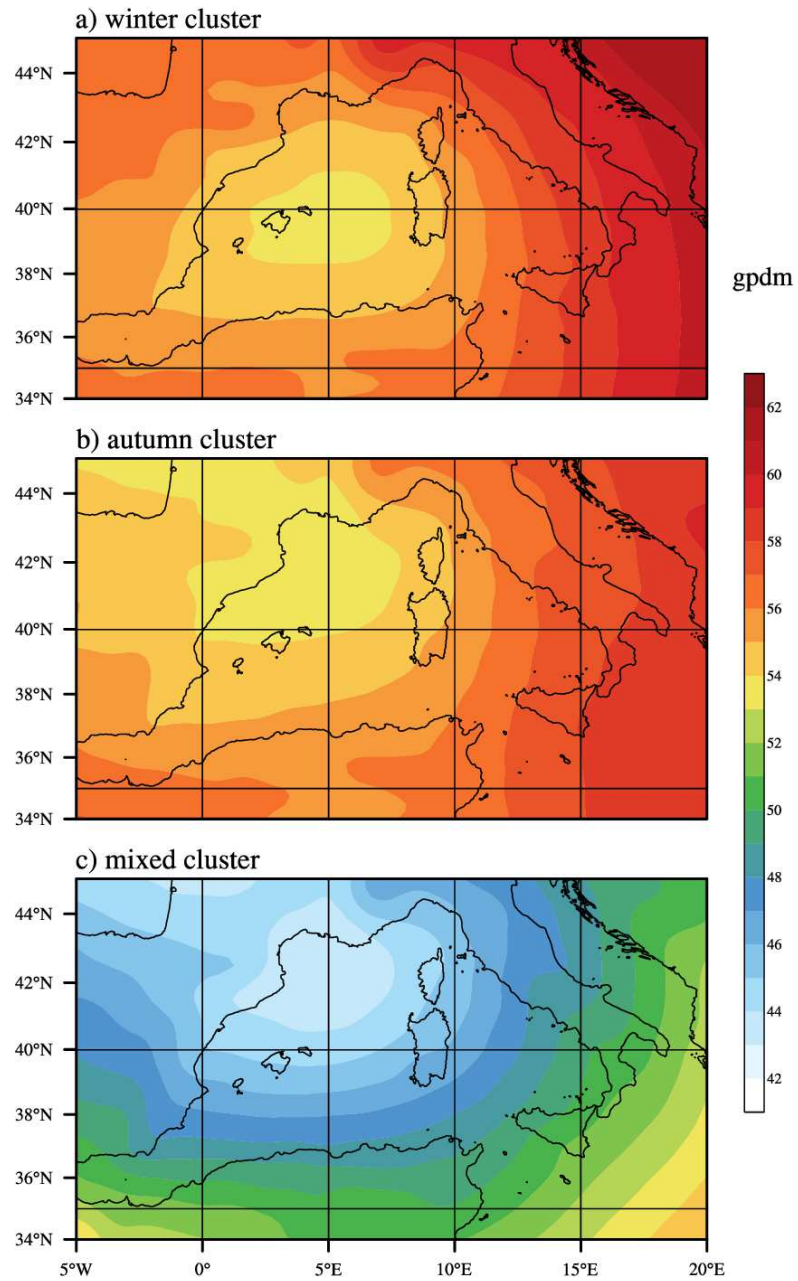


Figure 2.6: Average 950 hPa geopotential for each of the identified clusters.

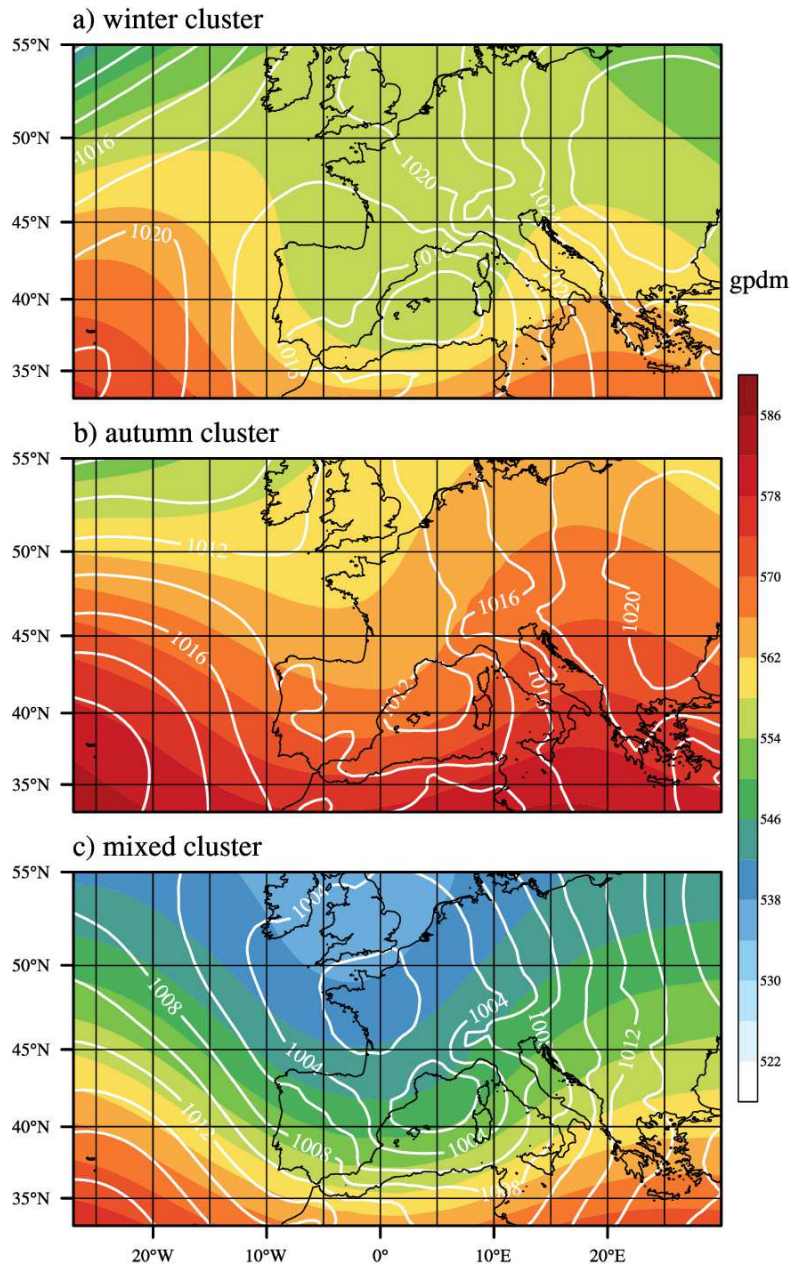


Figure 2.7: Mean 500 hPa geopotential (color) and sea level pressure (white contours) for each of the identified clusters.

An important factor for the location of heavy precipitation on Corsica is the wind, moisture and instability within the planetary boundary layer. Fig. 2.8 shows the wind and θ_e at 950 hPa. For all three clusters the warmest air is located south and southeast of Corsica. The warmest air is located over the sea with a θ_e gradient along the coast of the Mediterranean in all 3 clusters. The values of θ_e are strongly linked to the seasonal cycles seen in Fig. 2.5. All of them show southerly meridional wind with varying zonal wind. The winter cluster (Fig. 2.8a) shows the lowest values of θ_e and southeasterly flow over Corsica. The highest θ_e values are found in the autumn cluster (Fig. 2.8b), in accordance with the high SSTs observed during this time of the year. The wind has a weaker easterly component than in the winter cluster. The mixed cluster (Fig. 2.8c) shows southerly wind over Corsica with θ_e values close to but higher (by about 4 K) than the winter cluster.

2.6.2 Precipitation Distribution

After identifying a set of clusters with differing seasonal cycles and mean meteorological fields, this section explores the precipitation distribution within the clusters. In addition, differences in the spatial distribution of the mean and maximum precipitation is shown.

Figure 2.9 shows the point cloud from Fig. 2.4 with the points colored and sized according to the mean (a) and max (b) observed precipitation. The clusters are separated by lines and the average values are shown in the panels. The mean precipitation shows no drastic visual difference between the clusters, with the most striking feature being the only event for which >100 mm were observed in the autumn cluster. The mean values for the autumn and winter cluster are similar (30.19 and 29.11 mm respectively) whereas the mixed cluster shows 34.67 mm mean precipitation. The maximum precipitation (Fig. 2.9b), however, is different. While

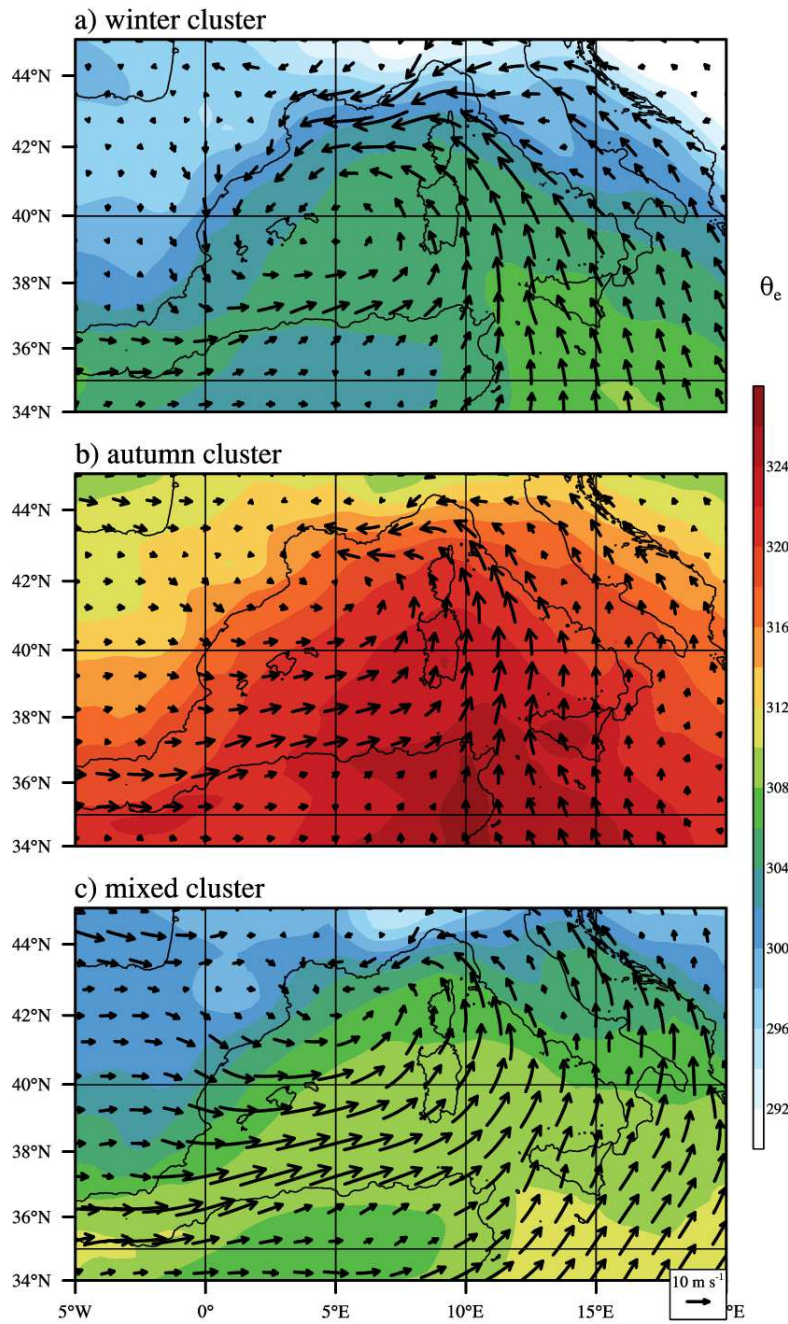


Figure 2.8: Average 950 hPa θ_e (color) and wind (vectors) for each of the identified clusters.

2.6. CLUSTER INTERPRETATION

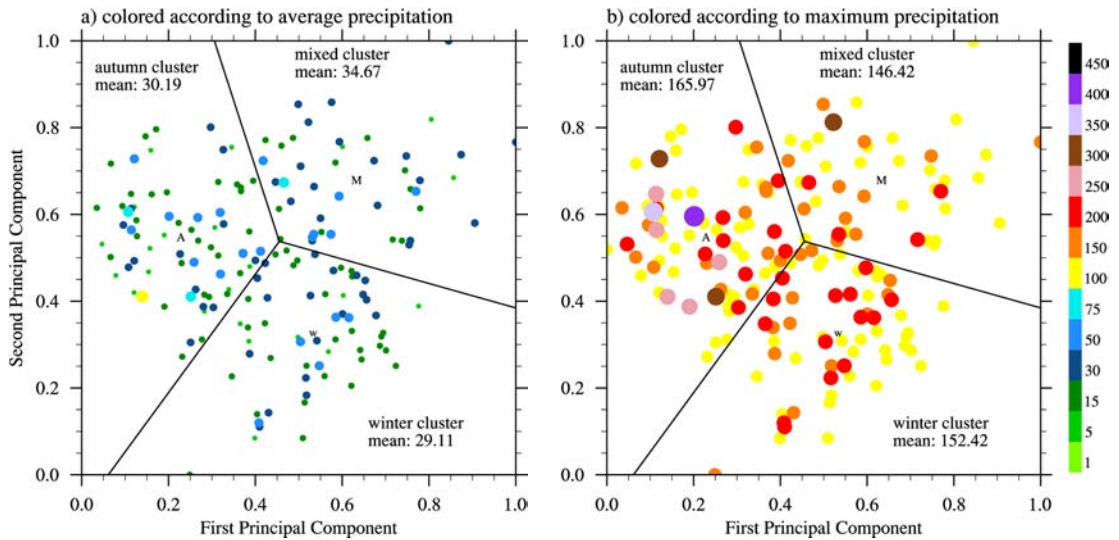


Figure 2.9: Points colored and scaled according to the observed average (a) and maximum (b) precipitation values for each event. The average in (a) is taken over all available stations on Corsica for each event. The clusters are separated by black lines and labeled accordingly. Their centroids are indicated by the capital letters A, W, and M, respectively.

the mixed cluster has the highest average precipitation, it has the lowest maximum precipitation. The highest maximum precipitation is found in the autumn cluster, which contains all but one events >250 mm. The events with the highest maximum precipitations are mostly found to the left, i.e. their PC1 is low.

The mean and maximum precipitation for all stations is shown in Fig. 2.10. The northwest of the island is more sparsely sampled, resulting in higher uncertainty of the precipitation distribution. This 'hole' in the observations is covered by high orography and bounded by high maximum values to its southeast (Fig. 2.10b). It is possible that higher precipitation is hidden by the absence of measurements in this region. However, Fig. 2.10, containing data from all 173 events, reveals a clear east-west gradient over Corsica for both, the mean and maximum precipitation.

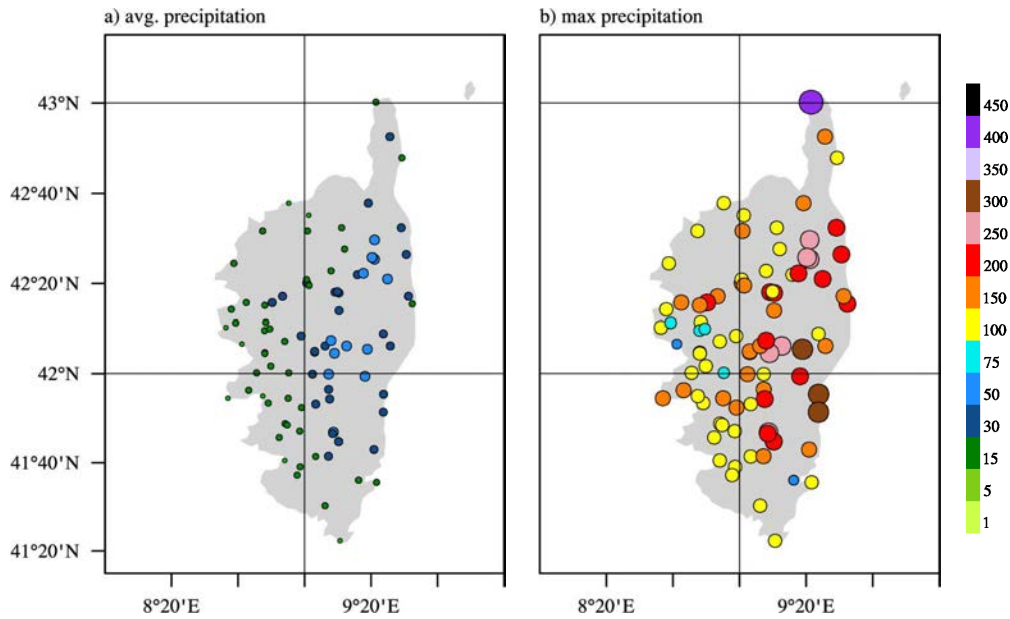


Figure 2.10: 24 hour mean and maximum accumulated precipitation observed at each point averaged over all 173 events.

Closer examination reveals that the mean precipitation is highest over the orography on the eastern half of Corsica, whereas the values along the coasts are slightly lower. This is consistently found along the entire east coast. However, the values along the east coast are still higher than those found over the west coast of the island. The maximum precipitation is somewhat more diffuse with high values (>250 mm) found over the orography but the highest values (>300 mm) seen along the coast and over the northern tip of Cap Corse. Overall, the distribution for all events reflects the easterly wind found in the majority of events.

Separating the mean and max precipitation by cluster (Fig. 2.11) reveals a more differentiated picture. The mean values (Fig. 2.11a-c) show a clear east-west gradient with the winter and mixed clusters concentrating the highest values over high orography. On the other hand, the high mean values in the autumn cluster (Fig. 2.11b) extend all the way to the east coast, indicating a lower dependence on orographic lifting. This is consistent with this cluster showing the highest

values of θ_e over the warmest SSTs and weaker cross mountain wind (Fig. 2.8b). Both factors allow precipitation to occur further upstream of orography (see, e.g., Miglietta and Rotunno, 2005). A similar distribution is seen for the maximum precipitation (Fig. 2.11d-f). However, while the highest mean values are found for the winter and mixed cluster, the most extreme events are mostly found in the autumn cluster. This confirms what was seen in Fig. 2.9. While the spatial distribution of the maximum precipitation is somewhat more diffuse than for the mean precipitation (i.e. high values are found along the coasts at some places), the rough distribution of orographic vs. coastal is also found for the maximum precipitation.

2.7 Discussion

The method used above contains a number of arbitrary elements, which impact the results. The fields used for the calculation of EOFs have to be selected. A multivariate approach based on three variables is presented in this study, but other possibilities exist. In addition, the clustering algorithm requires the number of clusters to be chosen beforehand. For this study, the results with two and four clusters were also examined but yielded less meaningful results. Specifically, of the four clusters two were insufficiently distinguishable for a robust physical interpretation, whereas two clusters separate the events into warm and cold events while allowing little distinction between their geopotential, pressure, and wind fields.

Moreover, the optimal number of clusters can vary depending on the fields chosen for the calculation of the EOFs. For instance, the same experiment was conducted using only the 950 hPa geopotential, which allowed to clearly distinguish four different clusters, differentiated mostly by the position of the cyclone. On the

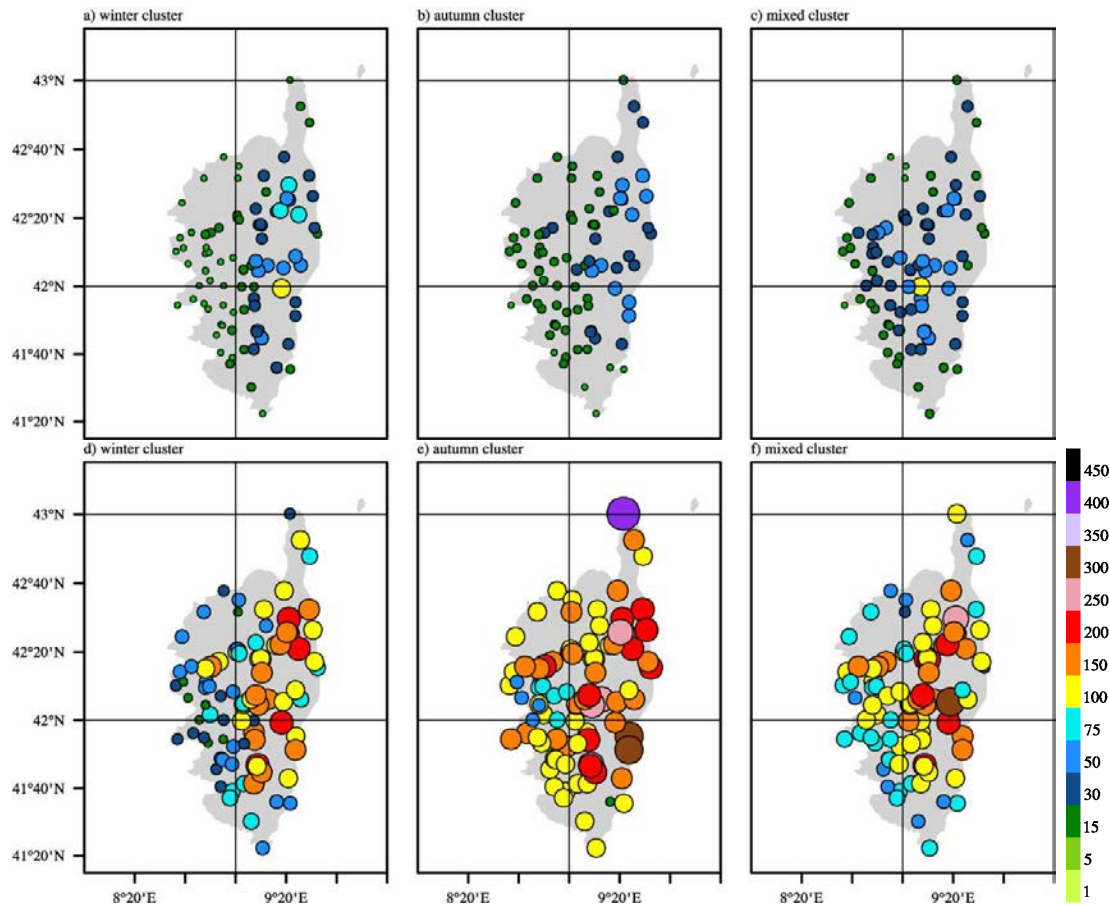


Figure 2.11: Mean (a,b,c) and maximum (d,e,f) observed 24 hour accumulated precipitation for each cluster.

other hand, three of these four clusters lacked a clear seasonal cycle and a distinct spatial distribution of precipitation on Corsica. However, basing the method purely on the 950 hPa geopotential identifies a cluster which corresponds to a Corsican low, i.e. a low centered just east of Corsica. This corresponds to a class of event which has been repeatedly observed over Corsica. It will be shown that the first case presented in this work, 4 September 2012, is an example for such a Corsican low. For the clusters presented above, the addition of θ_e allows to identify a clear seasonal cycle at the cost of clear spatial separation between the lows of each cluster.

While the above used method yielded the same cluster configuration for all 100 random seeds, other selections of variables, cluster numbers, observation times and even subsets of HPEs yield up to 13 different cluster configurations. Different configurations obtained by the same configuration do not necessarily correspond to the same physical interpretation. The domain was chosen over the Mediterranean to specifically address the mesoscale conditions around Corsica during HPEs. This comes at the cost of partially ignoring the large scale synoptic situation. While the identified clusters allow consistent physical interpretation, two clusters (autumn and mixed) show a signature of large scale cyclones over the north Atlantic and a signature of a Mediterranean cyclone at the same time. A test with a larger domain was able to separate large and Mediterranean cyclones but in turn reduced the differences between the clusters over Corsica. Since the latter is the focus of this study, the usage of the above presented domain is justified.

2.8 Conclusions

A 31 year precipitation climatology for HPEs (>100 mm in 24 h) reveals that most HPEs over Corsica are observed from September to January with the intense season being October to December with 55% of all events. It also reveals only few HPEs are observed during the summer with only 10 events from June to August (zero in July). The ECMWF analysis fields over the western Mediterranean were used to calculate EOFs for the 173 HPEs and a principal component analysis using the k -means algorithm separated three clusters of events, which show clearly different seasonal cycles, such that an autumn, winter and mixed cluster were identified.

The autumn cluster contains the most extreme events but shows also the lowest mean values over the orography. The winter cluster shows the lowest θ_e values in the boundary layer but the strongest easterly wind over Corsica, resulting in

precipitation well aligned with the orography of the island with much higher values over the eastern half of the island. On the other hand, the mixed cluster shows a mean southwesterly wind over southern Corsica. Consequently, its mean precipitation is found further west with the highest values still found over the highest orography over the eastern half of Corsica. The majority of all HPEs affect the eastern half of Corsica, predominantly the mountains along the east coast. Fewer and less extreme events are found over the western half of Corsica.

Chapter 3

Numerical Tools and Used Observations

Some of the tools used in this work depends on the initial findings for each case and will not be described in this section but in the chapters where the cases themselves are discussed. Nevertheless, there is a number of tools used for more than one case, which are described below. This includes the description not only of the comparison and analysis methods but also the description of the data sets used for comparison and the configuration of the numerical model. Most methods listed below are standard methods frequently used in the analysis of HPEs.

3.1 Meso-NH Simulations

3.1.1 Model Configuration

The Meso-NH model (Lafore et al., 1998) version 5.1.3 is used to simulate the heavy precipitation events over Corsica. The simulation are run with a horizontal grid spacing of 2.5 km and a vertical grid spacing between 30 m above the ground

3.1. MESO-NH SIMULATIONS

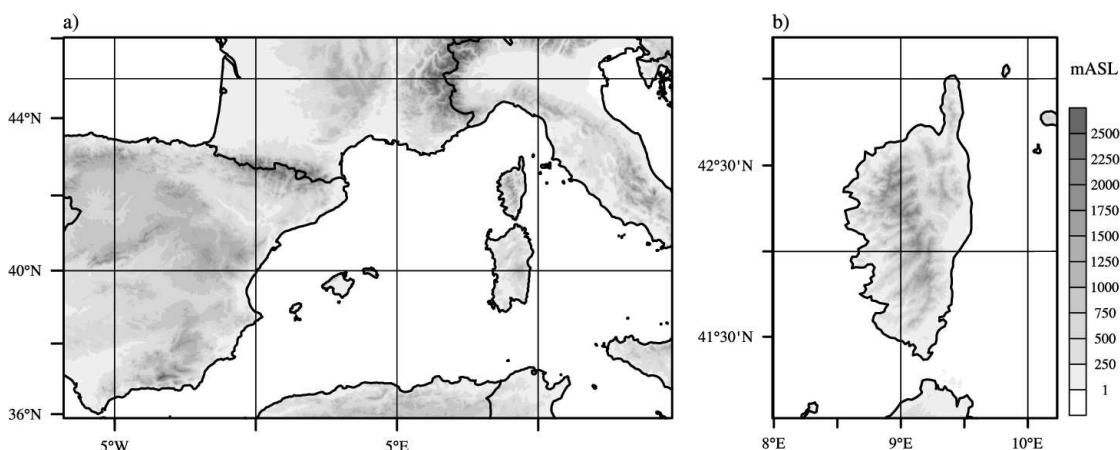


Figure 3.1: Map of the Meso-NH domain setup showing Domain 1 (a) and the nested Domain 2 (b).

and 700 m at the model top. When a nest is used, the inner model is run with a horizontal grid spacing of 500 m and the same vertical levels as the outer model. The outer model is run on Domain 1 (Fig. 3.1a), which includes the entire western Mediterranean to provide good coverage of any synoptic pattern in the vicinity of Corsica. The inner model is run on Domain 2 (Fig. 3.1b), which is centered over Corsica. Domains 1 and 2 have a size of 720 by 450 by 50 and 375 by 500 by 50 grid points, respectively. The moderate computational costs of these domains permits to obtain an ensemble of simulations for each case.

The time steps are 60 s (4 s) for the outer (inner) model, respectively, for cases 1 and 2, and 30 s (5 s) for the outer (inner) model for case 3. Where nests are used, the model is run with 2-way nesting. Atmospheric water is treated by the ICE-3 microphysics scheme (Lascaux et al., 2006; Pinty and Jabouille, 1998). Meso-NH includes SURFEX (Masson et al., 2013), a sophisticated surface model, which is responsible for any surface fluxes. No deep convection parametrization is used and shallow convection is handled by the Kain-Fritsch scheme (Kain, 1993). Long wave radiation is treated by the Rapid Radiation Transfer Model scheme (Mlawer et al., 1997) and short wave radiation parametrization is based on Fouquart and Bonnel

(1980). Cuxart et al. (2000) contains a description of the model's turbulence scheme. The scheme is used in its 1D version in Domain 1 and in its 3D version in Domain 2. The mixing length is based on Bougeault and Lacarrère (1989). For the nested simulations, additional tests are performed using a mixing length based on Deardorff (1972).

3.1.2 Simulation Ensembles

Due to the chaotic nature of the atmosphere, two simulations of the same event will generally diverge. Meso-NH is programmed in a manner that prevents this from happening if the same simulation is run twice with different numbers of computational cores. This property is called bit reproducible, because the simulation output will be identical bit by bit. However, any other change to the simulation (including running it on a different computer) will unavoidably introduce growing perturbations and eventually lead to diverging results. While this property of simulations seems vexing at a first glance, it is actually used in research by creating ensembles of simulations. An ensemble is a number of simulations of one event, each run slightly different from the others. The end result represents multiple possibilities of how the simulated event could have developed over time.

There are multiple approaches to ensemble simulations, i.e. the method of introducing perturbations to simulations. One of the simplest methods is to simply add small amplitude random noise to one or several model fields before running the simulation. In practice, however, other methods are more commonly used. The ECMWF for example uses a sophisticated method to identify the perturbations to its initial fields that will have the largest impact on the forecast after 48 hours (Leutbecher and Palmer, 2008). In the case of mesoscale models, the initial conditions are usually taken from a model with a larger domain. This allows the usage of the ensemble provided by the larger scale model (used for example by

3.1. MESO-NH SIMULATIONS

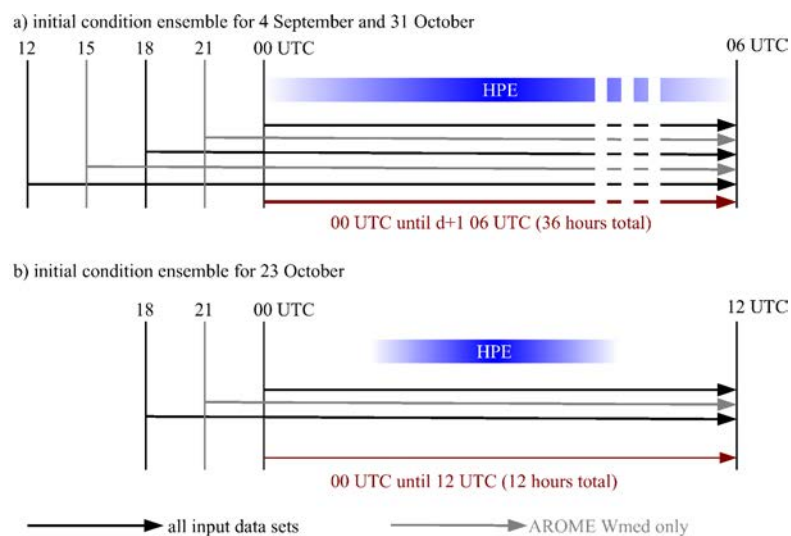


Figure 3.2: Schematic of the initial condition ensembles used for the cases of 4 September and 31 October (a) and 23 October (b). Black arrows show simulations which are conducted for all three input data sets (ECMWF, ARPEGE, and AROME-WMed) while gray arrows show simulations conducted exclusively using AROME-WMed data.

Hanley et al., 2011). An ensemble can also be obtained by using different input data sets (Ducrocq et al., 2002), using different parameterizations for processes like microphysics, surface or cumulus convection (Tapiador et al., 2012), or randomly perturbing one parametrization scheme (Fresnay et al., 2012; Hally et al., 2014a,b). Thus, an ensemble can be obtained by changing the initial or boundary conditions of the model or changing the model itself or a combination thereof.

In the course of this work, the initial conditions of the model are changed by starting it from different input data sets and at different times. Figure 3.2 shows a schematic diagram of the initial condition ensembles. Three input data sets are used, namely the ECMWF, ARPEGE, and AROME-WMed analyses. The first two, ECMWF and ARPEGE, are global data sets and as such they have a relatively large horizontal grid spacing of about 10 and 15 km, respectively. AROME WMed is the same model as AROME France. It is a convection permitting spectral model

Exp. Name	start time	coupling interval	4 Sep	23 Oct	31 Oct
AW 00-3	d 00 UTC	3 h	✓	✓	✓
AW 21-3	d-1 21 UTC	3 h	✓	✓	✓
AW 18-3	d-1 18 UTC	3 h	✓	✓	✓
AW 15-3	d-1 18 UTC	3 h	✓		✓
AW 12-3	d-1 18 UTC	3 h	✓		✓
AW 00-6	d 00 UTC	6 h		✓	
AW 18-6	d-1 18 UTC	6 h		✓	
EC 00-6	d 00 UTC	6 h	✓	✓	✓
EC 18-6	d-1 18 UTC	6 h	✓	✓	✓
EC 12-6	d-1 12 UTC	6 h	✓		✓
AR 00-6	d 00 UTC	6 h	✓	✓	✓
AR 18-6	d-1 18 UTC	6 h	✓	✓	✓
AR 12-6	d-1 18 UTC	6 h	✓		✓

Table 3.1: List of tests performed with different starting times and input data sets. The starting time indicates either the day of the HPE (d) or the day before (d-1) and a time in UTC. They are named according to the model which provides the initial and boundary conditions (AW for AROME-WMed, EC for ECMWF and AR for ARPEGE).

run at a horizontal grid spacing of 2.5 km and was run specifically for the HyMeX campaign with a domain centered over the western Mediterranean. In addition, Meson-NH is started at different times, increasing the number of available input data sets.

Figure 3.2 shows that the simulations were initiated between 00 UTC on the day of the HPE and 12 UTC of the day before. The ECMWF and ARPEGE analyses are available every 6 hours and the AROME WMed analysis is available every 3 hours. The naming of the ensemble members consists of two letters for the input data set (**AW**, **EC**, and **AR** for AROME WMed, ECMWF, and ARPEGE, respectively), two digits indicating the initiation time and one digit for the coupling interval. The initiation time in table 3.1 is given with either d (day of the event) or d-1 (day before the event). The coupling interval is given because for the case of 23 October the impact of the coupling interval on the simulation results was tested.

For instance, **AW 18-3** is the simulation initiated from AROME WMed data on the day before the HPE at 18 UTC with a coupling file every three hours. This nomenclature is consistent for all presented cases. Case 3 includes an ensemble based on random perturbations of the model physics, which is explained in the respective section. If any other named simulations are conducted, their names are given in the respective sections.

3.1.3 Experiments with Modified Orography

In addition to the ensemble simulation, the sensitivity of the HPEs to orography is tested. This is achieved by running the simulation after flattening Corsica to sea level. In all simulations where orography is modified manually, only the terrain height is modified while all other surface parameters remain unchanged, e.g. land use data or parameters used for the calculation of drag. While this is not entirely realistic, it simplifies the process of changing the orography greatly and is sufficient to explore the resulting differences.

Since the input data field does never perfectly align with the orography in Meso-NH, the preprocessing extrapolates down to the surface where atmospheric data are not available. Usually, this is mainly used to obtain initial conditions within valleys which are not resolved in the input data set but present in the Meso-NH simulation. Therefore, the volume of air whose values are extrapolated is usually low. However, when removing an entire mountain range, the volume becomes significant and the extrapolation distance is increased from usually around a few hundred meters up to more than 2 km. For the case of 23 October, the removal of Corsica caused the model to replace the orography with highly unstable air. Specifically, the extrapolation placed a pool of warm and moist air above the flattened island which had CAPE values exceeding 5000 J kg^{-1} . This unstable air resulted immediate convection after the initiation, consequently placing a large

cold pool over Corsica, which partly replaced the orography and resulted in similar results as seen in the reference simulation.

To remove the highly unstable air, a rectangular box was placed around the island and all moisture values within this box were bilinearly horizontally interpolated onto the grid over the flattened island. This change was sufficient to suppress the initial spurious convection. For the other two cases, 4 September and 31 October, the same problem was not found and the extrapolated values from Meso-NH preprocessing are used instead.

A further test for 23 October was conducted by blocking the northeasterly inflow of cold air into the Mediterranean basin. This was achieved by increasing the height of the mountain ranges along the Italian coast. Gaussian bell shaped mountains with a maximum height of 3000 m were added to the reference terrain height, resulting in a barrier with a height of between 3500 and over 4000 mASL. Lower mountains were tested but were unable to block the inflow of air until the end of the HPE.

3.2 Observational Data and Comparison Methods

This section lists the data used to verify the simulation results and the methods used in the comparisons. Along with the observational data several statistical methods are described and their strengths, weaknesses and limitations are discussed.

3.2.1 Precipitation - Surface Stations and Radar

Due to the focus of this study, verification and evaluation relies heavily on precipitation data. While precipitation is simple at a first glance (How much does it rain, where, and when?), its verification is in fact rather complicated. The distribution of rain in space and time is an extremely important parameter because flooding is a major cause of damage, injuries and even fatalities in severe weather events. A large portion of the verification and statistical methods is therefore used to compare observed and simulated rainfall.

Depending on the location, the availability of observations can drastically limit verification. Even over areas with a relatively dense observational network mesoscale models with horizontal grid spacings around 1 km produce a lot more pseudo rain observations than are available from real measurements. For example, the 2.5 km horizontal grid, which is used in most of the simulations discussed in this work, covers Corsica with more than 1300 grid columns, far beyond the density of any measuring network. The Météo France rain gauge network on Corsica provides data for 106 locations on the island for the 24 hour period from 06 to 06 UTC (for 4 September and 31 October) and for the case of 23 October, where hourly data are required, only 25 rain gauges are available, allowing the direct verification of only around two percent of all model grid points. In certain cases the spacing between the rain gauges exceeds the dimensions of the relevant features in the precipitation field, drastically limiting their usefulness for model verification. To address this problem, Météo France offers gridded precipitation data for the HyMeX SOP 1 which were obtained from radar data. While these are less accurate than rain gauge measurements they provide dense observations and reveal the precise location of small scale high precipitation areas even where no rain gauges are available, i.e. over the sea or between the surface stations.

For verification purposes, several methods are available. Arguably the simplest method is to overlay the observed precipitation onto the simulated precipitation fields for a visual comparison. Its simplicity is the greatest strength of this method and depending on the desired precision, it can be sufficient. It allows to easily identify zones of heavy simulated and observed precipitation and obvious errors in model precipitations are easy to find. However, especially for ensemble simulations this method is problematic, as the differences might be more subtle than what can be seen with the naked eye. Even if differences are apparent, their interpretation is highly subjective and a quantitative analysis is preferable to obtain an objective measure of the forecast accuracy.

One more method used in this work is the comparison of accumulated precipitation over time over a certain area. This area depends on the individual event because the spatial distribution of precipitation can vary greatly for different events. Multiple variations of this methods are used. For comparability model precipitation is interpolated to observation points where hourly data are available and the average over a zone of interest is taken. However, this method is greatly limited by the amount of available hourly rainfall data points within the averaging zone. As mentioned above, only 25 such stations are available on Corsica. For a localized event like 23 October, not a single station fully captured the main event, preventing any meaningful comparison between model and station data. For this case the same method was used with radar estimated precipitation data. The gridded precipitation field of the radar estimated precipitation provides an observation for almost all grid points, allowing the usage of a simple mean value over an area of interest. The downside is the limited accuracy of the radar estimated precipitation. Such a comparison trades off accuracy for the advantage of higher spatial resolution.

3.2.2 Satellite Data

Satellites are a valuable source of observational data for meteorologists around the world. Their position allows them to capture data over a large surface quickly, allowing them to provide gridded data which can easily be used for figures and statistical methods. While satellites measure a wide range of parameters such as temperature, rain, moisture, long and shortwave radiation, wind speed, ocean wave height and others, the parameter used herein is brightness temperature.

In its general sense brightness temperature T_b is a measure of the temperature of a black body. The amount of energy emitted as electromagnetic waves of a certain wavelength depends only on the temperature of a black body. For the atmosphere, things are not quite as simple. Firstly, neither the earth's surface nor the atmosphere and the clouds are perfect black bodies. Secondly, radiation from within the atmosphere could in theory have been emitted at any point along the line of sight. To circumvent this problem, the absorption properties of different ingredients of the atmosphere are used. The 10.8 μm infrared band is of particular interest to meteorologists because it is absorbed by clouds while clear air is transparent at this wavelength. Thus the source of the 10.8 μm radiation is either the earth's surface or the cloud top, allowing to measure their temperature (König et al., 1999). The brightness temperature is not a variable inherent to weather models and it has to be calculated separately. The Radiative Transfer for Tiros Operational Vertical Sounder (RTTOV) (Saunders et al., 2005) is available with the Meso-NH diagnostics and it allows to calculate a wide range of simulated satellite observations.

3.2.3 Radiosoundings

Radiosoundings, i.e. weather balloons, and profilers are two methods of obtaining information on the vertical structure of the atmosphere. This is especially useful for stability and vertical wind shear, which are essential factors in the organization of convection but also determine the behavior of air flow over or around an obstacle. A radiosounding is obtained by launching a balloon with sensors attached. Generally it takes around one to two hours for a weather balloon to reach its highest level, where it bursts and the sensor falls back to the surface. During this time, the balloon travels with the environmental wind, and depending on the conditions it can travel up to hundreds of kilometers.

Even under calm conditions, a radiosounding is not a strictly vertical profile, nor are all the measurements taken at the same time. However, in comparisons with model data they are often compared to single vertical columns of model data of one time step. While simplicity is certainly an important reason for that choice, it is justifiable. In most cases the vertical variability of the atmosphere is greater than the horizontal variability, meaning that even a highly tilted measuring path can be close to the values a purely vertical profile would have yielded. Nonetheless, this should be kept in mind when comparing details of observations and model output.

On Corsica, two operational radiosoundings are launched every day at Ajaccio at 00 and 12 UTC (see Fig. 1.2). In addition, the KIT launched extra radiosoundings during IOP 15c and IOP 18. The latter soundings are available multiple times per day in intervals of two to three hours for two of the three cases presented in this thesis. They were used for verification purposes in both IOPs, even though their measurements are only presented for IOP 18 (31 October).

3.3 Statistical Methods

One way to achieve a more quantitative comparison is to calculate the correlation between two fields. A commonly used parameter is Pearson's product-moment coefficient r , which is given by

$$r = \frac{1}{n\sigma_x\sigma_y} \sum_{i=1}^n (x_i - \bar{x})(y_i - \bar{y}), \quad (3.1)$$

where n is the number of points, σ_x and σ_y are the standard deviations and \bar{x} and \bar{y} are the means of the samples x and y . The coefficient is limited to $[-1, 1]$ and values of 1 (-1) show perfect linear correlation between the two data sets. A high correlation tends to indicate a better agreement between observations and simulation, but it is limited to the available observations. Values of exactly 1 (-1) indicate that a linear function of the type

$$y(x) = kx + m \quad (3.2)$$

where y and x are the sample values and k and m are constants. However, r can at times be a misleading parameter when used for precipitation verification. For a precipitation field with the same shape and location but a 90% underestimation r could theoretically be equal or very close to 1. On the other hand a simulated precipitation field with perfect agreement in shape and quantity but a spatial displacement will not yield a value of 1. Even though such configurations are highly theoretical and extremely unlikely, pure correlation is not sufficient to determine the performance of a simulation and r is best used in addition to other methods. In addition r does not measure bias. In the above example the bias would be m .

Two particular problems when using r over Corsica is the relatively low number of hourly reporting rain gauges and the absence of observations over the sea. With

n in the denominator Eq.3.1 is more susceptible to the impact of isolated outliers for smaller sample sizes. For precipitation events close to or over a coast r can be strongly influenced by a displacement of the bulk of precipitation over the sea, where it is not captured by rain gauges.

To address the fact that r ignores some errors, the difference between simulation and observation can be taken directly into account using the root mean square error (*RMSE*). It is given by

$$RMSE = \sqrt{\frac{1}{n} \sum_{n=1}^N (x - y)^2} \quad (3.3)$$

where x and y are two samples (e.g. simulated and observed precipitation). Both over- and underestimation contribute positively to the *RMSE* such that errors in opposite direction can not cancel. However, just like r the *RMSE* counts a horizontal displacement of the precipitation field as two errors, summing up both the positive and the negative errors of the respective zones. While pattern recognition algorithms for this problem do exist, they are not used in this study. Where it is necessary, visual comparisons are shown and explained.

The mean absolute error (*MAE*) is similar to the *RMSE* in that it is a measure of the unsigned error. It is given by

$$MAE = \frac{1}{n} \sum_{n=1}^N |x_i - y_i|, \quad (3.4)$$

where x_i are the simulated values and y_i are the observations. In contrast to the *RMSE*, the *MAE* does not use the square of each individual error, resulting in the same weight of every value. Both, *MAE* and *RMSE*, are always greater or equal to 0. For a perfect simulation, both, *MAE* and *RMSE*, would be equal

to 0 while higher values indicate larger errors. To get a measure of the over- or underestimation, the normalized bias NB is used, given by

$$NB = \frac{\sum_{k=1}^n x_i}{\sum_{k=1}^n y_i}, \quad (3.5)$$

which is the ratio of the means of two given samples. If y are the observations and x are the simulated values in the above example, values of $NB > 1$ show an overestimation and $NB < 1$ show an underestimation of the simulated precipitation. A hypothetical perfect simulation would have a value of $NB = 1$.

Taylor (2001) proposed a method to show three statistical parameters in one diagram. Firstly, the centered pattern $RMSE'$

$$RMSE' = \sqrt{\frac{1}{N} \sum_{n=0}^n [(x_n - \bar{x}) - (y_n - \bar{y})]^2} = RMSE - \overline{RMSE} \quad (3.6)$$

where

$$\overline{RMSE} = \bar{x} - \bar{y} \quad (3.7)$$

is the overall bias, i.e. the difference between the means of the two samples. Secondly, the cross correlation coefficient r . Thirdly, the standard deviations σ_x and σ_y , which are related to $RMSE'$ and r by

$$RMSE'^2 = \sigma_x^2 + \sigma_y^2 - 2\sigma_x\sigma_y r, \quad (3.8)$$

allowing them to be plotted into one single diagram called Taylor diagram (after Taylor, 2001). Figure 3.3 shows an example of such a diagram for 31 October 2012 using an ensemble of Meso-NH simulations compared to rain gauge observations. Each dot represents a member of the ensemble for a total of 11 simulations. The size of the dot cloud represents the dispersion between the different members of

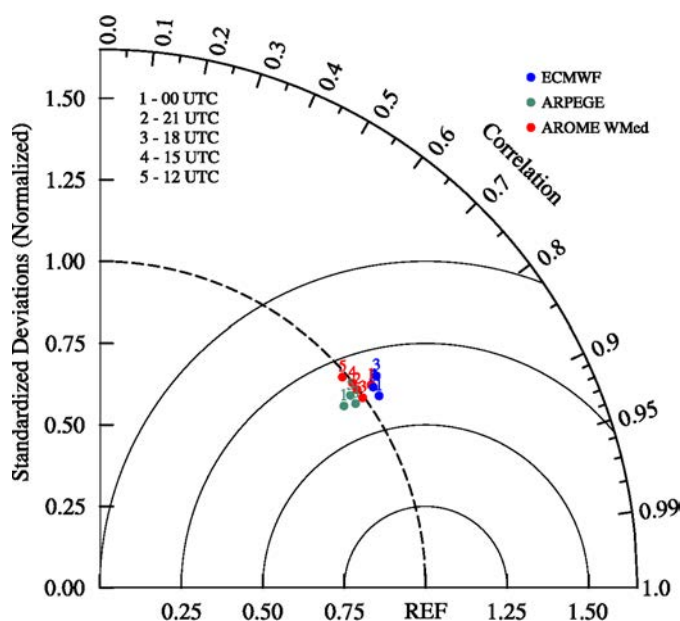


Figure 3.3: Example Taylor diagram for 31 October 2012 for 06-06 UTC 24 hour accumulated precipitation over the entire model domain (N=4088).

the ensemble. In this example dispersion is relatively small. Comparing smaller samples will tend to show higher dispersion. This is analogous to the effect that precipitation forecasts tend to be less reliable for small areas and shorter time periods. Figure 3.3 shows r as the azimuthal angle and the standardized deviations (σ_y/σ_x) as radius. The concentric circles are lines of constant $RMSE'$. A theoretical perfect simulation would be shown directly along the x-axis at the tick mark labeled REF ($r = 1$, $RMSE = 0$, $\sigma_y/\sigma_x = 1$). However, Taylor diagrams do not show the overall bias $\bar{x} - \bar{y}$. Where necessary in later chapters, the range of the x and y-axis of the Taylor diagrams is increased to accommodate the larger spread of ensemble members.

3.4 A Simple Cyclone Tracking Algorithm

In general, tracking cyclones is not trivial and large efforts are necessary to reliably track multiple forming and dissipating depressions over time. However, in the case of a single depression and a limited amount of time such an algorithm can be relatively simple. The method described below relies on two assumptions, namely (i) there is only one cyclone in the area of interest and (ii) the movement speed of the cyclone is limited. For such conditions a manually marked pressure minimum can easily be tracked over time.

Initially, the pressure field needs to be smoothed strongly to guarantee that there are not multiple local minima within the vicinity of the cyclone. This is achieved by calculating the moving average over the pressure field p_{smooth} by

$$p_{smooth} = \frac{1}{(2d + 1)^2} \sum_{i=i_0-d}^{i_0+d} \sum_{j=j_0-d}^{j_0+d} p \quad (3.9)$$

where p is the pressure field, d is the averaging distance in grid points, and i and j are the coordinates along the x and y direction. For $d = 1$ the above formula is equivalent to a classic unweighted 9-point average over a 2D field. However, the algorithm requires $d \gg 1$. The goal is to remove any secondary minimum in the pressure field and retain only the signal of the cyclone, which is relatively large compared to all other signals. Since d is a number of grid points, its value depends not only on the size of the phenomenon that is being tracked but also on the horizontal grid spacing Δx and Δy . Values of $d\Delta x \sim 75 \text{ km}$ work well for the application to the MSLP fields in this work and are used where cyclone tracks are shown.

For simplicity reasons the approximate initial position of the cyclone is defined manually. The algorithm then looks for a minimum in the pressure field within the vicinity of the given location. It then shifts the scanning box over the minimum

that it finds and looks for a minimum in the pressure field of the following time step within a maximum number of grid points from the initial minimum. This tracks a cyclone properly as long as the local minimum of the cyclone is also the global minimum within the scanning box. The algorithm does not work if a cut-off low transforms into a shortwave trough, i.e. it loses its local minimum. For the limited number of cases and simulations a manual quality control of the tracked cyclone centers is feasible, which allowed to easily develop an NCL script which was able to track the cyclones.

In addition to the above mentioned comparisons, the model data are further analyzed beyond simple comparisons to observations. This helps to gain further insight, as model output data contains a lot of information beyond what can be observed both in spatial and temporal extent as well as density. Even though most of this information can not be directly verified. it is generally assumed that if a simulation agrees well with observations where it can be verified, it represents the physical processes and qualitative development of the simulated event. Thus the model fields and their wealth of data are used to improve the understanding of the physical processes involved in a wide variety of simulated events.

Chapter 4

Case 1: 4 September 2012 - A Quasi-Stationary Cyclone

The HPE of 4 September 2012 is analyzed in this chapter. The event took place one day before the start of HyMeX SOP1 and was therefore not part of an IOP. Consequently, the study is limited to operational observations. First, the synoptic situation, observed precipitation and brightness temperature are shown to illustrate the development of the event. Then, an initial condition ensemble of the event is run and its results are discussed. Among the members of the initial condition ensemble, a reference simulation is chosen, which is used for a more in-depth analysis of the event and as a starting point for higher resolution simulations. Lastly, the results of a simulation with flattened orography over Corsica are presented.

4.1 Synoptic Situation

The event of 4 September 2012 was associated with a large quasi-stationary cut-off whose core remained in the vicinity of Corsica and Sardinia during the entire

duration of the analyzed period, from 4 September 00 UTC until 5 September 00 UTC. In fact, the cut-off developed over the bay of Genoa on 1 September, when it separated from a trough which lay over central Europe. The subsequent development of a cyclone over the bay of Genoa is exemplary for HPEs over the northwest of Italy and such cyclones are referred to as Genoa lows. Such events are known to cause heavy precipitation along the coast of northwestern and central Italy, over Corsica, Sardinia, and also further inland along the south side of the Alps.

The cyclone which caused the HPE of 4 September 2012 slowly circled Corsica counterclockwise starting from 1 September, its center reaching Sardinia on 4 September. This movement corresponds to a path length of approximately 500 km over more than 72 hours and a movement speed of only around 6.5 km h^{-1} . While the cut-off weakened continuously from 1 to 5 September and precipitation was observed throughout this entire period, the heaviest precipitation on Corsica and Sardinia was observed starting from the early morning of 4 September.

Figure 4.1a shows the cut-off core over northern Sardinia with the corresponding surface low about 200 km southeast, as seen in the ECMWF operational analysis. The closed isohypses around the cut-off extend to southern Germany in the north. It covered the entire western Mediterranean with a geopotential minimum of about 563 gpm (Fig. 4.1a). The surface low had a minimum pressure of 1012 hPa in the ECMWF analysis. In the boundary layer (Fig. 4.1b) the cyclonic rotation is clearly visible. The θ_e field shows warm moist air present around Corsica and Sardinia as well as south of 40° north. Northerly and northwesterly inflow over continental France advects colder air, visible as blue plume over the gulf of Lyon. Warmer air from east of the trough is advected over the Apennines. The wind vectors show that the cyclone forced this warm moist air toward the east coast of Corsica, where the highest precipitation values were observed for this

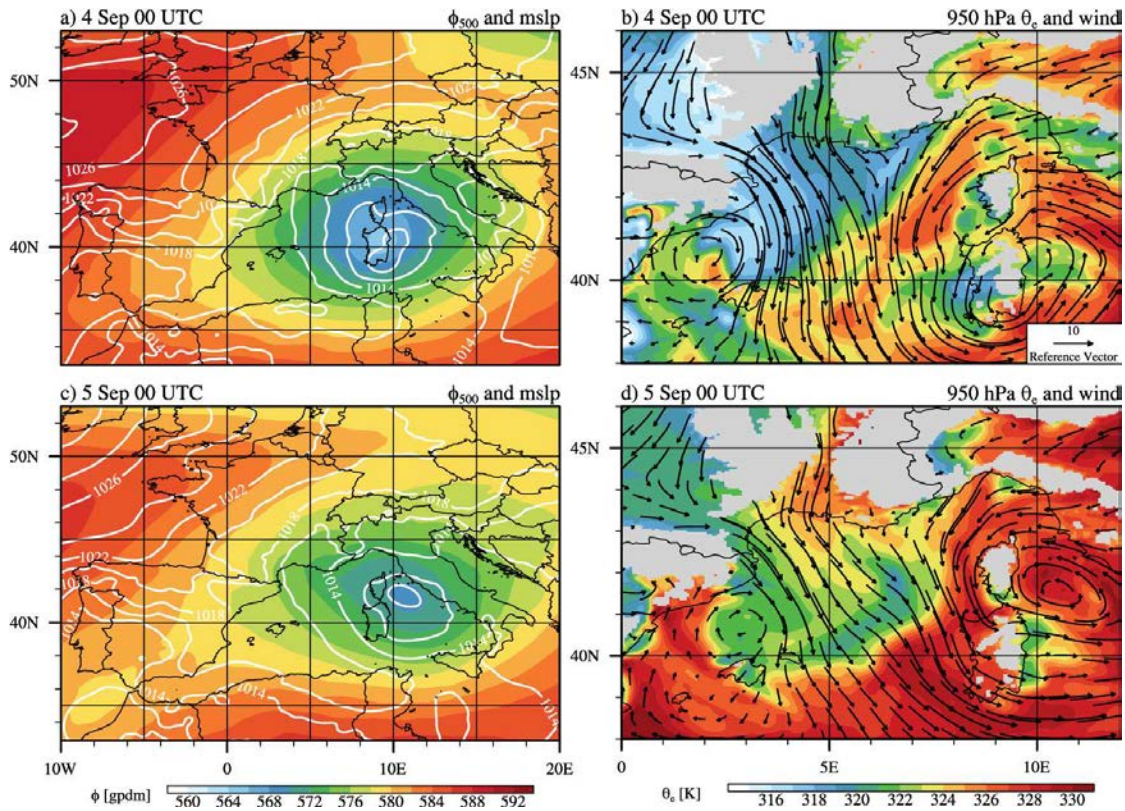


Figure 4.1: Synoptic Situation at 00 UTC of 4 and 5 September over the western Mediterranean as seen in the ECMWF analysis. 500 hPa geopotential and sea level pressure (a, c) and 950 hPa θ_e and wind (b, d).

HPE. The warmest inflow is found along the northern part of Sardinia's and the southern part of Corsica's east coast.

During the 24 hours from 4 to 5 September 00 UTC the surface and the upper level center of the cyclone moved slowly northeast (Fig. 4.1c). From the low level wind speed (Fig. 4.1d) it is visible that at this time the west coast of Sardinia was exposed to warm moist northwesterly wind. The easterly flow toward the Corsican orography was confined to the northern half of the island's coast. The θ_e field also shows increased values of θ_e compared to 24 hours earlier (compare Figs. 4.1b and d). Such a warming is not surprising. During the fall, the SST of the Mediterranean sea are at their maximum, lagging the solar radiation maximum by

around three months. Especially the presence of cold air aloft, as in the case of a cut-off or trough passing over the warm water, leads to increased evaporation. The moistening and warming of the boundary layer beneath relatively cold mid and upper level air leads unstable conditions which are favorable for the development of heavy precipitation.

4.2 Observed Evolution

4.2.1 Satellite Images

Figure 4.2 shows the observed brightness temperature every 6 hours for the HPE of 4 September, starting at 00 UTC. Figure 4.2a shows convection over the southeast of Corsica with additional cells located off-shore east of the island. Smaller patches of low T_b are scattered around the Corsica to its west, northwest, and east as well as over northern and central Italy. During the next 12 hours (Fig. 4.2b and c) convection between Italy and Corsica remains almost stationary with some weakening over the island itself. At 18 UTC (Fig. 4.2d) around Corsica the cold cloud tops ($<-40^\circ\text{C}$, yellow and orange) have significantly reduced in size and number. At 5 September 00 UTC (Fig. 4.2e) convection has restrengthened over the northern half of Corsica's east coast where it remains for the rest of the HPE. Convection is weakening but remains visible at 06 UTC (Fig. 4.2f).

4.2.2 Observed Precipitation

Figure 4.3a-e show the 6 hour accumulated precipitation observed by surface stations (filled circles) and estimated by radar (color). While both the surface stations and the radar estimated values are consistent with the event, there are discrepancies between the two data sets. The radar estimated values are slightly too high

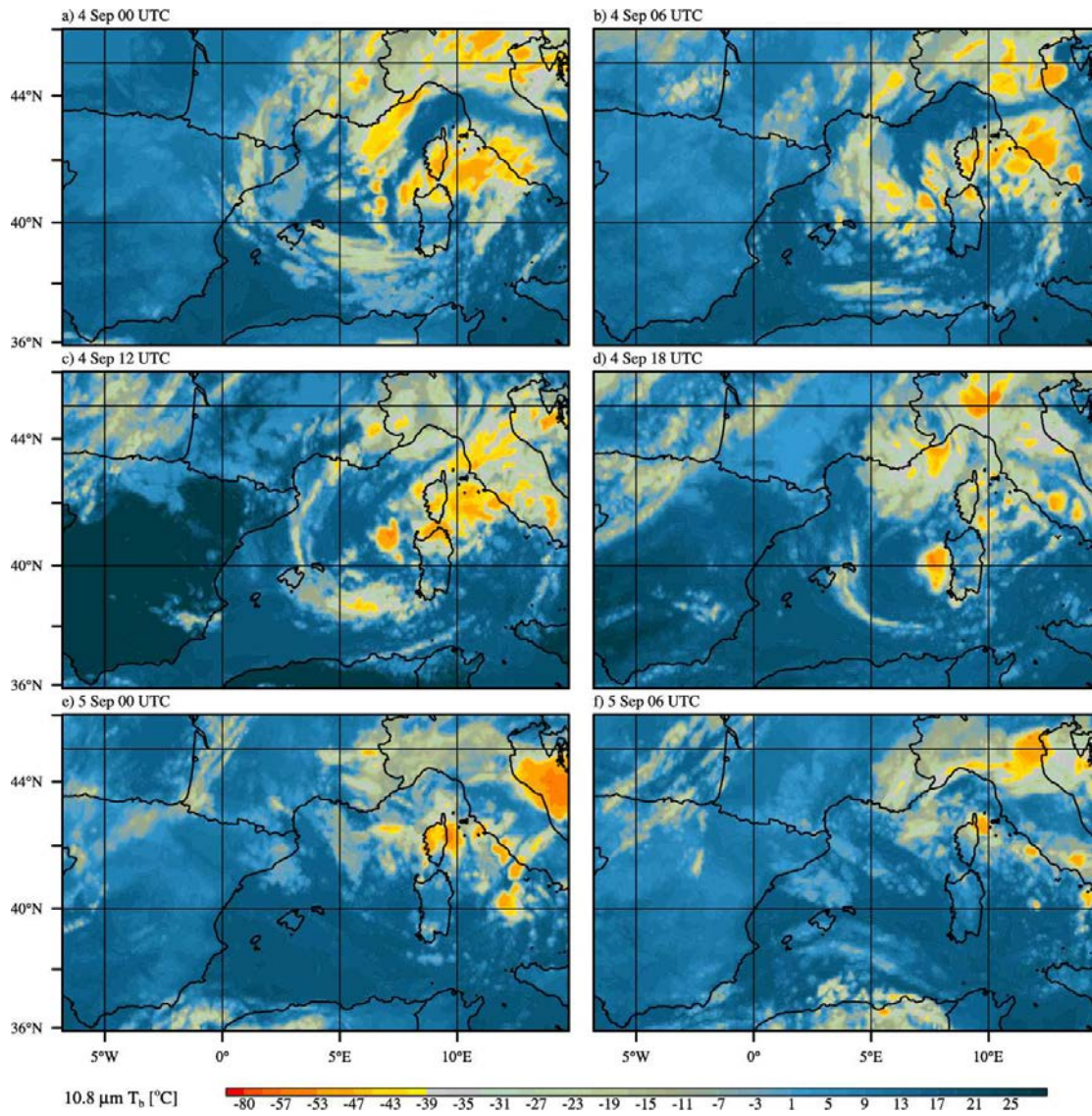


Figure 4.2: $10.8 \mu\text{m}$ brightness temperature [$^{\circ}\text{C}$] every 6 hours from 4 September 00 UTC to 5 September 06 UTC.

4.2. OBSERVED EVOLUTION

along the east coast and too low over the west of the island, where the line of sight of the Aleria radar is blocked by orography for the lower levels. A radar station at the coast of the French mainland in Collobrières samples the west of Corsica and the sea between Corsica and the mainland. However, it is about 200 km from the island, allowing it to observe only the upper levels. The northwest of Sardinia is too remote from the radar in Collobrières and shaded by orography from the radar in Aleria, resulting in virtually no observed precipitation over this area for the radar estimated data set. In contrast, the rain gauges show precipitation over the northwest of Sardinia throughout all phases of the HPE.

Fig. 4.3a shows the accumulated values from 00 to 06 UTC of 4 September. The observed precipitation was strongest along the southern and central east coast of Corsica, which is consistent with the cyclone center lying northeast of Sardinia and causing northeasterly inflow which was strongest over the south of Corsica. From 06 to 12 UTC (Figs. 4.3b) the southern half of the east coast continued being hit by the heaviest precipitation with more than 100 mm of precipitation estimated by from radar data. However, those values are contradicted by the surface stations along the east coast, which show values below 50 mm only. The 6 hour accumulated surface station data are relatively scarce and the radar estimated values show localized regions of valued >100 mm which are small enough not to be captured by any surface station. While the absolute values of the radar estimated precipitation are to be taken with caution, they still show a small scale variability in the rain field which is not captured by the rain gauge network. It is therefore reasonable to assume that the stations in Figs. 4.3a-e did not necessarily capture the highest values for this HPE.

From 12 to 18 UTC precipitation weakened somewhat, remaining below 50 mm over most of Corsica. Once again, this figure shows the importance of the radar estimated data, which shows more intense precipitation over the southern half of

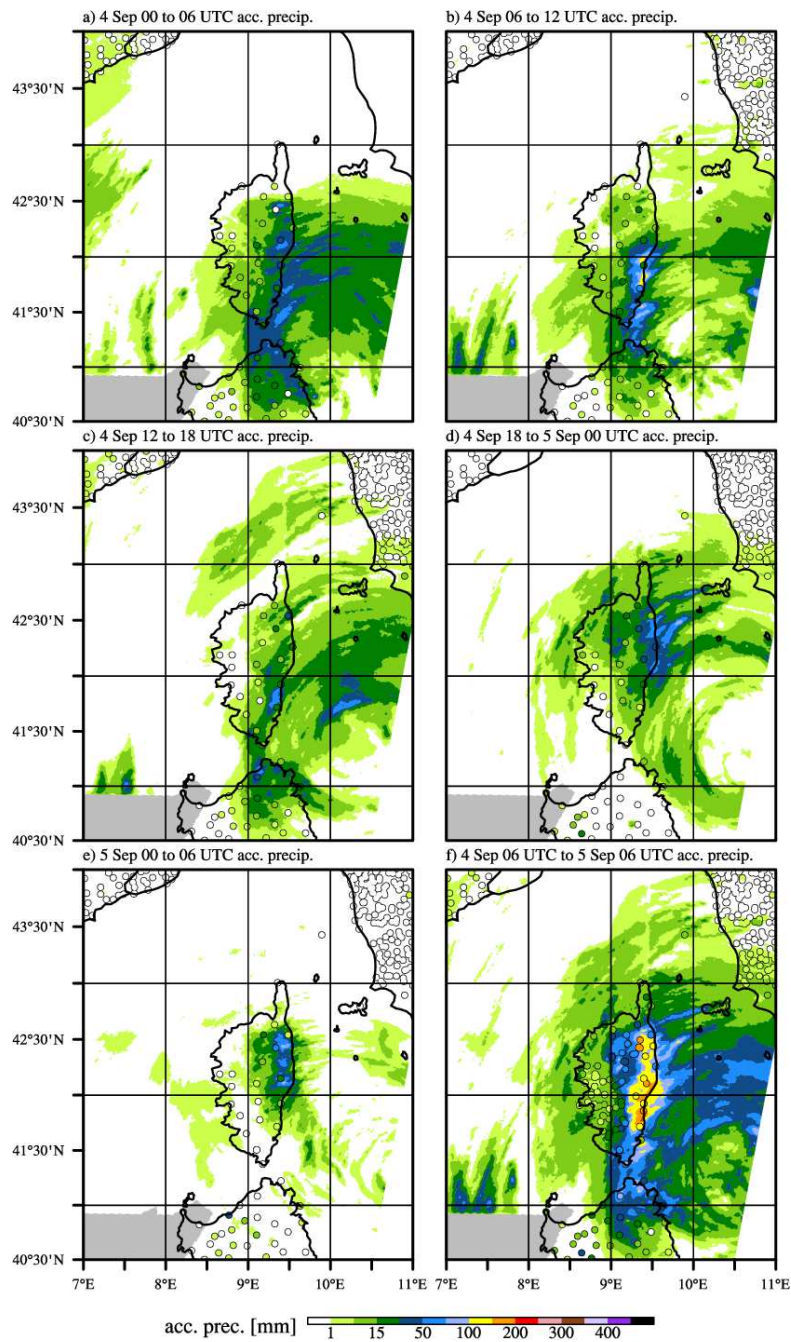


Figure 4.3: Rain measured by surface stations (circles) and estimated from 5 minute radar data (color) over Corsica for the event of 4 September. Panels a to e show 6 hour accumulated rain for the 6 hour periods from 4 September 00 UTC to 5 September 06 UTC. The 4 September 06 UTC to 5 September 06 UTC accumulated rain is shown in f.

4.2. OBSERVED EVOLUTION

the east coast of Corsica. From the stations alone, the strongest precipitation would clearly be located over the northern half of the east coast with the only station on Corsica showing over 25 mm of precipitation being located over the northeast of Corsica.

After 18 UTC (Fig. 4.3d) the highest precipitation is clearly located over the northeast of Corsica. While inconsistencies are still found between the radar estimated data and the surface stations, both agree on the location of the heaviest precipitation over the northern east coast of the island. Just like before, localized regions of high precipitation are seen by the radar between the individual surface stations.

During the morning of 5 September (Fig. 4.3e) precipitation remained over the northern half of the east coast of Corsica. However, the radar shows the most intense precipitation further inland than during the previous phases. For the period of 00 to 06 UTC of 5 September the terrain shading in the radar data over northwestern Sardinia is most apparent with one station exceeding 25 mm of rain while the radar observed below 1 mm. The precipitation observed by the surface stations over northwestern Sardinia is consistent with the northwesterly inflow shown in the ECMWF analysis of 5 September 00 UTC (Fig. 4.1d).

The 24 hour accumulated precipitation in Fig. 4.3f shows that while the entire island was affected by the HPE, values over 100 mm occurred only over the east coast of the island.

4.3 Initial Condition Ensemble

4.3.1 Spatial Distribution of 24 Hour Accumulated Precipitation

The first goal is to obtain a simulation which reproduces the event as well as possible. Therefore, an ensemble of 11 simulations is run with varying initial conditions and lateral boundary conditions from three different models and with variable starting times. Table 3.1 in Sec. 3.1.2 shows which simulations were conducted for the initial condition ensemble of 4 September. In total, the starting time varies between 3 September 12 UTC and 4 September 00 UTC. Figures 4.4 and 4.5 show the 24 hour accumulated precipitation observed (Fig. 4.4a) and simulated (others). In addition, Pearson's product-moment coefficient r is calculated for every ensemble member based on a comparison of the rain gauges on Corsica and the simulated precipitation for the 24 hours between 4 and 5 September 06 UTC. This allows to benefit from the higher number of 24-hourly reporting stations.

All ensemble members share the signatures of moving convective cells which are organized around a common center of rotation. This pattern is the result of the cyclone's rotation and its slow movement. The pattern gives some indication as to where the center of the cyclone was located during the accumulation period. For all ensemble members but one (**AW 12-3**, shown in Fig. 4.4f) this center of rotation lies east-southeast of Corsica. **AW 12-3** is also the simulation with the highest simulated precipitation, exceeding the observed values over the central mountain range by up to 250% (>250 mm instead of <100 mm). In addition, all ensemble members show increased precipitation over the Corsican orography but none of them achieves the concentration along the coast which is seen in Fig. 4.4a.

Common to all simulations is a precipitation maximum away from the coast over central Corsica, where the orography is tallest. All simulations overestimate this secondary maximum while underestimating the rain along the northern half of the east coast of the island. With respect of the predominant wind direction, this corresponds to a downstream (westward, inland) shift of the precipitation in the initial condition ensemble. As a first quantitative indicator, the Pearson's product-moment coefficient r is shown for every simulation, it varies between 0.39 and 0.76 for the comparison with the rain gauges on Corsica (observation points visible in Fig. 4.4a).

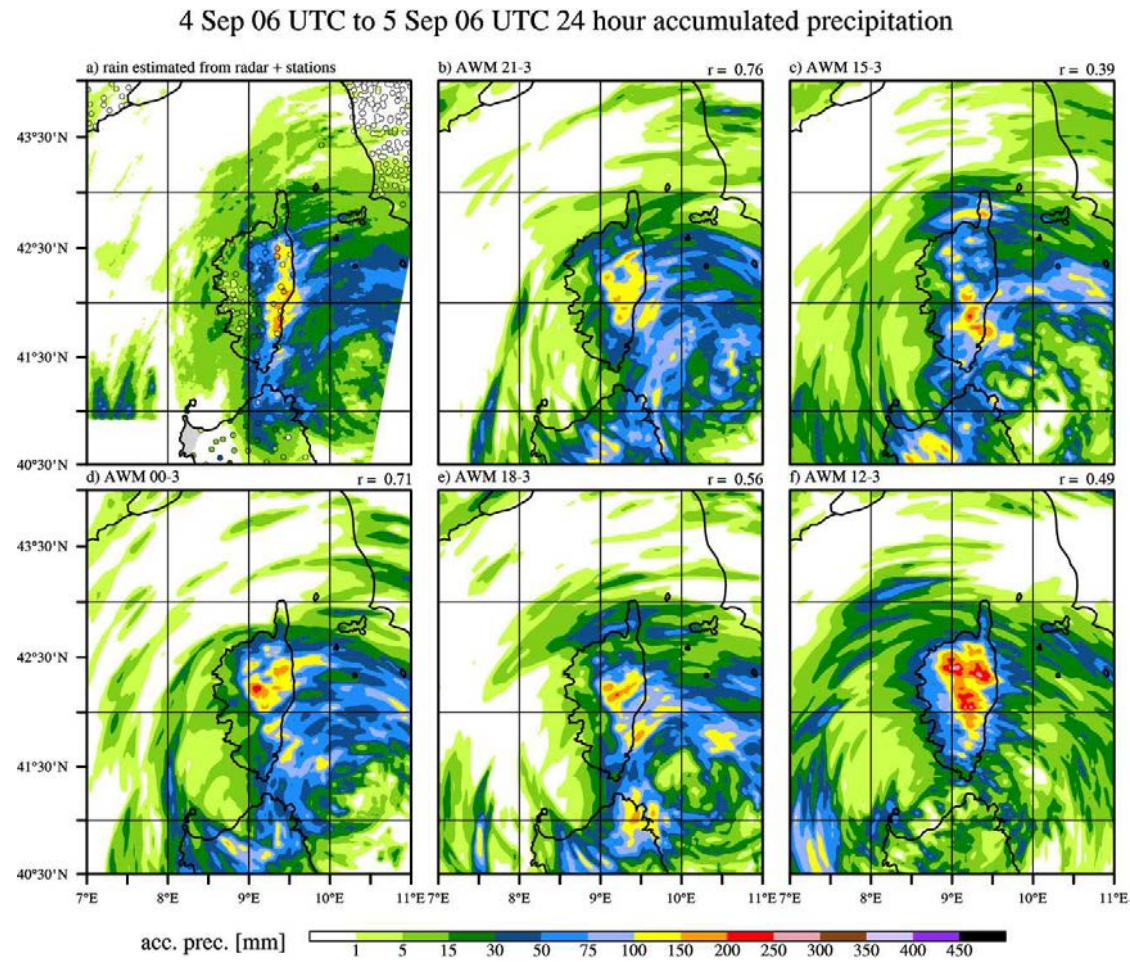


Figure 4.4: Observed (a, like Fig. 4.3f) and simulated precipitation for the AW-members of the initial condition ensemble (b-f). Pearson's product-moment coefficient r is shown for each simulation. The calculation of r is limited to the rain gauges on Corsica.

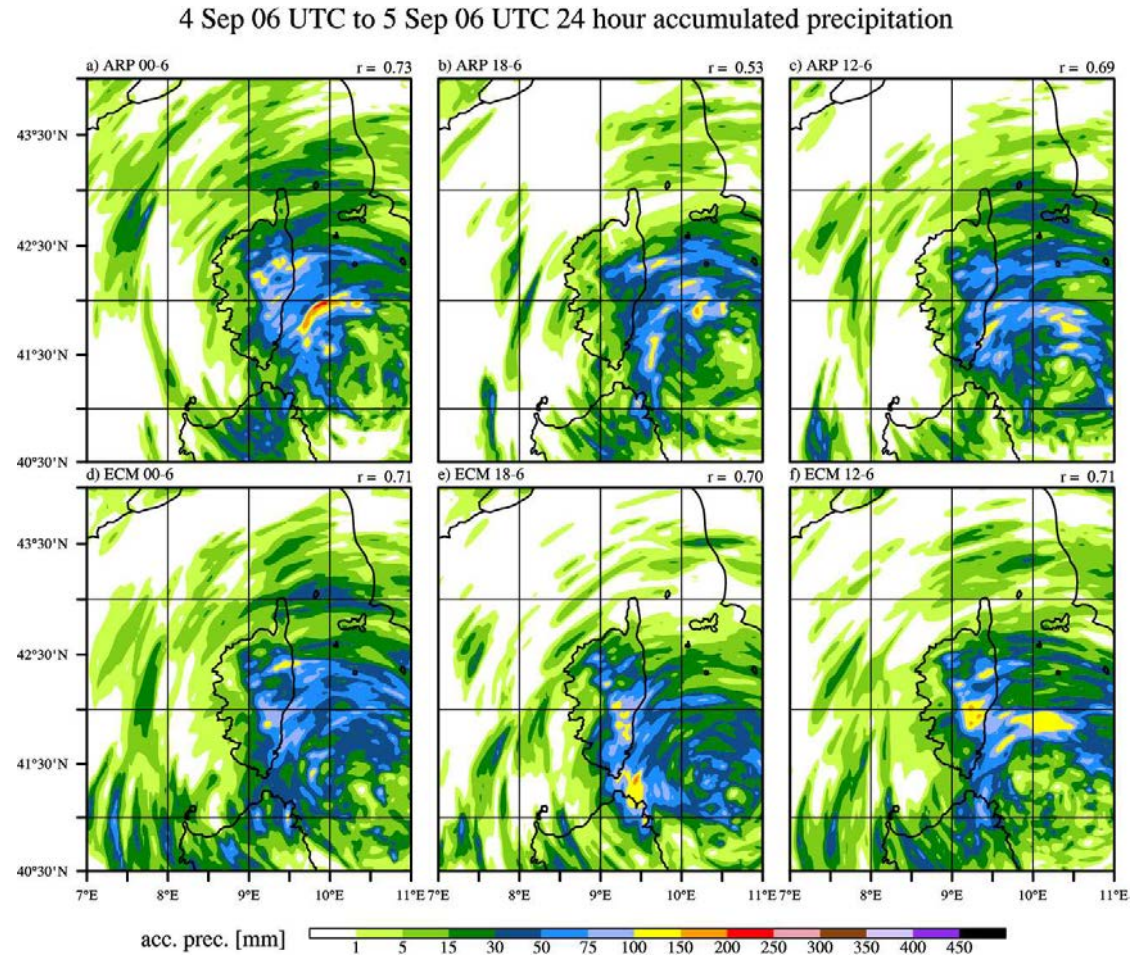


Figure 4.5: Like Fig. 4.4b-f, but for the **AR** and **EC**-members of the initial condition ensemble.

4.3.2 Quantitative Precipitation Verification

To get a quantitative measure of the precipitation for the ensemble members, the temporal evolution of the average precipitation over Corsica is shown in Fig. 4.6. The radar and model data are interpolated to the rain-gauge locations and the average of the accumulated precipitation is shown (Fig. 4.6a). The rain-gauges registered an average of 59 mm between 4 September 00 UTC and 5 September 06 UTC. The radar estimated precipitation is about 22% lower at 46 mm. The accumulated values for the simulations vary between 25 (**AR 18-6**) and 108 mm (**AW 12-3**), which equals 42 and 183% of the rain-gauge values, respectively. All but two of the ensemble members are grouped within 60 to 120% of the station values. The accumulated precipitation (Fig. 4.6a) confirms that the **AW** members produce the highest precipitation. The five **AW** simulations are the five simulations with the highest precipitation. Three of them, namely **AW 00-3**, **21-3**, and **18-3** are within 5% of the observed values. However, they produce too much precipitation during the last 6 to 8 hours of the event. The **EC** members show a high consistency, spreading less than 2 mm. However, they underestimate precipitation by around 30%. The **AR** members show a higher spread and the lowest precipitation.

The precipitation rate (Fig. 4.6b) shows that precipitation was observed and simulated during the entire comparison period of 30 hours. Station values remained approximately between 1 and 4 mm h⁻¹ during the entire period with the radar values almost constantly underestimating precipitation. The peaks in the precipitation rate are poorly detected by the radar and their timing is not reproduced by the initial condition ensemble. Overall, the temporal evolution of the precipitation contains little useful information concerning the details of each simulation. The peaks appear to be mostly related to convection embedded within the cyclone. Such details are usually highly variable within ensembles even if the

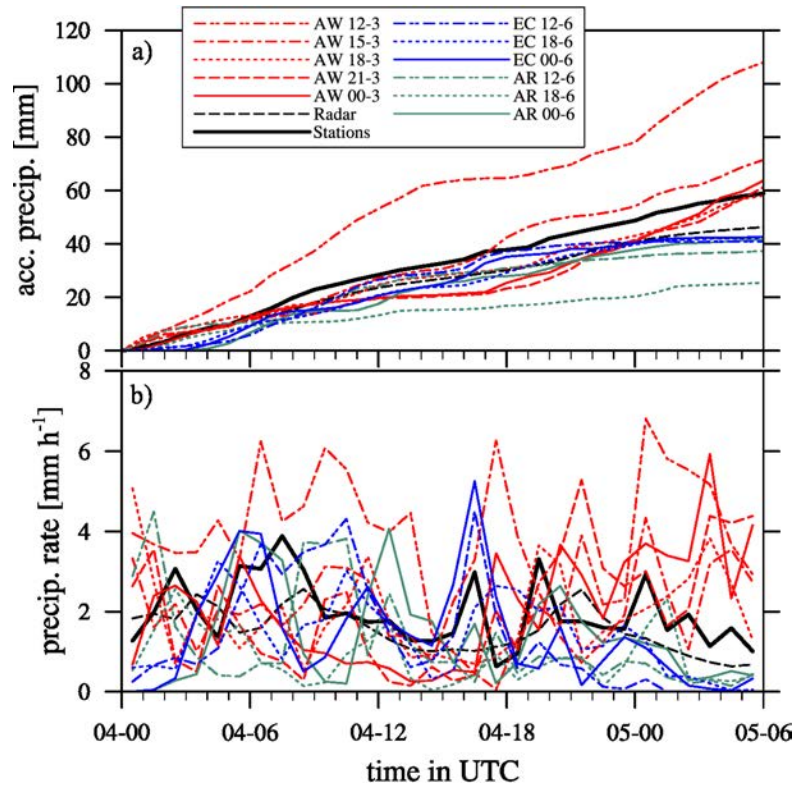


Figure 4.6: Average accumulated precipitation (a) and precipitation rate (b) over Corsica, data obtained from 26 hourly reporting surface stations with radar and model data interpolated to the observation points.

members show little spread. The few occurrences where peaks of observed and simulated precipitation line up (e.g. 4 September 16 UTC, **EC 00-6** and **12-6**) must not be over-interpreted, especially when considering that Fig. 4.6 contains no information on the spatial distribution. This means that a well timed peak can be simulated in a different location than where it was observed.

Figure 4.7 shows two Taylor diagrams for the HPE of 4 September for the entire domain (a) and for the stations on Corsica (b). When taking all stations into account the spread between the ensemble members is larger than when limiting calculation to Corsica. This is due to high precipitation over the Apennines where the different ensemble members yield highly varying results. These areas have a

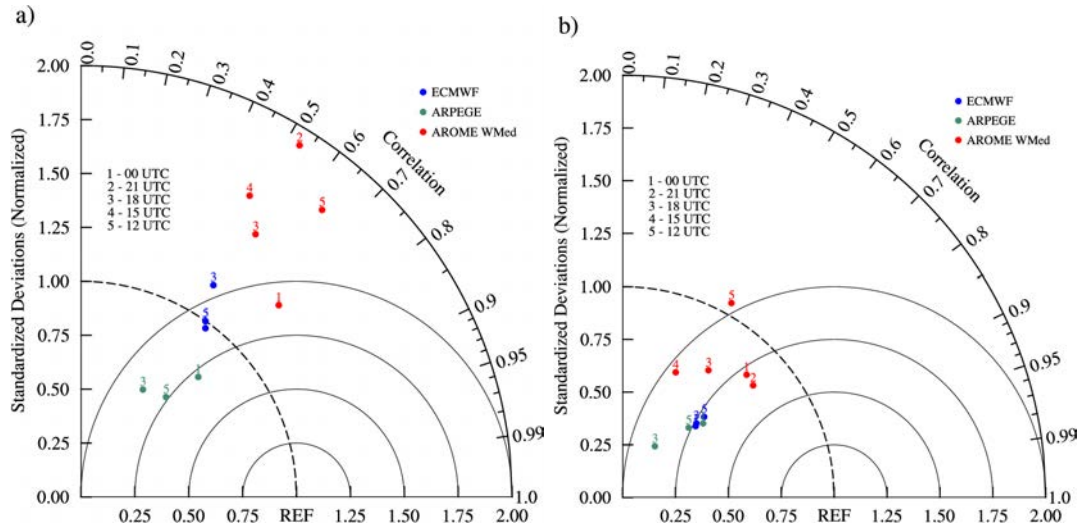


Figure 4.7: Taylor diagrams of the initial condition ensemble for 4 September 2012. The diagrams are based on the 06 to 06 UTC accumulated precipitation showing the results for the entire domain (a) and only the stations on Corsica (b).

relatively large impact on the statistics due to their dense observational network while they are relatively close to the lateral domain border. Figure 4.7a shows a clustering of the ensemble members depending on the model which was used for the initial and boundary conditions. The members initiated from ARPEGE data show the lowest normalized standard deviations while the simulations based on AROME WMed show the highest one. The normalized RMSE is lower for ARPEGE members and highest for AROME WMed members. In terms of correlation the three groups are relatively similar, and r is between 0.50 and 0.72.

When limiting the comparison to Corsica (Fig. 4.7b), the spread is lower due to less variation in the standardized deviation, even though r now varies more strongly, between 0.39 and 0.76. The clustering by input model remains visible. **AW** simulations show higher normalized standard deviation but a similar correlation and RMSE as the **AR** and **EC** members. Interestingly, the best simulation over Corsica, **AW 21-3** in Fig. 4.7b performs much worse for the entire domain.

AR 00-6 performs well for the entire domain as well as Corsica. The **EC** members perform significantly better over Corsica than over the entire domain.

Table 4.1 helps to quantify the performance of the individual ensemble members in more detail. It shows MAE , NB , and r (see Sect. 3.2.1) for the initial condition ensemble. The statistics are shown for the entire domain and for Corsica only. It mostly confirms what is seen in the Taylor diagrams, but NB adds additional information, which is not visible in Taylor diagrams. The numerical bias indicates whether precipitation is over- or underestimated. Over the entire domain, NB varies between 0.76 and 2.14, showing large variation throughout the initial condition ensemble. Over Corsica, NB varies even more, ranging from 0.35 to 2.10. **AR 00-6**, which performs relatively well on the entire domain and over Corsica according to the Taylor diagrams, has a NB of 0.72, whereas **AW 21-3** is at 1.05, agreeing better with the observation. **AW 21-3** shows the highest r , second best NB and the second lowest MAE of all initial condition members over Corsica.

Based on a visual comparison and the statistics presented above, a shortlist of candidates for a reference simulation can be compiled. The Taylor diagram in Fig. 4.7a indicates **AR 00-6** as best simulation for the entire domain. However, the large spread seen in Fig. 4.7a arises mainly from differences in simulated precipitation in northern Italy, relatively close to the lateral boundary of the domain. In addition, the focus of this study puts emphasis on the precipitation on Corsica. Over the island (Fig. 4.7b) **AW 21-3** outperforms all other simulations. **AR 00-6** performs similarly well over Corsica as it does for the entire domain, but underestimates precipitation. The **EC** members show very little spread over Corsica and all perform similarly well as **AR 00-6**, but also underestimate precipitation. The **AW** members still show the largest spread of all input data sets, but **AW 21-3** is the best choice for this case and will therefore be used as reference simulation.

Exp. Name	all stations in domain			stations on Corsica		
	<i>MAE</i>	<i>NB</i>	<i>r</i>	<i>MAE</i>	<i>NB</i>	<i>r</i>
AWM 00-3	6.85	1.73	0.72	24.81	1.13	0.71
AWM 21-3	9.80	2.10	0.53	23.26	1.05	0.76
AWM 18-3	8.46	1.80	0.55	26.73	0.94	0.56
AWM 15-3	10.49	2.14	0.49	37.53	1.22	0.39
AWM-12-3	9.59	1.92	0.64	60.08	2.10	0.49
ARP 00-6	5.13	1.03	0.70	23.01	0.72	0.73
ARP 18-6	5.63	0.84	0.50	31.89	0.35	0.53
ARP 12-6	5.15	0.76	0.65	25.28	0.53	0.69
ECM 00-6	6.79	1.38	0.59	24.28	0.69	0.71
ECM 18-6	7.51	1.50	0.53	24.13	0.69	0.70
ECM 12-6	7.20	1.39	0.58	25.88	0.71	0.71

Table 4.1: Mean absolute error (*MAE*), normalized bias (*NB*), and Pearson’s product-moment coefficient *r* for the initial condition ensemble members and rain gauges for the 4 September 06 UTC to 5 September 6 UTC 24 hour accumulated precipitation.

4.4 Cyclone Tracks

While all members of the initial condition ensemble produce a slow moving cyclone located mostly southeast of Corsica, the placement of the center is different in the individual members. Figure 4.8 shows the location of the sea level pressure minimum from 4 September 01 UTC to 5 September 06 UTC for all ensemble members. At 06 UTC (diamonds) the cyclone centers are all located within about 100 km of each other, moving north, some with an eastern component. At 12 UTC (circles) the position varies by up to 200 km. The position of the cyclone center is important because it determines the exact wind direction relative to the orography of the island. North of the cyclone center the wind is roughly easterly while northeast of the center it is more northeasterly. The simulation with the highest precipitation on Corsica, **AW 12-3**, is also the only one which locates the cyclone center directly south of Corsica during more than half of the simulation

time (leftmost red track). **AW 15-3** is the second of two tracks which move over the two islands before 00 UTC of 5 September. Both, **AW 12-3** and **15-3** are the simulations with the highest simulated precipitation over Corsica.

Like for precipitation, the **AW** members show the largest variability in their tracks with the most distant members lying about 100 km apart from the beginning. In comparison, both the **AR** and the **EC** ensemble members are relatively closely grouped until 18 UTC (stars). The longitude of the 12 UTC and 18 UTC sea level pressure minimum is linked to the *NB*. Higher longitude of the cyclone center means a lower *NB*. The relation is not perfect, however, the cyclone center in the simulation with the highest precipitation (**AW 12-3**) is consistently farther west than in all other members whereas the cyclone center in the **AR** members, which produce the least precipitation, is further east than in all other members during the first 18 hours. This indicates that the cyclone position has an important impact on the precipitation amount on the island.

Between 18 and 00 UTC of 4 September, all ensemble members except for **AW 00-3** and **21-3** simulate a change in movement first toward south and then east or southeast, toward the Tyrrhenian sea. Consequently, the markers for 5 September 06 UTC (downward facing triangles) are mostly found east of northern Sardinia over the sea. The members which move out over the sea toward the end of the simulation (the **EC** and **AR** members) produce the lowest precipitation after 20 UTC of 4 September, whereas simulation with cyclone centers closer to the island produce higher values. In terms of sea level pressure, the cyclones were within less than 2 hPa and their core pressure varied by less than 3 hPa over the compared 30 hour period.

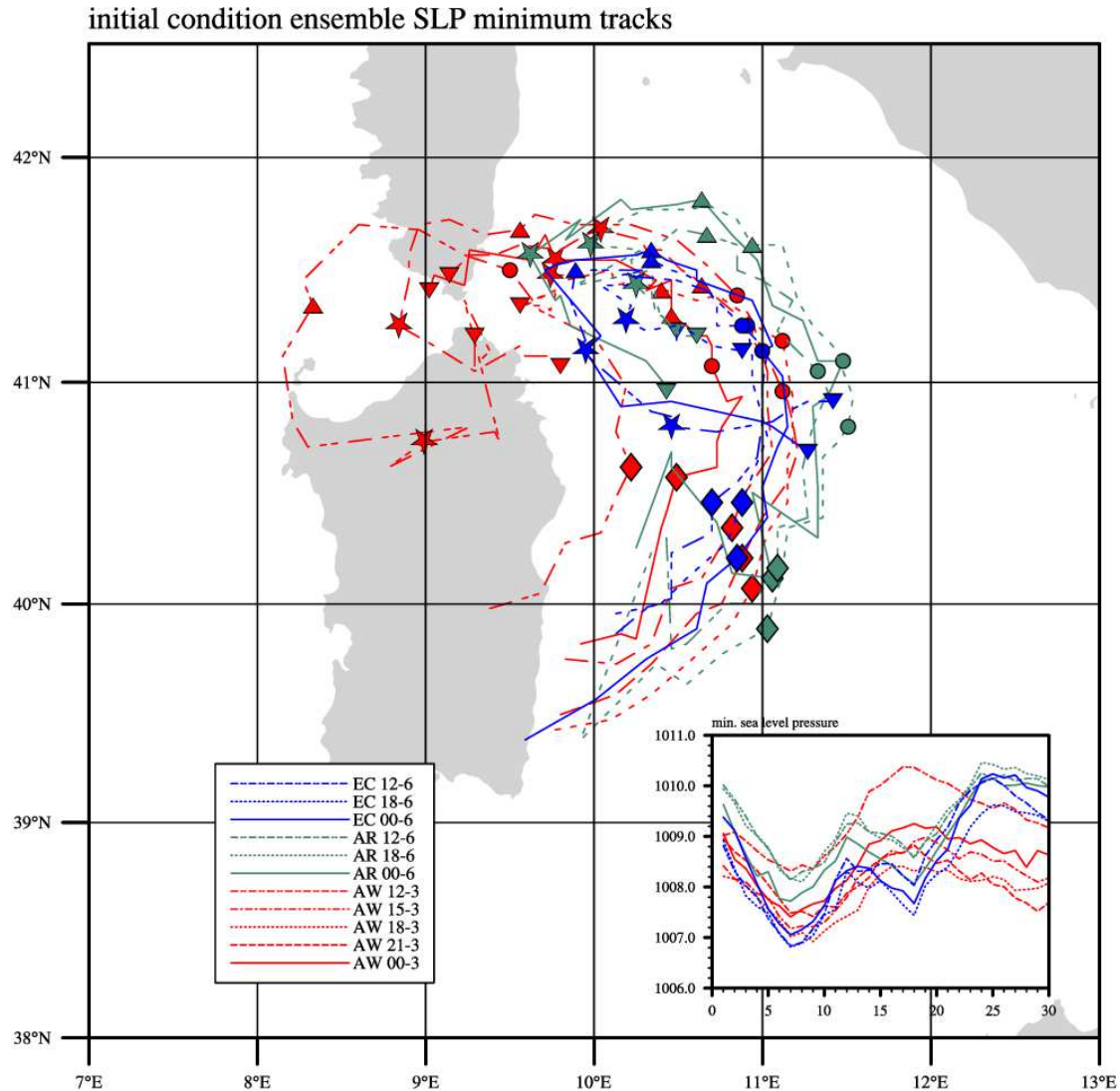


Figure 4.8: Tracks of the sea level pressure minimum obtained from smoothed fields of the initial condition ensemble. The position every 6 hours is shown by large markers with the steps in between indicated by small circular markers. The embedded figure shows the minimum sea level pressure for the smoothed fields for each simulation over time.

4.5 Evolution of the HPE in the Reference Simulation

The agreement with observations on an hourly basis is shown in Fig. 4.9, where **AW 21-3** is compared to observations for two representative times. The event began mostly over the southern half of Corsica's east coast and precipitation moved north during the day. This can be seen in the radar estimated precipitation shown in Figs. 4.9a and d for 10 and 20 UTC respectively. The simulation reproduces the precipitation field well with the heaviest precipitation located over the southern east coast and northeastern Sardinia at 10 UTC (Fig. 4.9b). However, the precipitation over the northern part of the island is not simulated and the precipitation over the coast ranges too far off shore. The simulation captures the second phase during which precipitation is most intense in the north. Figure 4.2e shows the simulated precipitation at 20 UTC with the bulk of the precipitation located along the northern coast. However, at 20 UTC the model places heavy precipitation too far east over the sea. In addition, a secondary maximum is visible further inland, west of the coast (around 9° east), which is less pronounced in the observations.

Figures 4.9c and f give an indication of the primary mechanism of the HPE. The cyclonic rotation is well visible southeast of Corsica in the 950 hPa wind with the easterly wind north of the cyclone encountering the orography of Corsica. The θ_e field shows how warm air from the Tyrrhenian sea is transported north along the east side of the cyclone. During the morning (Fig. 4.9c) high θ_e is mostly found around the cyclone core while lower values are found along the coast. The wind is oriented mostly along the orography, limiting orographic lifting. However, at 20 UTC the warm air has penetrated all the way up to the north of Corsica and the cyclone center is found further north. These two changes result in warmer air being advected along the east coast of Corsica with a larger wind component

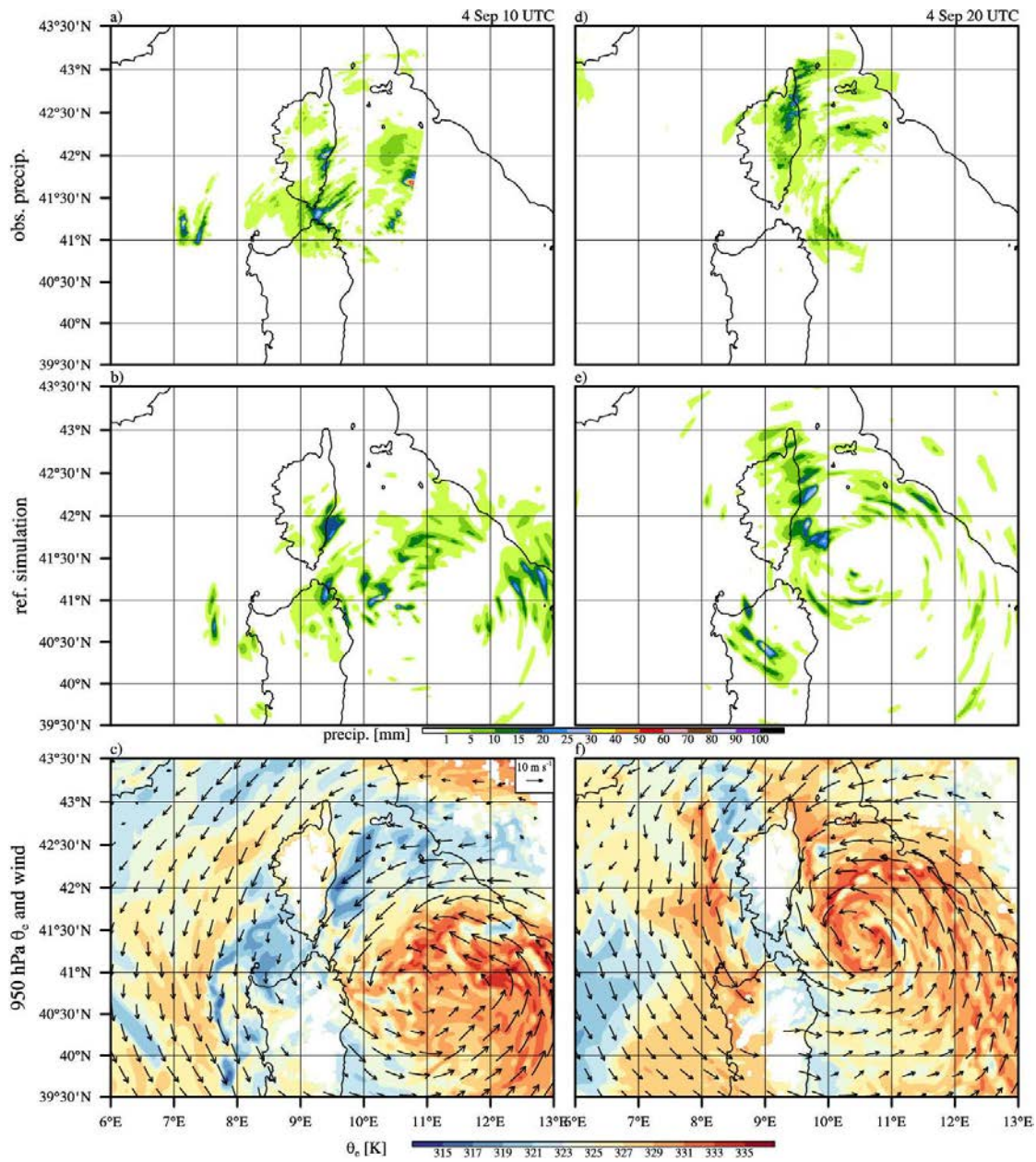


Figure 4.9: Observed (a, d) and simulated (b, e) 1 hour accumulated precipitation and 950 hPa θ_e and wind (c, f) shown for 10 and 20 UTC of 4 September at two representative phases of the HPE.

perpendicular to the orography along the northern half of the coast (Fig. 4.9). The panel also explains the precipitation over the northwest of Sardinia, which is the result of moist northwesterly flow toward the Sardinian coast.

In summary, the event of 4 Sep 2012 was caused by a quasi-stationary cyclone which forced the easterly flow of conditionally unstable air toward the Corsican orography. The observations confirm how the precipitation was concentrated along the east coast of the island. The chosen reference simulation, **AW 21-3**, reproduces the general precipitation distribution. However, the model has problems placing the precipitation along the coast. A large part of the precipitation is found further inland, just east of 9° east, close to the center of the island. The reason for this is not clear, but in cases of orographic forcing the placement of precipitation can depend heavily on the resolution and height of the terrain. Thus, in addition to the initial condition ensemble, high resolution simulations are presented in the next section.

4.6 Sensitivity to Horizontal Grid Spacing

The effect of smaller horizontal grid spacing is not only the resolution of smaller scale processes but also a more realistic topography. Within the 2.5 km simulation, a nest (Fig. 3.1) with a horizontal grid spacing of 500 m is placed over Corsica. Its configuration is identical with the reference simulation except for the deactivation of the shallow cumulus scheme and a change from 1D turbulence to 3D turbulence. The mixing length in both domains is calculated using the formulation of Bougeault and Lacarrère (1989).

In order to run a nested simulation, Meso-NH recalculates the terrain of Domain 1 to account for the higher orography in the nest. The model does this by adjusting the terrain in Domain 1 to the average of the terrain in Domain 2 for each grid

point. This has the effect of increasing the peak height and valley depth also in Domain 1. To test the influence of this change in orography, a second simulation at 2.5 km is conducted using only the new terrain of Domain 1 without placing the nest, allowing to observe the effect of the slightly modified orography on the reference simulation. This additional simulation is called **AW 21-3 oro** and its results are presented alongside the reference and the nested simulation in this section.

4.6.1 Impact on Precipitation Distribution

The precipitation distribution, including observations, is shown in Fig. 4.10. For comparison, the reference simulation is included in Fig. 4.10b. In comparison, the nested simulation (Fig. 4.10d) shows an eastward shift of the precipitation toward the coast over the northern half of Corsica. Over the southern half, most of the precipitation is seen off-coast, east of the island. This maximum over the sea is greatly increased compared to the reference simulation and the observations. The radar's view in this area is partly obstructed by orography, but the available data nevertheless indicates a significant overestimation of the off-coast precipitation. On the other hand, the spurious maximum in the center of Corsica (see Fig. 4.10b) is greatly reduced in the 500 m simulation. The values over northern Corsica around 9°east agree well with the observed values (75–100 mm) while values over 100 mm are mostly limited to the coastal mountain range over the sea of Corsica. South of 42°north, the maximum precipitation is found too far west in the reference simulation but too far east in the 500 m simulation and precipitation over the southeast of the island are underestimated in the 500 m simulation. Overall, the precipitation distribution over the island improves as the horizontal grid spacing decreases, as is reflected in the increase in correlation r from 0.76 in the reference simulation to 0.85 (0.84) in Domain 1 (2) of the nested simulation.

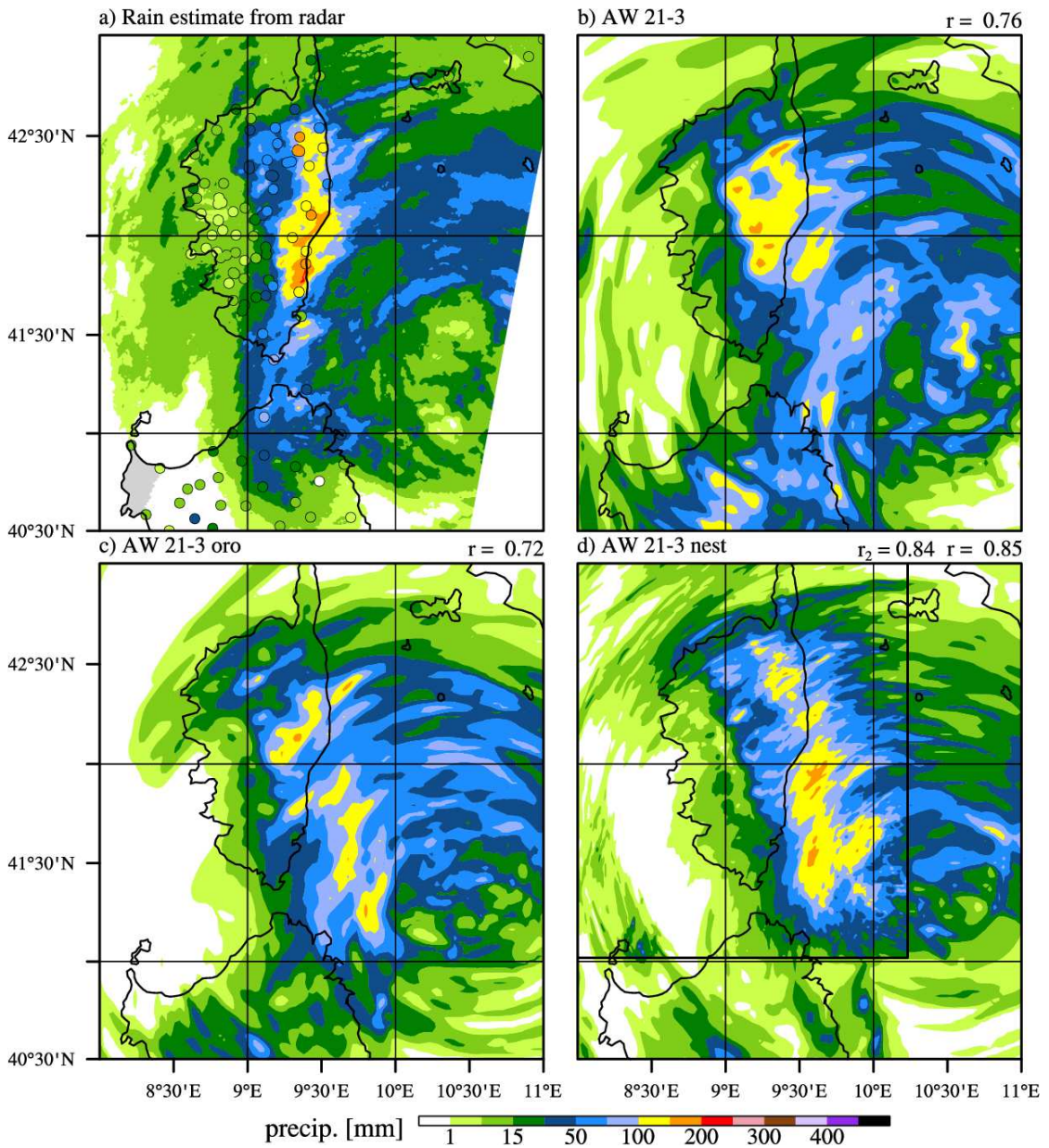


Figure 4.10: Observed (a) and simulated (b, c, d) 24 hour accumulated precipitation from 4 September 06 UTC to 5 September 06 UTC.

The displacement of the precipitation can be attributed to two likely effects. Firstly, orographic lifting is more effective as the height of the topography increases. Secondly, a higher horizontal resolution allows the formation of more narrow but stronger convergence lines. While orography only changes over land, increased convergence is also simulated over the sea. In **AW 21-3 oro**, only the orography is changed, eliminating the effect of stronger and narrower convergence lines. Nevertheless, precipitation over the sea changes noticeably (Fig. 4.10c). In particular, the precipitation off-shore east of southern Corsica is higher and the region with precipitation >100 mm are more widespread. This indicates an interaction between the island and the precipitation further upstream over the sea. Over the island itself, a similar effect as in the nested simulation is visible, albeit weaker. The spurious maximum in the center of the island is greatly reduced, but the simulation does not align the highest precipitation with the coast.

The correlations for the three simulations confirm that the 500 m simulation is better at representing the spatial distribution of precipitation. However, **AW 15-3 oro** shows a lower correlation than both the reference and the 500 m simulation, despite producing a result that visually appears to be between the other two. This demonstrates the limitations of a simple statistic measure like the Pearson product moment coefficient.

4.6.2 Convergence Zones

As mentioned above, altered orography can only directly impact the simulation over land. Over the sea, on the other hand, convergence is the main lifting mechanism. However, this does not exclude an indirect impact of changed orography on precipitation over the sea, for example through the formation of upstream convergence zones over the sea due to a change in flow regimes. The large discrepancies in off-shore precipitation distribution between **AW 21-3**, **AW 21-3 oro**, and **AW**

21-3 nest indicate an essential role of convergence in the HPE of 4 September. To explore this, the convergence of the 10 mAGL convergence is shown in red in Fig. 4.11, while divergence is shown in blue.

Figure 4.11 reveals that convergence in the reference simulation is found primarily inland, around 15-25 km from the east coast (west of 9.5° east, Fig. 4.11b). The orography of the island shows a visible imprint in the convergence field along the center of the island, just east of 9° . In addition, multiple convergence zones are visible over the sea east of the island, corresponding to convective cells embedded in the cyclone circulation.

In **AW 21-3 oro** (Fig. 4.11a), the strongest convergence zone is found directly over the northern half of the east coast of Corsica and, more importantly, off-coast parallel to the southern half of the east coast of the island. The increase of the topography height is enough to modify the precipitation from orographic to upstream along a convergence line, effectively displacing it eastward by around 50 km. Over the island itself, the orography has a stronger impact on the convergence field, as indicated by the darker shades of red and blue over the center of the island.

The 500 m nested simulation (Fig. 4.11c) shows more detail and higher convergence and divergence values. Smaller horizontal grid spacings allow higher convergence or divergence values, as they resolve the wind field better. While this prevents a direct comparison of the magnitude of convergence between the reference and the nested simulations, the figure still allows to locate convergence zones. In this case, Fig. 4.11c reveals that convergence is found along the northern half of the Corsican coast and off-shore almost parallel to the southern half of the islands east coast. Over the island itself, convergence and divergence align mostly with orographic features. However, **AW 21-3 nest** produces more convergence zones

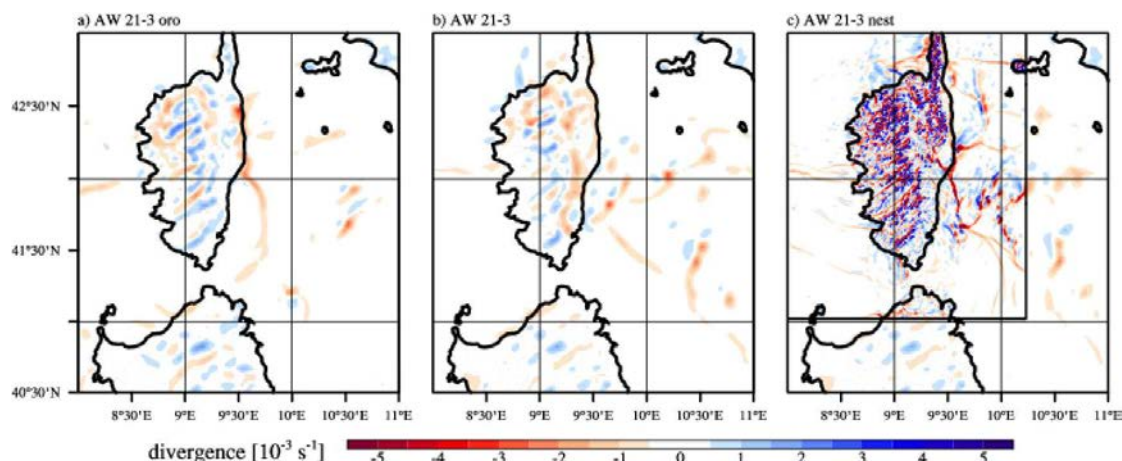


Figure 4.11: Convergence at 4 Sep 10 UTC during the first phase of the HPE for the modified orography (a), reference (b) and nested (c) simulation. The location of the nest is indicated by the black rectangle in (c).

over the sea east of Corsica, providing lift for the formation of more convective cells than in both, **AW 21-3** and **AW 21-3 oro**.

The above described differences are well visible at 10 UTC, but are seen throughout the entire duration of the HPE. The large maximum seen east of the Corsican coast in Fig. 4.10c and d are a direct result of this offshore convergence. The three simulations discussed above show that two mechanisms are responsible for the precipitation displacement in **AW 21-3 nest**. Firstly, higher orography changes the precipitation, instead of orographic lifting, lifting ahead of cold pools is the primary lifting mechanism. Secondly, the convergence ahead of the cold pools is more intense as horizontal grid spacing is reduced, allowing the formation of even more precipitation. Ultimately, in this case the height of the orography is responsible for placement of the precipitation. Higher orography moves the bulk of the precipitation further upstream, while a decrease in horizontal grid spacing allows the formation of stronger and more convergence zones, increasing the precipitation.

4.7. TEST OVER FLAT OROGRAPHY

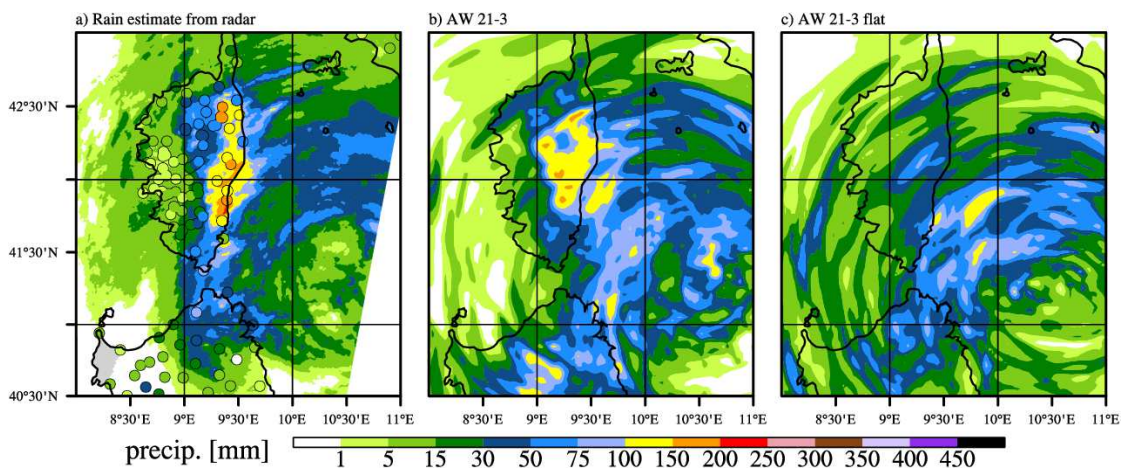


Figure 4.12: Observed (a) and simulated (b,c) precipitation for the reference (b) and flat (c) 24 hour accumulated precipitation from 4 September 06 UTC to 5 September 06 UTC.

4.7 Test over Flat Orography

An additional simulation, **AW 21-3 flat**, is conducted over flattened Corsican orography. The island itself is not removed and the land use data remains unchanged. This means that surface wind will still encounter increased friction as it moves from the sea over land, retaining a mechanism for the formation of convergence along the coast. However, the main obstacle is removed and the resulting simulation allows to examine the impact of the Corsican mountain ranges on precipitation distribution.

The resulting precipitation field is shown in Fig. 4.12, where the precipitation fields of the observations (a), the reference simulation (b) and the flat simulation (c) are shown side by side. The experiment shows that flattening orography greatly reduces precipitation over the island from >150 mm to mostly <75 mm or around 50%. While higher values remain over the eastern half of Corsica, the pattern itself shows no alignment with the orography, but the features of the field align mainly with the rotation of the cyclone. Interestingly, removing the Corsican orography

also reduces precipitation over Sardinia. In the reference simulation, moist air flows along the west of Corsica and encounters Sardinia as northwesterly wind around 22 UTC. In the flat simulation, this wind is replaced with a more stable northerly wind passing over the flat island before encountering Sardinia. The flat simulation confirms that the orography was a major factor for the placement of precipitation.

4.8 Conclusions

Of the three cases studied in this thesis, the HPE of 4 September 2012 is by far the most intense in terms of duration and precipitation intensity. It is also the most typical event, in that its synoptic situation and the location of the cyclone remain quasi-stationary throughout the duration of the event. As will be shown, this is not the case for either of the two events described below. The cyclone of 4 September exposed the coastal mountain ranges of eastern Corsica to warm moist cross-mountain wind, inducing orographic lifting and precipitation along most of the island's coast during more than 30 hours. Like the typical HPE described in Ricard et al. (2012) as well as in Chapter 2, the HPE of 4 September was fed by a large pool of warm and moist air located southeast of the island. This warm air was advected toward the island by the cyclone, where it encountered the high orography. In the analysis of Chapter 2, this case was placed in the autumn cluster.

The general evolution of the HPE is well reproduced at a horizontal grid spacing of 2.5 km. This is true for all members of the initial condition ensemble. However, closer examination reveals substantial difficulties in the precise placement of the precipitation. At a horizontal grid spacing of 2.5 km all simulations place an equal or higher amount of precipitation along the mountain ridge in the center of the island than they place over the coast. Most of the observed precipitation (including

4.8. CONCLUSIONS

all values >100 mm) was found along the coast and the values observed over central Corsica were generally below 100 mm. Despite this problem, the reference simulation **AR 21-3** was able to reproduce the south-to-north displacement of the heaviest precipitation throughout the event, which is evidence for the models capability of capturing the cyclone well.

The inland displacement of precipitation was removed when decreasing the horizontal grid spacing to 500 m, allowing the model to more accurately represent the interaction between the orography and the environmental wind. On the other hand, a simulation with a horizontal grid spacing of 2.5 km and an increased orography height was also able to partially offset the shortcomings of the initial condition ensemble members. However, its seemingly better performance was not confirmed by the calculated correlation values.

Chapter 5

Case 2: 31 October 2012 (IOP 18) - A Fast Moving Cyclone

This chapter presents the HPE of 31 October 2012 (HyMeX IOP 18). While this chapter is focused on Corsica, the event itself impacted a much larger area. During the early morning, precipitation was observed over the Balearic islands and the coast of continental France. Later during the day, heavy precipitation was observed along the entire Apennines from Liguria down to Calabria. Italy was hit later than Corsica, mostly during the afternoon of 31 October. On Corsica, a series of additional observations is available. A set of radiosoundings is available from San Giuliano and, in addition, X-band research radar was also deployed there. During the morning, a flight of the French ATR-42 gathered measurements over Corsica.

5.1 Synoptic Situation

The event of 31 October 2012 was characterized by a relatively fast moving cyclone which moved from the Balearic islands over the western Mediterranean past the

5.1. SYNOPTIC SITUATION

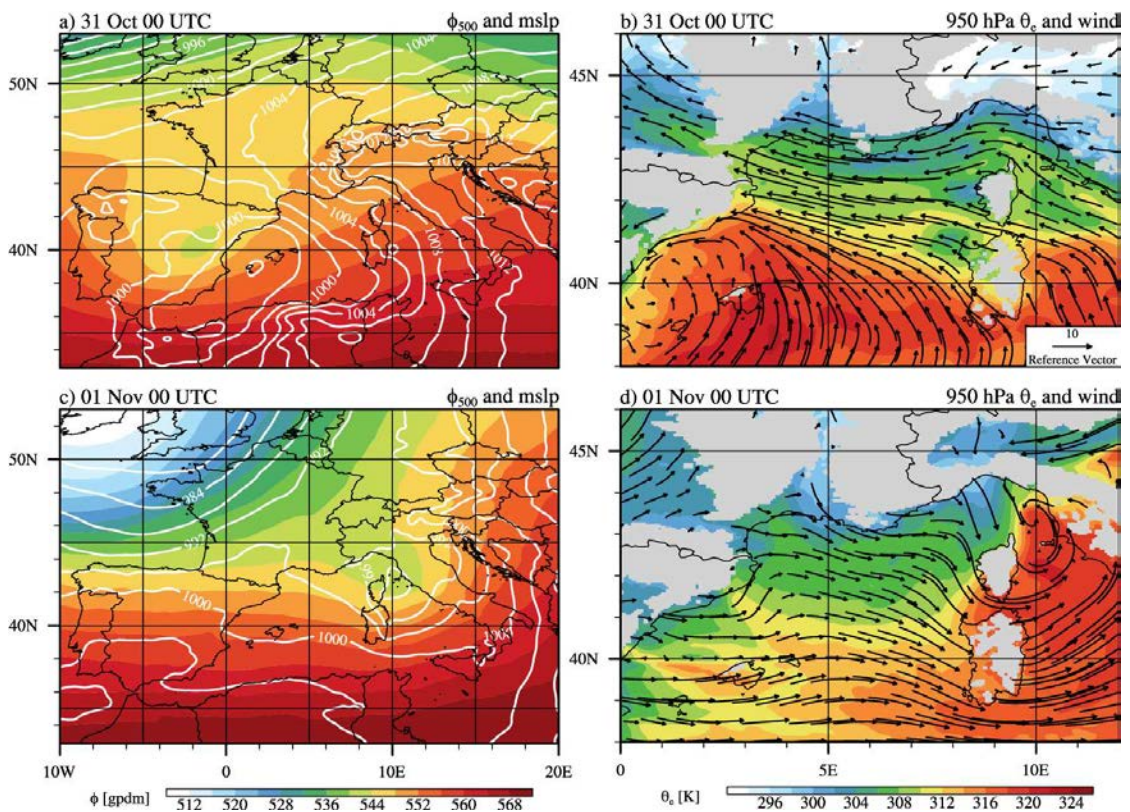


Figure 5.1: Synoptic Situation at 00 UTC of 31 October and 1 November over the western Mediterranean as seen in the ECMWF analysis. 500 hPa geopotential and sea level pressure (a, c) and 950 hPa θ_e and wind (b, d).

northern coast of Corsica close to the coast of Italy within only 24 hours. The 500 hPa field at 00 UTC of 31 October (Fig. 5.1a) shows a short wave trough over Spain embedded into a westerly upper level flow. Its surface signal (Fig. 5.1a) is found over Ibiza, the westernmost of the three largest Balearic islands. Within the boundary layer (Fig. 5.1b) a warm air mass lay over the southern part of the western Mediterranean. Within the warm air the wind was southerly to southeasterly, carrying moisture toward the north. Along the coast of continental France and northwestern Italy, easterly wind dominated. The cyclonic circulation can be seen in the southwest, off the coast of Spain (Fig. 5.1b). It lies about 100 km northeast of the MSLP minimum in the ECMWF analysis. The warm air

east of Sardinia over the Tyrrhenian sea was important for the early phase of the HPE. The southeasterly wind advected it toward the Corsican east coast, where it encountered the island's orography.

By 00 UTC of 1 November, 24 hours later, the shortwave trough had caught up to the surface low and lay directly over Corsica and its closed 500 hPa geopotential minimum had disappeared and the system was weakening rapidly (Fig. 5.1c). West of the short wave trough, a strong north-south gradient is visible in the 500 hPa geopotential field, indicating strong westerly flow at this level. Over the British isles a large trough is visible. The westerly flow along its southern edge was responsible for the fast movement of the cyclone. In the boundary layer, the flow over the western Mediterranean was mostly westerly and the region southwest of Sardinia and Corsica had cooled as the system passed. East of the islands, however, warm air now extended north beyond Cap Corse almost to the Ligurian coast (Fig. 5.1d). The MSLP minimum (Fig. 5.1c) and the center of rotation in the wind field (Fig. 5.1d) were at the same location, northeast of Corsica just off the Italian coast. The wind over Corsica was northwesterly (over the north) to westerly (over the south), during 31 October it turned by around 180°.

The changing conditions illustrate one of the constraints of the climatology in Chapter 2, namely the assumption of stationarity. Within 24 hours, the low level flow over Corsica changed from southeast to northwest, effectively causing the event to resemble the autumn cluster in the morning of 31 October and the mixed cluster in the morning of 1 November.

5.2 Observed Evolution

5.2.1 Satellite Images

This rapid change is also found in the satellite imagery of T_b for the HPE of 31 October. During the night (Fig. 5.2a) the entire western Mediterranean is covered in clouds with scattered cold cloud tops found from northern Africa all the way up to continental France and central Italy, indicating widespread, deep clouds. The situation at 06 UTC (Fig. 5.2b) is more organized with the highest clouds concentrated over southern France and the sea between Corsica and the French coast. In addition, lower values of T_b are found at 06 UTC, indicating increasingly active convection. The center of the cyclone becomes visible at 12 UTC (Fig. 5.2c) over Menorca and convection organizes north and northeast of the cyclone with fewer scattered cells to its east, over the Tyrrhenian sea and also over Italy. Convection continues to intensify and the lowest values of T_b are found around 18 UTC (Fig. 5.2d) around the border between France and Italy. By this time, the sky over Corsica is partly clear and the island lies just east of the cyclone center. As the cyclone continues northeast, it moves over the northern coast of the island and on toward Italy with convective activity rapidly decreasing over the Sea (Figs. 5.2e and f). The observed brightness temperatures confirm the rapid movement of the cyclone and the varying conditions over Corsica throughout 31 October. The sequence of satellite images indicates that convection hit the Island at some time between 06 and 12 UTC.

5.2.2 Observed Precipitation

On 31 October the highest precipitation was observed over the eastern half of Corsica, however, the entire island was affected by the precipitation. The different phases of the HPE are apparent when looking at consecutive plots of 6 hour accu-

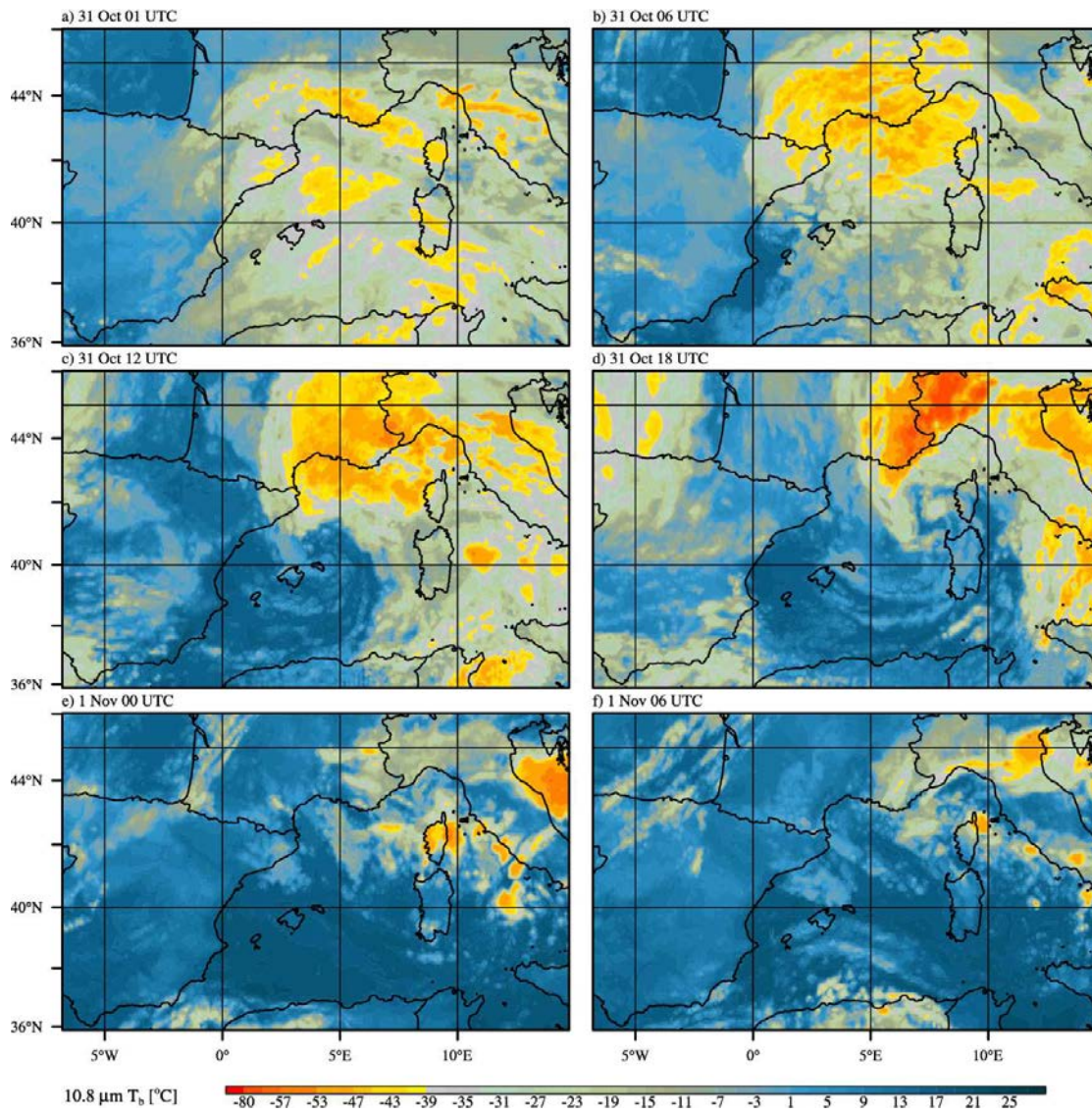


Figure 5.2: $10.8 \mu\text{m}$ brightness temperature [$^{\circ}\text{C}$] every 6 hours from 31 October 00 UTC to 1 November 06 UTC.

5.2. OBSERVED EVOLUTION

mulated precipitation (Fig. 5.3). The HPE began over the east coast of the island with moderate precipitation (around 15 to 25 mm over 6 hours, Fig. 5.3a). As indicated by the satellite observations, the most intense phase occurred between 06 and 12 UTC, with the bulk of the precipitation found over the orography along the northern half of the island's east coast (Fig. 5.3b). As the cyclone approached, the southeasterly flow over Corsica turned gradually south, and precipitation became increasingly stratiform, more widespread, and less intense (Fig. 5.3c). While the wind direction is not directly shown in the panels, it can be inferred from the traces of small scale precipitation structures, which are organized mostly north-south. As the cyclone moved over the northern coast of Corsica, precipitation weakened further (Fig. 5.3d). At this time, the rain field indicates rotation centered just northwest of Corsica. Precipitation stopped before 1 Nov 00 UTC (Fig. 5.3e).

The 24 hour accumulated precipitation between 31 Oct 06 UTC and 1 Nov 06 UTC is shown in Fig. 5.3f. While the radar derived values clearly show more precipitation over the east of the island, mainly over higher orography, the rain gauges indicate values above 25 mm also over the west of the island. This discrepancy is caused by the islands mountain range obstructing the radar at lower elevations over the west of Corsica. Compared to the case of 4 September, this discrepancy is stronger for 31 October, because more of the precipitation is formed in lower clouds instead of convective cells, such that a larger part of precipitation is obstructed by orography or distance. While the rain gauges and the radar both place the highest precipitation over the mountains, their values do not agree perfectly. The radar maximum appears slightly east of the maximum shown by the rain gauges and the highest values (two observation points >100 mm) are not confirmed by the radar. Considering the differences between the two modes of observation, the rain gauges

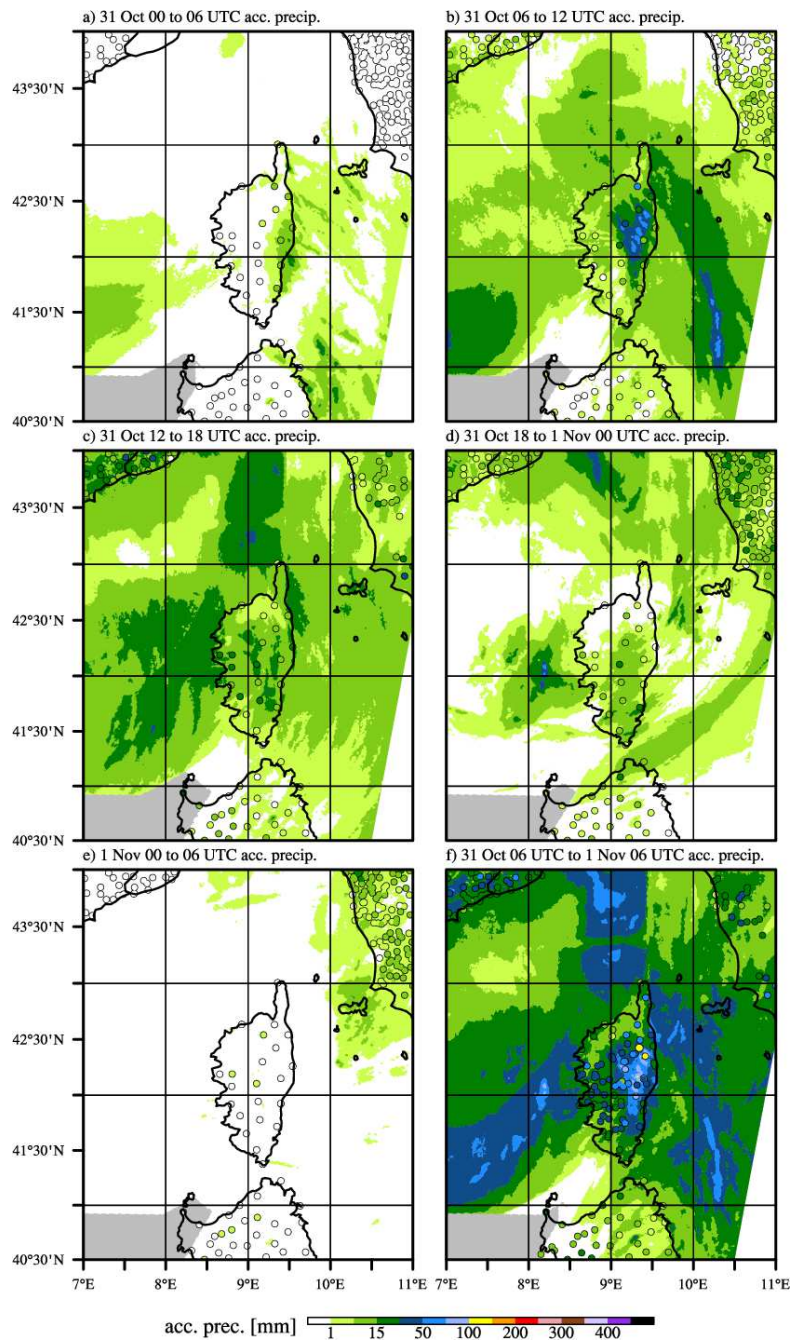


Figure 5.3: Observed rain over Corsica for the event of 31 October. Panels a to e show 6 hour accumulated rain for the 6 hour periods from 31 October 00 UTC to 1 November 06 UTC. The 31 October 06 UTC to 1 November 06 UTC accumulated rain is shown in f. The contours show the precipitation estimated from 5 minute radar data. Rain gauges are shown as filled circles.

take precedence over the radar derived values for the verification of simulations for this case.

The X-band radar, deployed in San Giuliano, mainly captured the event over the east coast. Like the operational radar in Aléria, it suffers from terrain shading over the west of the island. However, its measurements (not shown) confirm that the zones of high reflectivity reached higher in the morning (≈ 8 km) compared to later phases (after 18 UTC, mostly below 6 km and horizontally more homogeneous). As already indicated by the satellite images, the convective cells on 31 October 2012 remained less developed than for the previous case (4 September 2012) due to lower temperatures and lower instability in the upstream region of the HPE.

5.3 Initial Condition Ensemble

5.3.1 Spatial Distribution of 24 Hour Accumulated Precipitation

The 24 hour accumulated precipitation from 31 Oct 06 UTC to 1 Nov 06 UTC for all members of the initial condition ensemble is shown in Figs. 5.4 and 5.5. All simulation produce a large precipitation maximum between 8 and 9° east, which is located at the convergence line between northerly flow over the mountains around Genoa and southeasterly flow of warm air between Italy and Corsica. Compared to the radar observed values, all simulations appear to overestimate this precipitation maximum. However, the radar values for 31 Oct were shown to be of limited reliability in the above section. Moreover, this zone of high precipitation north of Corsica is relatively far from both radars (Aléria and Collobrières), such that an underestimation is likely. Another common feature to most simulations is the

concentration of precipitation over the orography of the island with lower values along the coasts. A precipitation maximum with varying intensity is also simulated over Cap Corse in all members. The large precipitation area over the sea west of Corsica, visible in Fig. 5.4a) is poorly reproduced by all members of the initial condition ensemble.

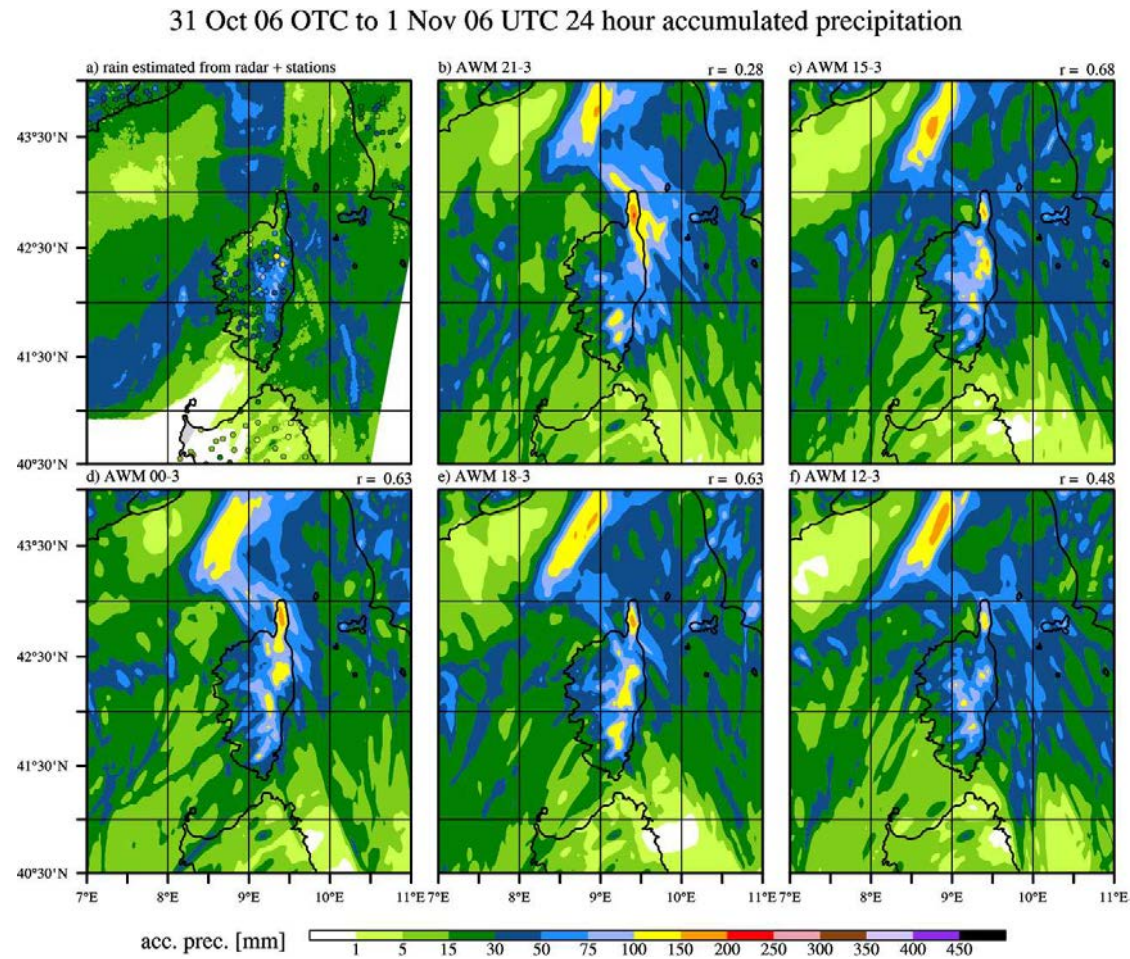
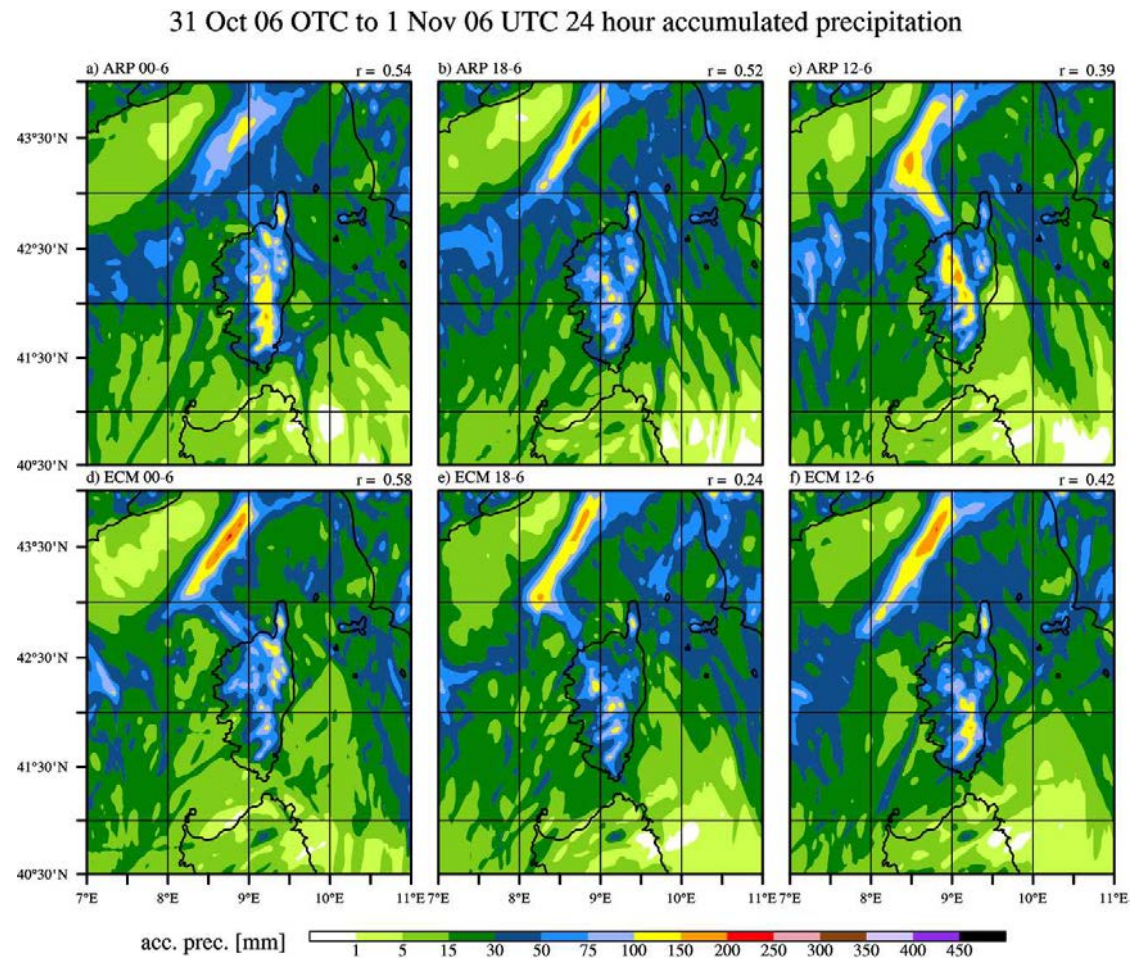


Figure 5.4: Observed (a, like Fig. 5.3f) and simulated precipitation for the AW-members of the initial condition ensemble (b-f). Pearson's product-moment coefficient r is shown for each simulation. The calculation of r is limited to the rain gauges on Corsica.

Figure 5.5: Like Fig. 5.4b-f, but for the **AR** and **EC**-members of the initial condition ensemble.

A more detailed look at the individual members reveals subtle differences in the placement of the precipitation maximum over the Corsican orography. For instance, **AW 00-3** (Fig. 5.4d) places most zones with more than 100 mm north of 42° north, while values above 100 mm (and even a small maximum with over 150 mm) are found further south in **AW 18-3** (Fig. 5.4e). However, the overall distribution is too similar to visually determine quality differences between the simulations. Compared to the observations (shown in Fig. 5.4a), all **AW** simulations overestimate the precipitation over Cap Corse in the north of the island. **AW 00-3**, **15-3**, and **18-3** reproduce the maximum around 42.5° north more accurately than the other two **AW** members, which place precipitation either too far north and south (**AW 21-3**, Fig. 5.4b) or underestimate the maximum over the coastal mountain range and place too much precipitation inland around 9° east (**AW 12-3**, Fig. 5.4f). The correlation r , shown above the respective panels, is highest for **AW 15-3** (Fig. 5.4c). However, all **AW** members fail to reproduce the extended zone of >30 mm which extends all the way from the center of the island to its west coast.

The ensemble members based on ARPEGE (Fig. 5.5a, b, c) and ECMWF (Fig. 5.5d, e, f) all have difficulties reproducing the precipitation maximum over the coastal mountain range in the east of Corsica. In all of the **AR** and **EC** simulations, the highest precipitation extends too far west whereas values along the west and east coast are underestimated compared to the station observations in Fig. 5.5a. In summary, the simulations of the initial condition ensemble perform similarly and visual comparison alone is insufficient to identify the best performing simulation. However, **AW 15-3** appears slightly superior, an impression which is confirmed by the correlation coefficient. However, further comparison is necessary for a definitive answer.

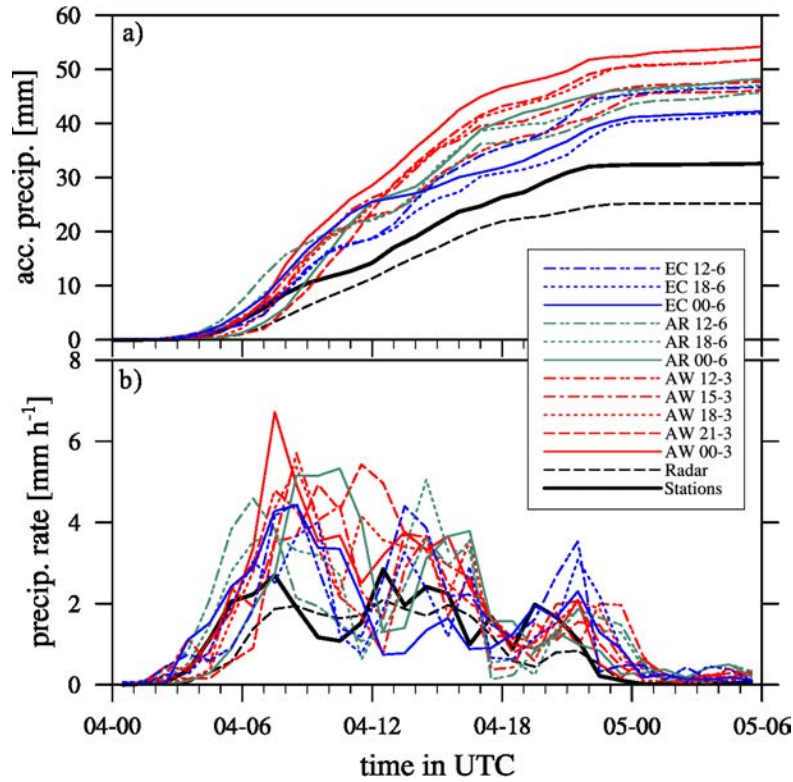


Figure 5.6: Average accumulated precipitation (a) and precipitation rate (b) over Corsica, data obtained from 26 hourly reporting surface stations with radar and model data interpolated to the observation points.

5.4 Quantitative Precipitation Verification

In addition to the spatial distribution presented above, the temporal evolution of precipitation over Corsica is examined (Fig. 5.6). All values are interpolated to observation points for better comparability. This comparison confirms that the radar derived values underestimate precipitation by around 20%. All simulations overestimate precipitation between around 30 to 60%. Moreover, the reproduction of the pattern, as quantified by r , does not coincide with the best quantitative estimation. The simulation with the best agreement of average precipitation (**EC 18-6**) is at the same time the one with the lowest correlation ($r=0.24$), underlining the difficulties in choosing a reference simulation for the case of 31 Oct 2012.

5.4. QUANTITATIVE PRECIPITATION VERIFICATION

The precipitation rate over Corsica (Fig. 5.6b) reveals an overestimation of the first precipitation peak mostly between 5 and 10 UTC by all simulations, between about 10 and 250% depending on the time and simulation. A second peak was observed from 12 to 16 UTC, which was also overestimated. The third and last peak around 19 to 21 UTC was better captured in terms of intensity but most simulations delay it by one to three hours. While neither the precise timing nor intensity is captured by any of the ensemble members, several simulations produce an event with a duration close to the observed one and also produce three distinct peaks in the precipitation rate. The **EC** simulations produce the least intense first peak but simulate the consecutive peaks with similar intensity whereas both **AW** and **AR** produce most precipitation (and thus overestimation) before 31 Oct 12 UTC while capturing the intensity - but not the timing - of the last peak between 19 and 23 UTC fairly well. However, Fig. 5.6 shows a large variability of the model performance over time in terms of intensity and does not allow definitive statements about the quality of the simulations.

More detailed information is available in Tab. 5.1, where the *MAE*, *NB*, and *r* are shown for all members of the initial condition ensemble. When comparing observed and simulated precipitation for the entire domain (first three columns), *r* is between 0.75 and 0.82, with the *NB* between 1.00 and 1.31, indicating a tendency to overestimation for all ensemble members over the entire domain. The *MAE* is similar for all members, ranging from 5.77 to 7.55 mm. The values over Corsica show a larger spread. Since the focus of this study is Corsica, the statistics over Corsica are more important in this case. Correlation varies between 0.24 and 0.68, indicating a large performance gap in terms of spatial precipitation distribution. The numerical bias *NB* confirms the overestimation with values between 1.08 and 1.33. Values for the *MAE* are higher over Corsica because the values for the entire

Exp. Name	all stations in domain			stations on Corsica		
	<i>MAE</i>	<i>NB</i>	<i>r</i>	<i>MAE</i>	<i>NB</i>	<i>r</i>
AWM 00-3	6.02	1.18	0.80	18.45	1.30	0.63
AWM 21-3	6.00	1.09	0.79	23.04	1.15	0.28
AWM 18-3	5.85	1.16	0.81	18.64	1.33	0.63
AWM 15-3	7.33	1.26	0.78	16.59	1.21	0.68
AWM-12-3	7.55	1.25	0.75	17.35	1.09	0.48
ARP 00-6	5.77	1.00	0.80	19.80	1.28	0.54
ARP 18-6	6.05	1.18	0.81	19.21	1.25	0.52
ARP 12-6	6.05	1.12	0.79	22.29	1.26	0.39
ECM 00-6	6.27	1.27	0.82	16.84	1.08	0.58
ECM 18-6	6.91	1.31	0.79	19.85	1.08	0.24
ECM 12-6	6.30	1.20	0.81	19.02	1.16	0.42

Table 5.1: Mean absolute error (*MAE*), normalized bias (*NB*), and Pearson’s product-moment coefficient *r* for the initial condition ensemble members and rain gauges for the 31 October 06 UTC to 1 November 6 UTC 24 hour accumulated precipitation.

domain are lowered by a large number of stations with zero observed and simulated precipitation outside the region affected by the HPE.

The Taylor diagrams in Fig. 5.7 visualize the information from Tab. 5.1. For the entire domain (Fig. 5.7a) the ensemble shows little spread, again due to the large number of stations unaffected by the HPE. Over Corsica, however, the quality differences between the ensemble members become clearly visible with **AW 15-3** showing the overall best performance over the island (red dot marked with 4). In addition, **AW 15-3** is one of the simulations which capture the three peak structure of the HPE, further increasing confidence in its performance. For the following tests and explanations, **AW 15-3** is chosen as reference simulation and additional tests will be based on this simulation.

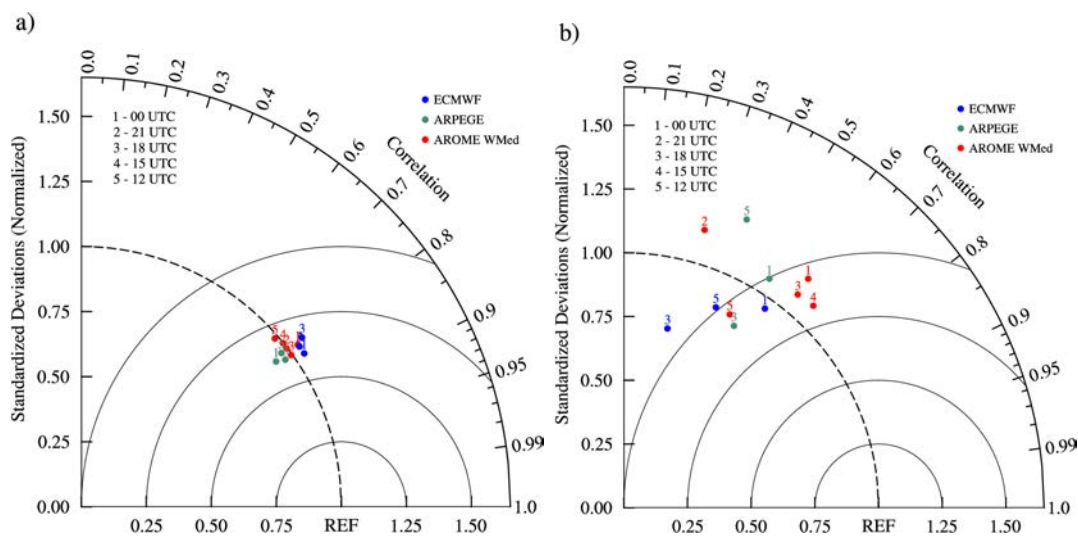


Figure 5.7: Taylor diagrams of the initial condition ensemble for 31 October 2012. The diagrams are based on the 06 to 06 UTC accumulated precipitation showing the results for the entire domain (a) and only the stations on Corsica (b).

5.5 Cyclone Tracks

The cyclone tracks as simulated by the initial condition ensemble are shown in Fig. 5.8. The plot is limited between 31 Oct 06 UTC and 1 Nov 00 UTC. Earlier and later cyclone positions vary greatly or even fall on the lateral boundary of the simulation domain. The low pressure system responsible for the HPE of 31 October was initially located north of the Balearic islands (diamonds in Fig. 5.8). The movement was relatively slow at first at around $10\text{--}20\text{ km h}^{-1}$. After 12 UTC (circular markers), the cyclone accelerated eastward, reaching Corsica between 20 and 22 UTC, depending on the ensemble member. Between 18 and 00 UTC, the MSLP cyclone center was moving at about $35\text{--}50\text{ km h}^{-1}$. In total, the cyclone center travels around 600 km in 18 hours.

Initially, the cyclone centers are widely spread and even at 06 UTC (diamonds). As the cyclone travels east, the tracks converge and all move within around 80 km from each other at 18 UTC (see triangles in Fig. 5.8). The tracks remain close

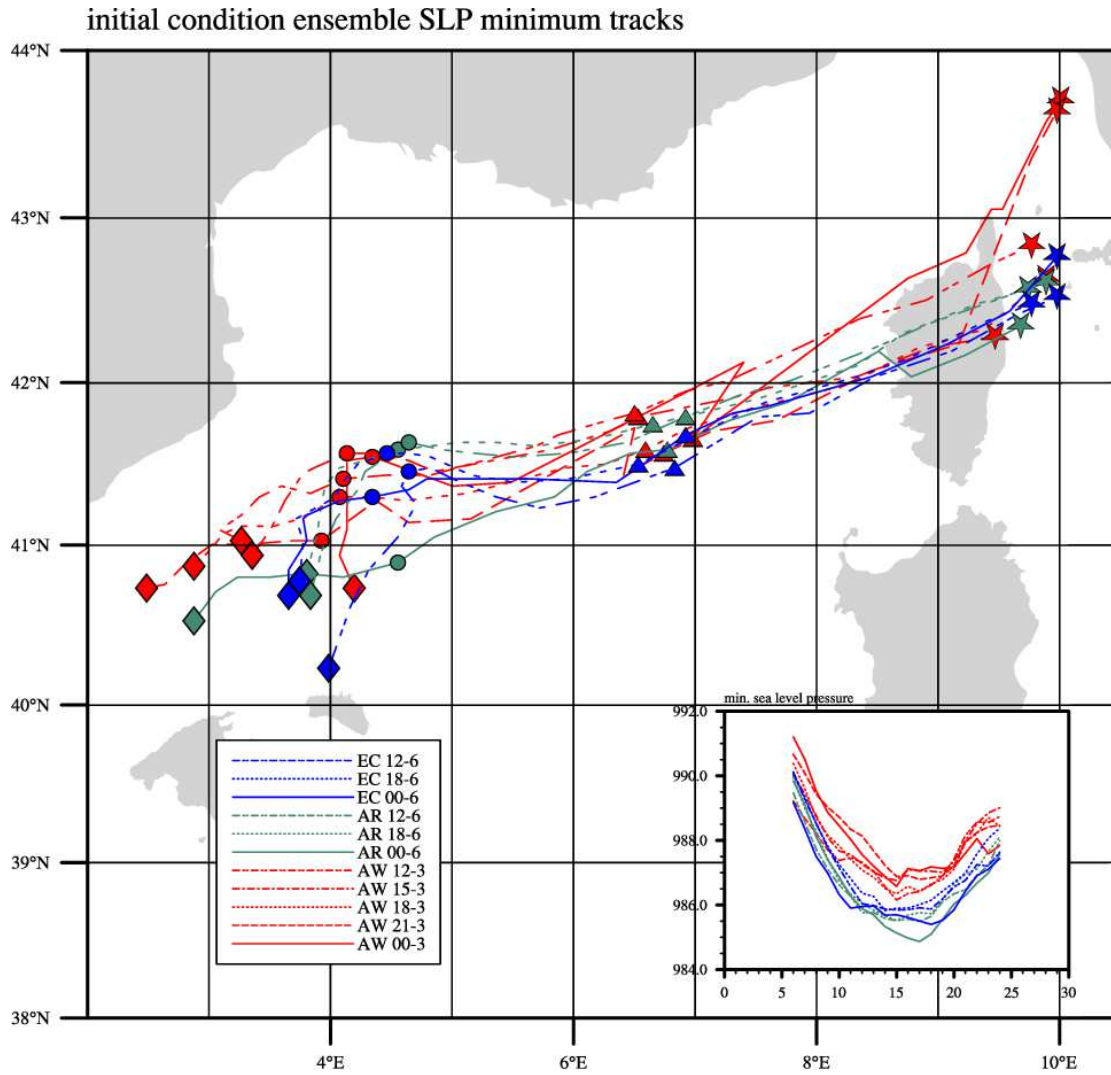


Figure 5.8: Like Fig. 4.8 for 31 Oct 2012. For this case the tracks are limited to time steps from 31 Oct 06 UTC to 1 Nov 00 UTC.

together (around 40 km spread) between 18 and 00 UTC, except for the two outliers **AW 00-3** and **AW 21-3**, which are found about 40-50 km further north and later diverge further from the other simulations, such that they are almost 200 km away from the rest at 00 UTC (stars). These two are also the members which produce the highest precipitation (see Fig. 5.6). **AW 18-3**, **AW 21-3** and **AW 00-3** produce the most extreme precipitation peaks between 06 and 07 UTC and the highest accumulated precipitation of all ensemble members. However, this peak occurs while the cyclone centers are still around 400 km west of Corsica. By the time the cyclones of **AW 00-3** and **AW 21-3** arrive over Corsica, they do not produce any outstanding precipitation features. They are also the ones with the highest core pressure during most of the time. However, the total variation throughout the ensemble is only around 2 hPa.

The algorithm is not working perfectly for this case, as can be seen for the track of **AW 00-3**, which appears to reverse its direction between 18 and 00 UTC. This is due to multiple MSLP minima found within the same cyclone, which vary in intensity. When their depths and spatial extents are close, the performed interpolation can identify one or the other, which gives the impression of the minimum jumping inconsistently. This behavior is not observed for any of the other tracks for the case of 31 October.

5.6 San Giuliano Radiosoundings

The KIT launched seven radiosondes at 03, 05, 08, 11, 14, 17, and 20 UTC of 31 October 2012. The launch site was located in San Giuliano at the east coast of Corsica (see Fig. 1.2). Figure 5.9 shows the values of u and v measured (a) and simulated by the initial condition ensemble (b–l). The most important feature is the zone of negative u from 03 to around 15 UTC below 4000 mASL. During this

time, San Giuliano lies several hundred kilometers east of the cyclone center in southeasterly low level flow. As mentioned above, the most intense precipitation was observed between 06 and 12 UTC, during this phase the cross mountain wind u shows the highest observed values below 1500 mASL. Around 15 UTC the zonal wind changes direction to southwesterly, as the cyclone center approaches from the east and passes northwest of San Giuliano. The observed meridional wind remains southerly throughout the entire observed period except for a shallow (<400 m) layer during the first two hours.

All members of the initial condition ensemble capture the negative zonal wind to varying degrees, but disagree on the exact timing of the change of sign as well as the depth of the layer of negative u . During the first half of the observation period both u and v show a series of rapid changes throughout the initial condition ensemble, linked to the occurrence of convective cells which pass through the model column. After around 15 UTC variability decreases as the HPE becomes increasingly stratiform.

Additional information can be gained from the observed θ_e and θ (Fig. 5.10a). This figure shows that the boundary layer warmed by about 4 K during the measured period from 03 to 20 UTC. In addition, moisture increased until around 15 UTC, the time of the zonal wind direction change, and then decreased again until 20 UTC. Warming and moistening is not limited to the boundary layer but seen throughout the lower and mid troposphere. This cycle of warming and moistening until the afternoon and subsequent cooling and drying is seen in all of the ensemble members. Most of the simulations, however, show abrupt and overestimated cooling of the lower troposphere after 16 to 18 UTC, coinciding with an overestimation of the zonal wind (see Fig. 5.9).

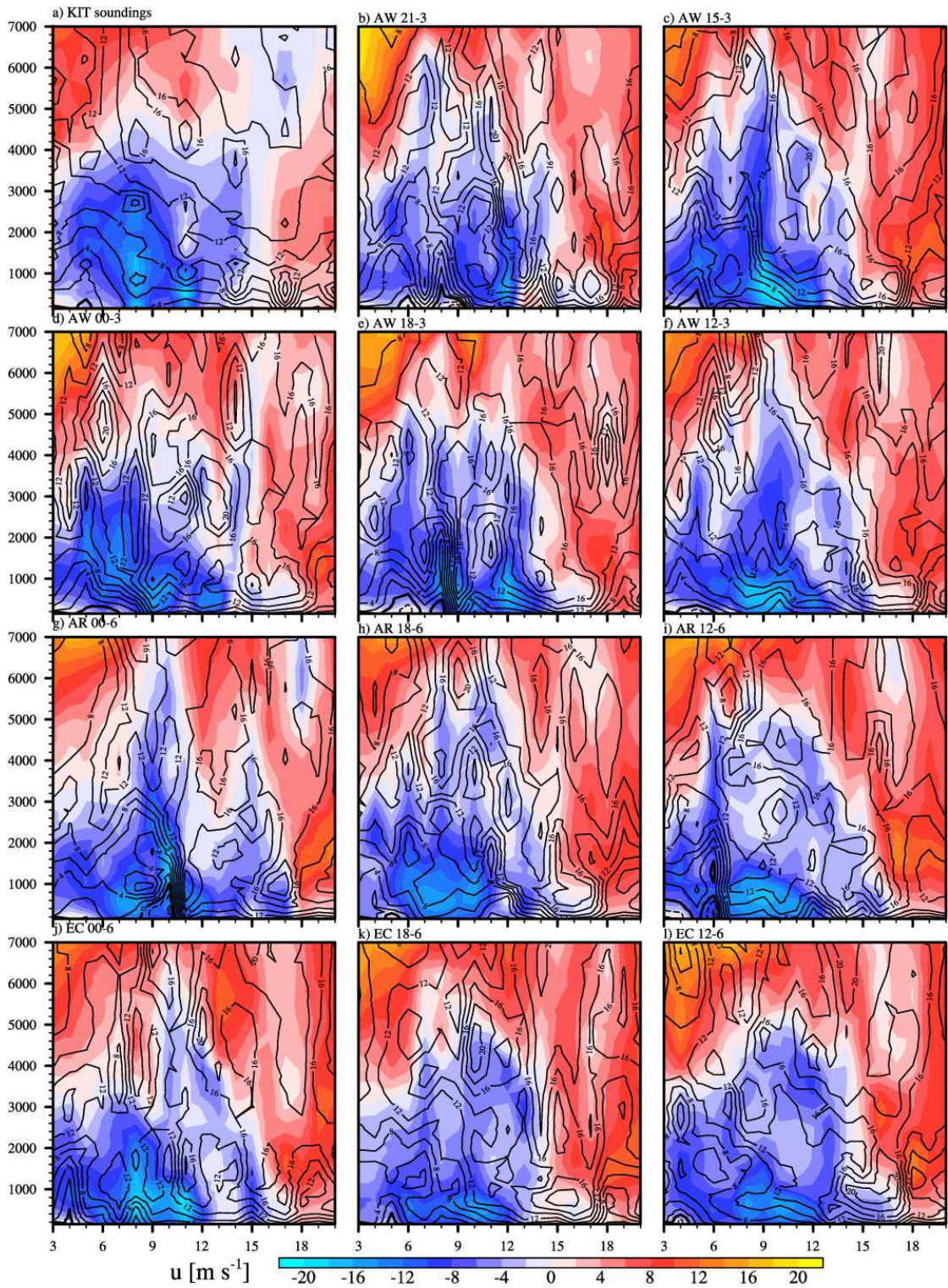


Figure 5.9: Time-height diagrams of observed (a) and simulated (b–l) values for u (color) and v (black contours in intervals of 2 m s^{-1}) in San Giuliano at the east Coast of Corsica. Soundings 03, 05, 08, 11, 14, 17, and 20 UTC, the values between those times were linearly interpolated. Model data from hourly values in the vertical model column closest to the launch site.

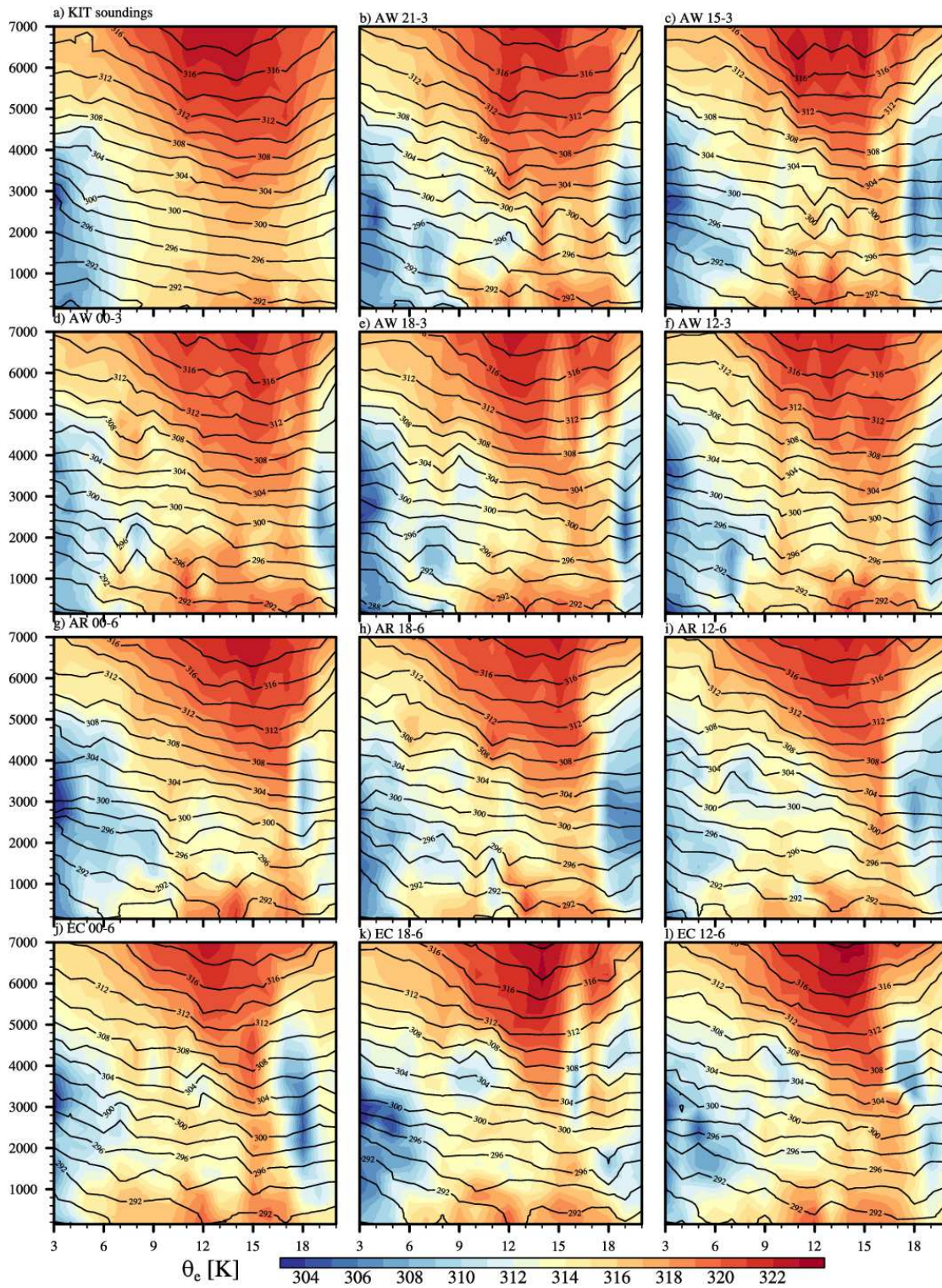


Figure 5.10: Like Fig. 5.9, showing observed (a) and simulated (b-l) values for θ_e (color) and θ (black contours in intervals of 2 K).

From the observational sounding it appears that the initial warming is caused by southeasterly advection of warm moist air from the Tyrrhenian sea, which occurs while the cyclone is still around 400 km west of Corsica. As the cyclone approaches, this advection continues, slowly raising temperature and moisture until 15 UTC, when Corsica is located in the warm sector of the low pressure system. After that, θ begins falling as the cold front approaches. Although low level cooling is seen in some simulations after 18 UTC, this last phase is poorly represented in most simulations, which show a drying of the lower troposphere rather than cooling. The cooling above 4000 mASL is captured by all simulations.

5.7 Evolution of the HPE in the Reference Simulation

Having established confidence in the reference simulation **AW 15-3**, it is now used to explain the development of the precipitation event over time. Three time steps with a representative state are chosen to explain the three peaks seen in Fig. 5.6b. For each of these time steps, Fig. 5.11 shows the observed and simulated hourly precipitation as well as 950 hPa θ_e and wind. This led to precipitation primarily along the mountain range just inland of Corsica's east coast and also over the sea east of the island (Fig. 5.11a). Even though the model is not capable of capturing the exact placement of the precipitation, it succeeds in placing the bulk of the precipitation over the eastern half of Corsica. However, its precipitation extends too far north and is overestimated over the sea (Fig. 5.11b). During this first phase of the HPE at 08 UTC the cyclone was located over the sea between the Balearic islands and Corsica. At this time it induced a southeasterly wind with up to 20 m s^{-1} , which advected warm moist air from the Tyrrhenian sea toward the Corsican orography (Fig. 5.11c).

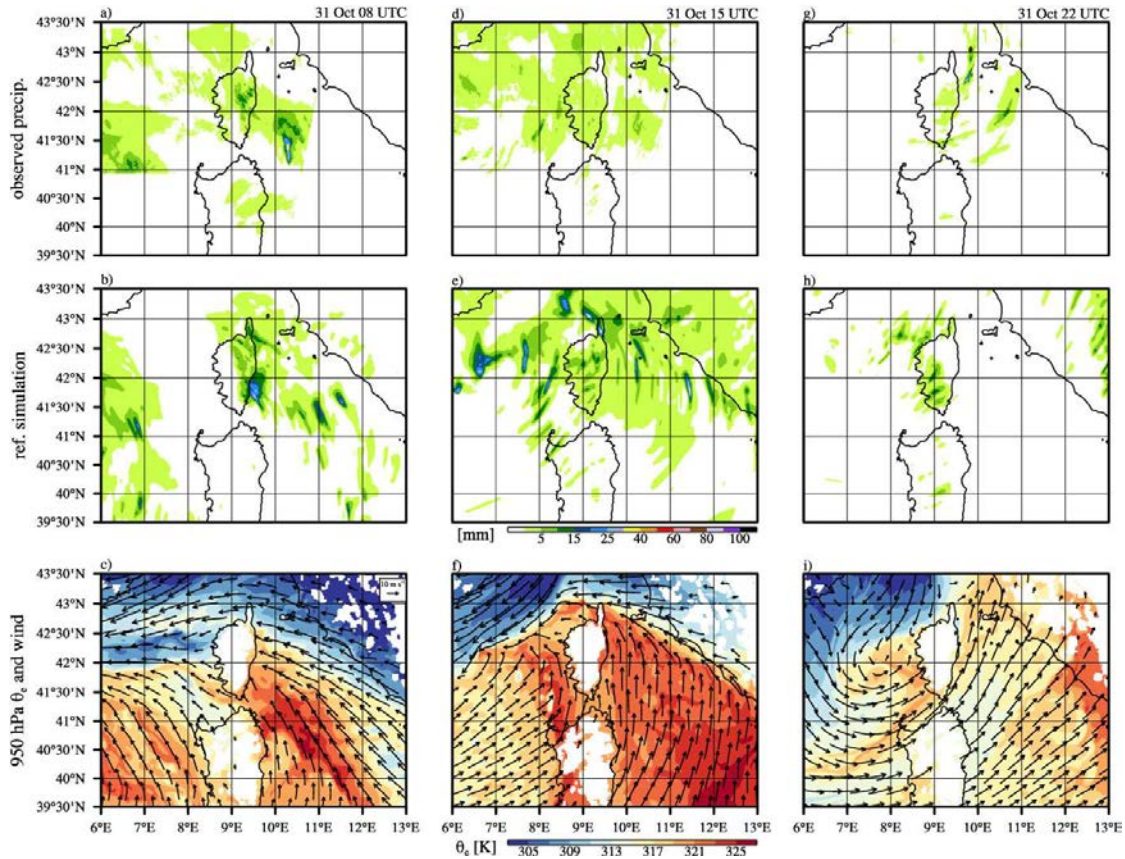


Figure 5.11: Observed (a, d, g) and simulated (b, e, h) 1 hour accumulated precipitation and 950 hPa θ_e and wind (c, f, i) shown for 08, 15, and 22 UTC of 31 October at three representative phases of the HPE.

By 15 UTC, precipitation spread over almost the entire island and had lowered in intensity (Fig. 5.11d). The model overestimates precipitation over most of the island, especially over Cap Corse. Most of the intensity maxima visible in Fig. 5.11e are located over the sea, where no direct observations are available. Moreover, they are relatively far from the radar stations used in Fig. 5.11d, greatly limiting the verification of their exact location and intensity. This phase of the HPE is characterized by mostly southerly flow over Corsica (Fig. 5.11f). While θ_e values and wind are similar to those at 08 UTC, no deep convection forms. Fig. 5.10 shows a relatively warm mid troposphere at 15 UTC over Corsica,

greatly limiting CAPE. In addition, the wind is now almost parallel to the highest mountain ridges, greatly reducing orographic lifting. However, Fig. 5.11e shows an alignment of the precipitation with the smaller southwest-northeast oriented ridges over the southwest of Corsica. While θ_e east and west of Corsica are higher at 15 UTC, precipitation is found mostly along the sharp θ_e -gradient northeast and northwest of Corsica, where convergence and lifting are present. Southwest of Corsica, a north-south oriented line of elevated θ_e coinciding with a jump in wind direction is visible.

At the end of the precipitation event (22 UTC), observed precipitation over Corsica is limited to the southern tip and over the higher orography over the east of the island (Fig. 5.11g). The simulation, lagging the observations by 2 to 3 hours, still produces rain over the southwest of the island. (Fig. 5.11h). At this time, the center of the simulated cyclone has almost arrived at the northwestern coast of the island, with the occluding fronts visible in the θ_e field (Fig. 5.11i). The simulations and observations indicate that the three phases correspond to warm advection ahead of the cyclone in phase 1, with the most intense precipitation found during the phase of the strongest easterly wind toward the coast. Phase 2 was caused by the passage of the warm front, which is indicated by the warming of the troposphere in the radiosounding measurements. Phase 3 is somewhat more diffuse, and while the cyclone center and the occluding frontal system passes over the island, the trough axis passes Corsica at the same time. The three distinct peaks in precipitation are seen best in the initial condition ensemble while they are less pronounced in the observations, especially the third peak.

5.8 Sensitivity to Horizontal Grid Spacing

The configuration of these tests is identical to those presented in Sec. 4.6. A nest with a horizontal grid spacing of 500 m is placed over Corsica. Just like in Sec. 4.6, a test with modified orography at 2.5 km horizontal grid spacing is conducted.

5.8.1 Impact on Precipitation Distribution

The 31 Oct 06 UTC to 1 Nov 06 UTC accumulated precipitation for the new tests is shown in Fig. 5.12b-d with the observations in Fig. 5.12a. A comparison between the reference simulation (Fig. 5.12b) and the nested simulation (Fig. 5.12d) reveals a region of low precipitation in **AW 15-3 nest** extending from the northern coast of Corsica around 9° east all the way to the east coast around 42° north. While such a feature supported by four surface stations over the northwest of Corsica (Fig. 5.12a), it extends too far south in **AW 15-3**. The simulated low precipitation zone cuts through the observed high precipitation zone close to the east coast at 42° north. This problem is reflected in a lowered correlation of the nested simulation, where r is 0.49 in Domain 1 and 0.46 in Domain 2 compared to 0.68 in the 2.5 km reference simulation. However, a more in-depth comparison shows that the change of the precipitation field over land corresponds to an upwind shift and reduction of the precipitation values over the east and an upwind shift over the west and south of the island. This reduces the overestimation seen over the northeast and the underestimation over the west, the exception being Cap Corse, where the overestimation remains. The exact extent of the overestimation is uncertain, as the peninsula is relatively sparsely sampled by observations.

The low precipitation region over northern Corsica in the nested simulation is bounded by high orography on the east and west, shielding it from both sides. The increased resolution and height of the orography partly blocks precipitation

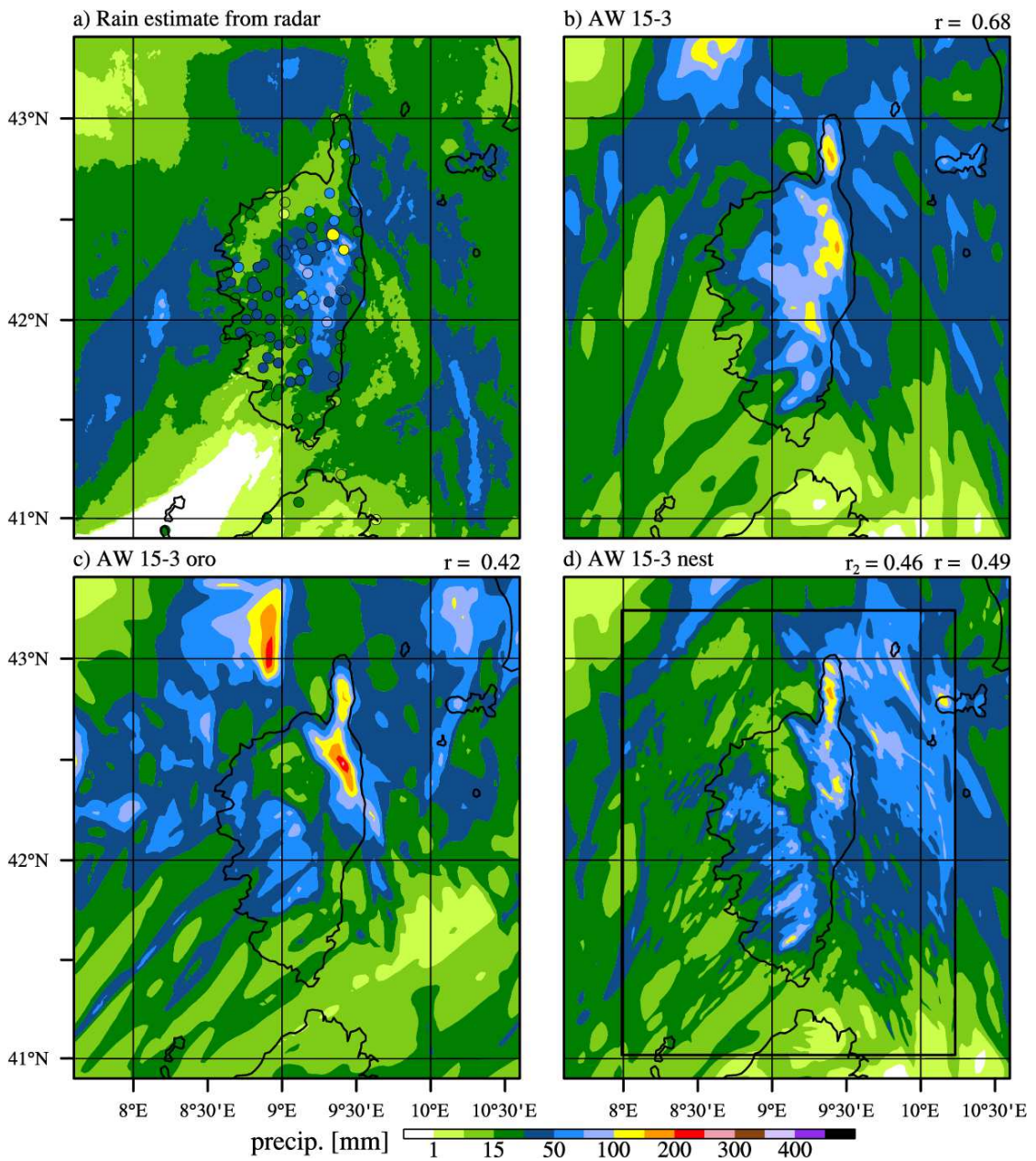


Figure 5.12: Like Figs. 5.4, showing observed (a) and simulated 06 to 06 UTC 24 hour accumulated precipitation for the reference simulation **AW 15-3** (b), **AW 15-3 oro** (c), and the 500 m nested simulation **AW 15-3 nest**.

from both sides. The results of **AW 15-3 oro** (Fig. 5.12c) show that this is not purely a result of the reduced horizontal grid spacing. This 2.5 km simulation with terrain interpolated from the high resolution domain shows a similar area of low precipitation over northern Corsica. Compared to **AW 15-3 oro**, the nested simulation places larger amounts of precipitation further upstream, east of the island over the sea. There is a visible discontinuity in the precipitation field along the eastern boundary of Domain 2, indicating the favoring of precipitation by higher resolution over the sea.

The changes seen for the high resolution simulations are comparable to the changes found for the HPE of 4 September. In both events, a decrease in horizontal grid spacing and also an increase in terrain height, place precipitation further upstream. In addition, precipitation over the sea east of Corsica is increased in the 500 m simulation compared to the 2.5 km simulations. Like for the case of 4 September 2012, the decrease from 2.5 km to 500 m horizontal grid spacing overcompensates the downstream shift of precipitation, placing it too far upstream. This is the case for the convective precipitation over the east coast but not for the more stratiform precipitation over the west and south of the island, which is clearly better captured by the high resolution simulation.

5.9 Test over Flat Orography

An additional simulation, **AW 21-3 flat**, is conducted over flattened Corsican orography. The island itself is not removed and the land use data remains unchanged. For the case of 31 October, the flat simulation reveals that the HPE was not purely dependent on orography like in the other cases.

The observations (5.13a) are shown alongside the reference simulation **AW 15-3** (Fig. 5.13b) and **AW 15-3 flat** (Fig. 5.13c). The most striking difference

5.9. TEST OVER FLAT OROGRAPHY

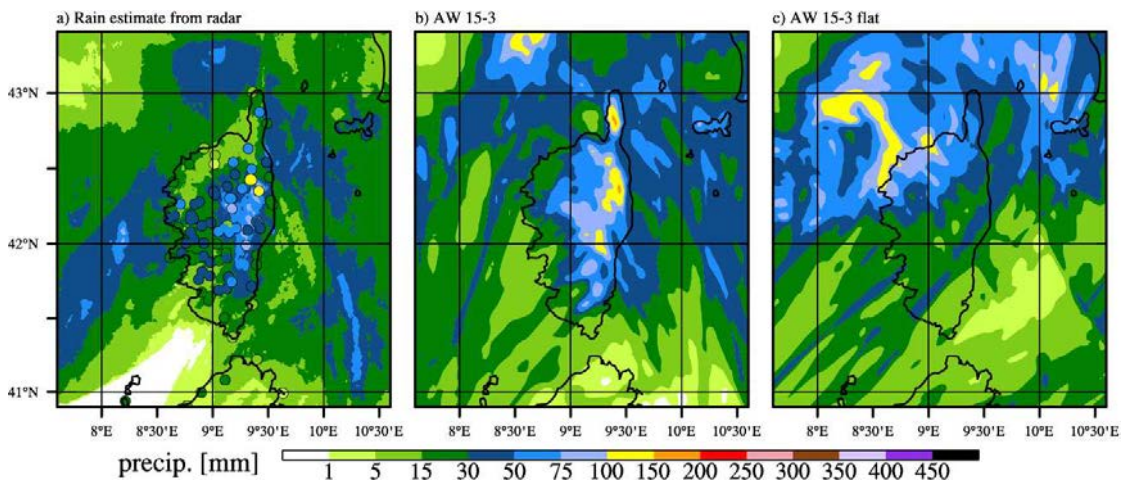


Figure 5.13: Observed (a) and simulated (b,c) precipitation for the reference (b) and flat (c) 24 hour accumulated precipitation from 31 October 06 UTC to 1 November 06 UTC.

in the flat simulation is the absence of the pronounced precipitation maximum over the east of the island. In **AW 15-3** this maximum extends from Cap Corse almost to the southern tip of the island while the strongest precipitation in **AW 15-3 flat** is found over the northwest of the island and northwest and northeast of Corsica over the sea. In the absence of the orographic barrier, the southeasterly wind during phase one of the HPE moves over the island unhindered, only causing heavy precipitation once it encounters the northerly flow coming from the gap between the Alps and the Apennines, which results in the precipitation maximum northwest of Corsica and over the northwestern coast. As the cyclone approaches and its center moves over the north of Corsica, precipitation is found along the occluding frontal system, which covers almost the entire island. In **AW 15-3** this precipitation is concentrated over the west and center of the island, where it is augmented by the orography. However, even without orography, this phase accumulated between 15 and 30 mm over most of Corsica. As the moist air moves northeast over the island, it eventually encounters the gap flows from the north and northeast and the resulting convergence enhances the precipitation greatly. Thus,

the precipitation zone north of Corsica is mainly a result of this convergence and the path of the cyclone center and its frontal system.

For the case of October 31, the flat test shows that the orography is most important for easterly conditionally unstable flow, especially in the absence of other lifting mechanisms like fronts or convergence lines. Together with the results of the flat simulation for 4 September 2012, it also shows that the high precipitation found primarily over the east is indeed closely linked to the mountain range which spans the entire island from the north to the south just inland of the east coast.

5.10 Conclusions

The HPE of October 31 is an example for a fast moving cyclone. Consequently it has multiple phases, each of which characterized by different mechanisms. As the cyclone is still north of the Balearic islands, the main mechanism is southeasterly advection of conditionally unstable air toward the orography along the east coast of Corsica. This phase is mostly dependent on convection initiated by orographic lifting and represents the most intense phase of the HPE. As the cyclone approaches, the wind over Corsica turns south and stability increases as the mid and upper troposphere gradually warms. Orographic lifting remains the primary mechanism while precipitation is more widespread and weaker. The last phase occurs when the cyclone center reaches Corsica and lifting along the frontal system supports the orographic lifting of the southwesterly wind.

The three phases are captured by all simulations of the initial conditions ensemble. However, precipitation is generally overestimated by the model. Comparison to flight data indicates that the presence of too intense convection is the reason for the overestimation of precipitation. **AW 15-3** performs best at reproducing the spatial and temporal distribution of precipitation and is thus chosen as reference

simulation. Based on this reference simulation, a test at 500 m horizontal grid spacing is performed to examine the impact on the simulated HPE. The better resolved orography results in more effective orographic lifting and produces a low precipitation zone downstream of the orography. While such a feature was observed, it is overestimated in the high resolution simulations. Moreover, a test with higher orography at 2.5 km reveals the same but slightly weaker change in precipitation distribution over Corsica. Over the sea, precipitation is higher in the 500 m simulation, showing an overestimation compared to the available observations. This change is not seen in **AW 15-3 oro**, which runs with higher orography but at 2.5 km resolution, which shows that precipitation over the sea for this case is more dependent on horizontal grid spacing than precipitation over land. The test over flat orography confirms the importance of the mountain range for the precipitation maximum accumulated in phase 1. Later precipitation in the flat simulation is more similar to that in the reference simulation but still weaker and lacks the observed alignment with orographic features.

Even though a maximum of only 95 mm day⁻¹ was observed for this event, it was manually included in the climatology presented in Chapter 2. The event of 31 October falls into the winter cluster. However, its non-stationary nature makes this classification difficult. During the beginning of the event, the cyclone is located west of Corsica and southeasterly flow encounters the orography, agreeing with mean fields of the winter cluster. As the cyclone moves farther east, the wind over the island changes to southwest, at which points the event would fit better into the mixed cluster. This underlines one of the primary weaknesses of the clustering in Chapter 2, namely that it can not account for rapidly evolving events.

Chapter 6

Case 3: 23 October 2012 (IOP 15c) - A Highly Localized Convective Event

The HPE of 23 October 2012 (HyMeX IOP 15c) differs from the classic Corsican HPE in duration, location, and spatial extent. It was highly localized, its heavy precipitation band spanning only few tens of kilometers in length and width. In addition, it was relatively short with a duration of the heaviest rain of only around 4 hours. Nevertheless, flooding and extensive damage occurred locally around Porto-Vecchio in the southeast of Corsica (see. Fig. 1.2). The event was poorly forecast with warnings given less than 10 hours before the beginning of the precipitation event. This section is an extended version of the published article (Scheffknecht et al., 2016). Several passages remain as they were published while other parts were expanded or added to accommodate supplementary material.

In particular, issues associated with the turbulence parametrization and its closure assumption are analyzed more in-depth. In contrast to the setup used for cases 1 and 2, the shallow convection scheme used in the coarse grid model

is disabled for this case to eliminate a potential source of differences between the results obtained at different resolutions. Sensitivity tests (not shown) have indicated that the impact of the shallow convection scheme on the simulation results was fairly weak.

6.1 Synoptic Situation

The primary synoptic feature of the event of 23 October was a cut-off low centered northeast of the Balearic islands with a weak surface signal in the sea level pressure (Fig. 6.1a). At 00 UTC, it was slowly (about 15 km h^{-1}) moving eastward between two troughs, visible at the eastern and western edges of the panel (Fig. 6.1a). North of the cut-off lay a blocking high with its center over Germany. The difference between the SLP minimum over the western Mediterranean and at the surrounding coasts was less than 2 hPa. In the boundary layer, represented by the 950 hPa θ_e and wind field (Fig. 6.1b), the cyclonic rotation is well visible with its center just north of Menorca while θ_e is homogeneously distributed around the cyclone center. Warmer air is primarily located over the Tyrrhenian sea between Italy, Corsica, and Sardinia, with smaller zones of elevated θ_e west of the two islands. In the vicinity of Corsica, farther from the center of the cyclone, the wind at 00 UTC was northwesterly. This northwesterly flow originated mainly along the coasts of southern France and northwestern Italy and was forced over the coastal orography by the pressure gradient. This air was relatively dry and cool.

At 06 UTC, during the HPE, the cyclone continued approaching Corsica from the west while deepening (Fig. 6.1c), its SLP signal remaining weak without closed isobars. In the boundary layer (Fig. 6.1d) the situation around the cyclone center remained almost unchanged. However, farther northeast around Corsica the wind changed from northwest to northeast with the flow over the orography

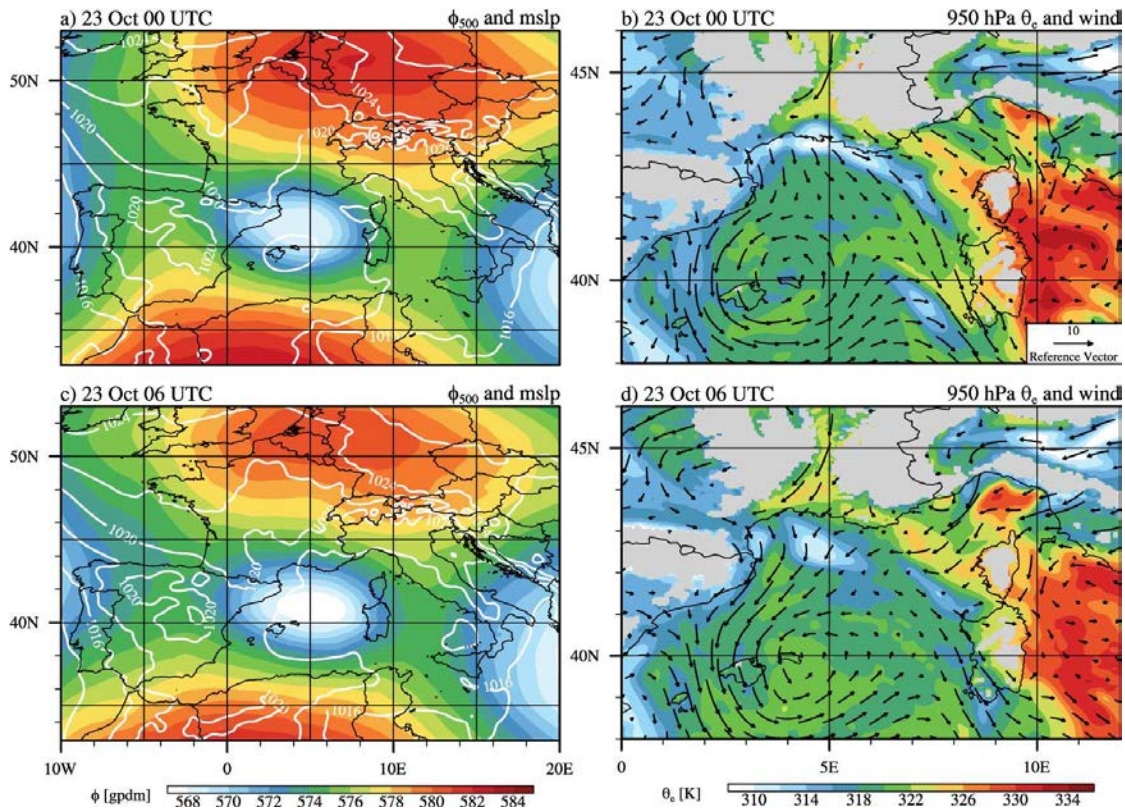


Figure 6.1: Synoptic Situation at 00 and 06 UTC of 23 October over the western Mediterranean as seen in the ECMWF analysis. 500 hPa geopotential and sea level pressure (a, c) and 950 hPa θ_e and wind (b, d).

intensifying. The air around Corsica remained warmest to its southeast where the northerly flow along the island's coast and the westerly flow between Corsica and Sardinia converged.

6.2 Observed Evolution

6.2.1 Satellite Images

The $10.8 \mu\text{m}$ infrared brightness temperature T_b (Fig. 6.2)a reveals a cloud band northeast of the cyclone center, stretching from southeastern continental France

6.2. OBSERVED EVOLUTION

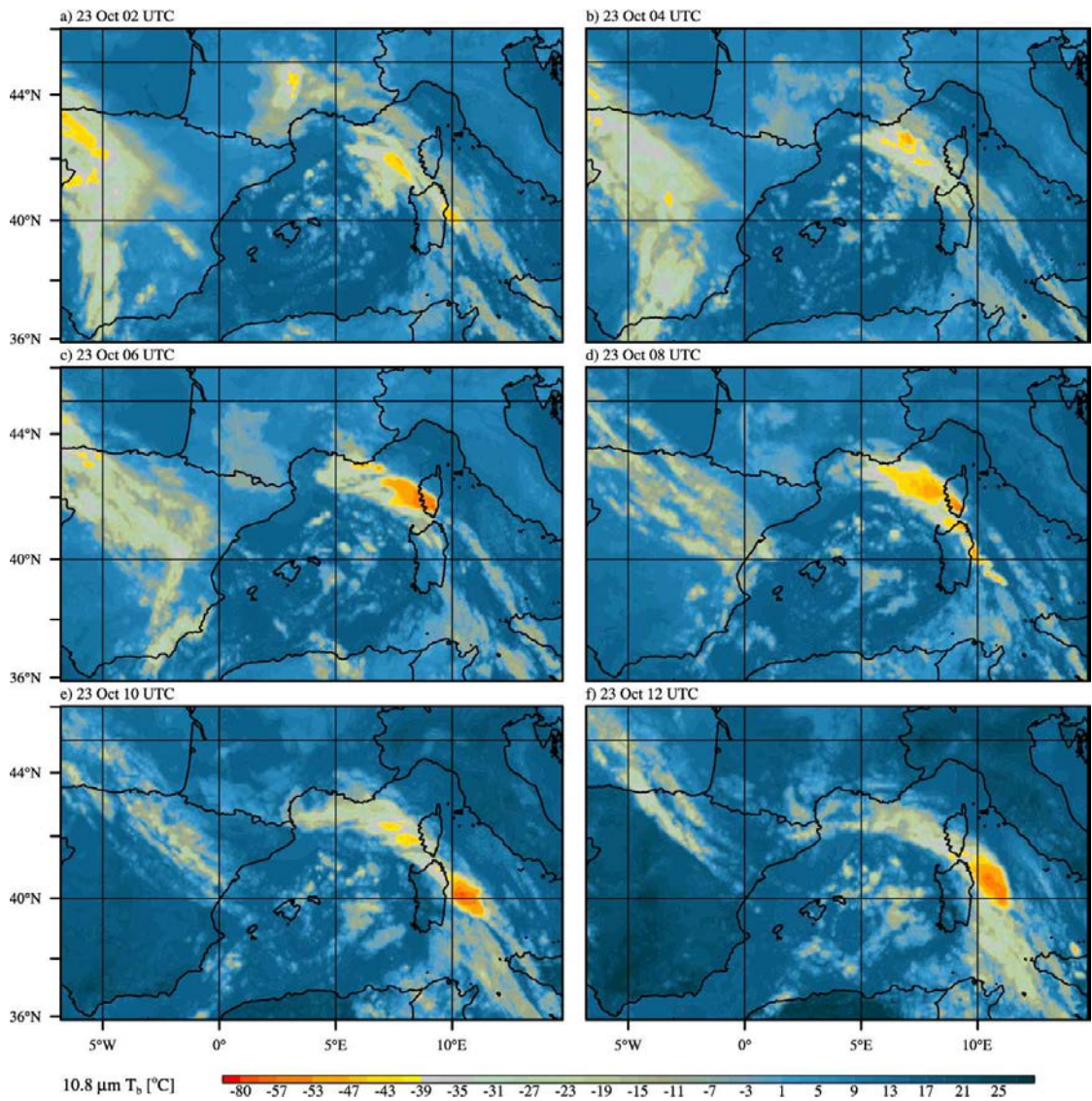


Figure 6.2: 10.8 μm brightness temperature [$^{\circ}\text{C}$] every 6 hours from 23 October 00 UTC to 12 UTC.

over Corsica and Sardinia to Sicily. Scattered zones of low T_b (yellow and orange) indicate that convection was already present in the vicinity of Corsica at 02 UTC (Fig. 6.2a). Convection west of Corsica intensified and moved north between 02 and 04 UTC, when the first convective cell becomes visible over the south of the island (Fig. 6.2b). The convective system over the south of Corsica is well developed at 06 and 08 UTC (Fig. 6.2c and d, respectively). The high clouds are advected northwest with the upper-level wind, shown by the zone of low (<-40 °C) T_b extending from Corsica toward the French coast. After 08 UTC convection over Corsica weakened and by 10 UTC (Fig. 6.2e) the remains of the system are found mainly downstream (with respect to the upper-level wind, i.e. west) of the island. Farther southeast, off the east coast of Sardinia, convection continued throughout most of 23 October, visible at 12 UTC (Fig. 6.2f).

6.2.2 Observed Precipitation

The observed precipitation (Fig. 6.3) confirms that the HPE only affected the south of Corsica. Between 00 and 06 UTC (Fig. 6.3a) precipitation is found only over the southwest of the island with a localized (about 10 by 20 km) but intense band (>150 mm) just inland of Porto-Vecchio. The band extended over the sea east of Corsica. Between 06 and 12 UTC a second highly localized precipitation maximum formed over Porto-Vecchio at the east coast of Corsica (Fig. 6.3b). After 06 UTC, the intense rain band also extends over the sea east of Corsica. The mid- and upper-level wind, which controlled the movement of the convective cells, was southeasterly. The eastern end of the rain band observed off-coast east of Corsica approximately marks the origin of the convective cells. This indicates that orographic lifting was not responsible for convective initiation.

The entire event took place between 00 and 12 UTC of 23 October and the accumulated precipitatin for that period (Fig. 6.3c) shows the heaviest precip-

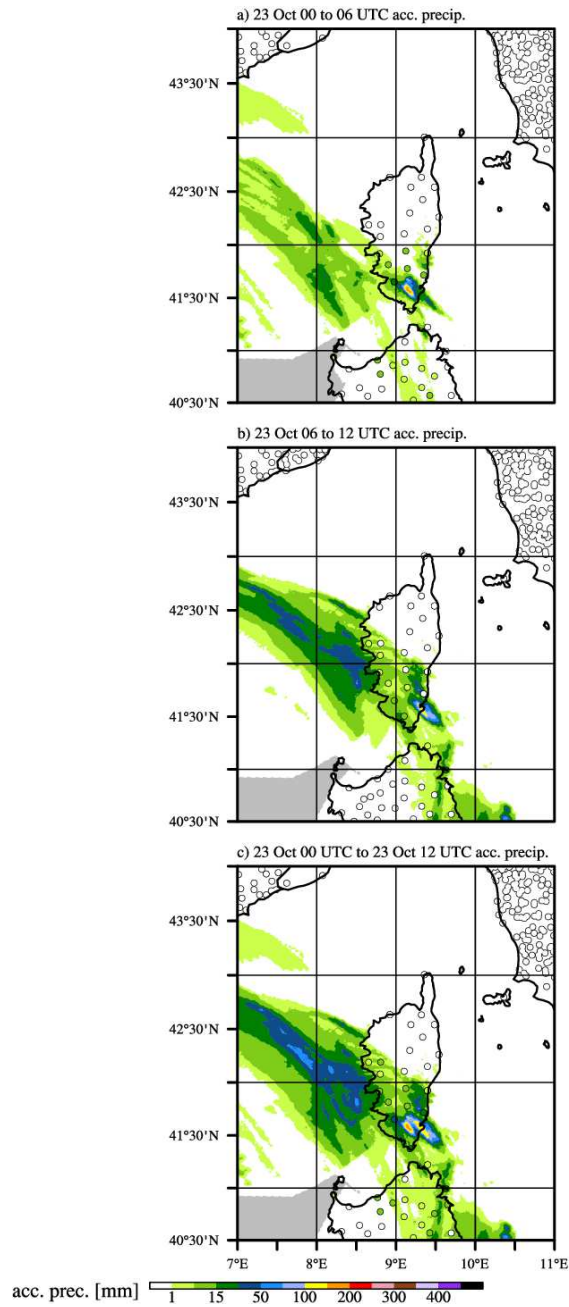


Figure 6.3: Observed rain over Corsica for the event of 23 October. Panels a and b show 6 hour accumulated rain for the 6 hour periods from 23 October 00 UTC and 06 UTC, respectively. The 23 October 00 to 12 UTC accumulated rain is shown in c. The contours show the precipitation estimated from 5 minute radar data. Rain gauges are shown as filled circles.

itation localized over the southeast. With the help of radar data, the highest precipitation is estimated at just over 150 mm per 12 hours. In comparison, the highest raingauge value for the corresponding period is around 31 mm. The observational network used for the HPEe of 23 October consists of the hourly reporting raingauges (Fig. 6.3), of which only 26 are available. This number excludes any stations with missing data during the accumulation period. The narrow and short but intense rain band is located almost entirely between the surface stations and is not properly registered by them. Consequently, using the rain gauges for the calculation of statistics is problematic.

6.3 Predictability and Sensitivity to Input Data Set and Initialization Time

Real time forecasts for the event of 23 October showed a large spread. Warnings were issued less than 10 hours before the beginning of the event, suggesting a low predictability. Model runs initialized earlier than 00 UTC of 23 October did not show a HPE over Corsica. The tests presented below allow a comparison between the simulations driven by the operational global analyses (ECMWF and ARPEGE) and regional high-resolution analysis (AROME WMed). This section has two goals, namely to provide an ensemble of simulations which can be examined with respect to the spread in its results and to identify the best performing simulation and chose it as reference simulation and starting point for further tests.

Fig 6.4 compares 00 UTC to 12 UTC accumulated precipitation, simulated and observed, for all nine simulations. In Fig 6.4a rain-gauges observations represented as filled circles are superimposed on the radar-derived precipitation. No major inconsistency is found between the two sets of observations. However, it is worth noting that the highest precipitation was not captured at all by the too coarse

6.3. INITIAL CONDITION ENSEMBLE

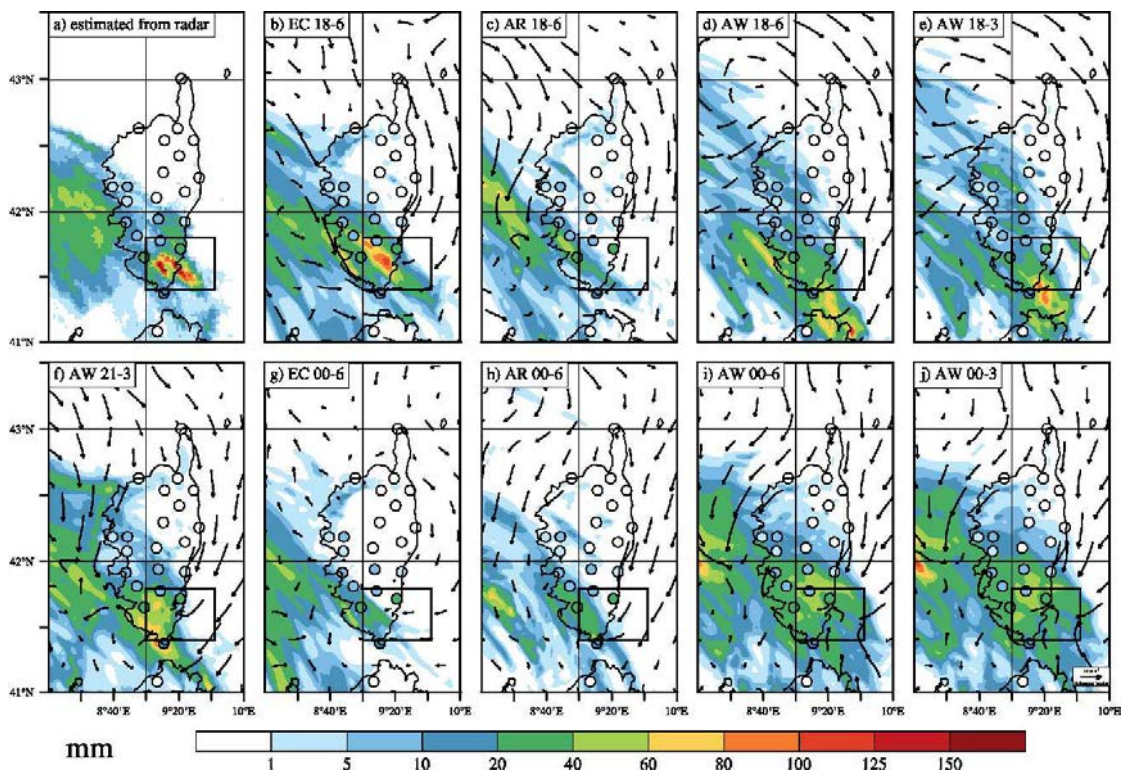


Figure 6.4: 23 October 00 to 12 UTC accumulated precipitation estimated from radar (a) and for the initial condition ensemble members (b-j). 04 UTC wind at 950 hPa is shown for each simulation. The black rectangle marks the averaging region for the precipitation evolution shown in Fig. 6.5. (figure published in Scheffknecht et al., 2016)

hourly reporting surface network. The radar data are extracted from the French radar composite. Corsica is seen by two radars, one located in Aléria on the east coast of Corsica (see Fig. 1.2), and the second in Collobrières on the southern coast of continental France (see Fig. 1.1). Its range limit can be guessed southwest of Corsica over the sea where the precipitation field seems to be "cut off" along an almost straight line. As already mentioned, the east of Corsica is relatively well sampled by the radar in Aléria, while the west of the Corsica suffers from larger uncertainties due to terrain shading.

Simulated fields are shown in Figs. 6.4b to j. The area where the storm was observed is marked on each figure by the black rectangle. All simulations produce a precipitation band over southern Corsica oriented southeast-northwest. This suggests that the large-scale forcing is correctly captured in all the experiments. However, at the meso-scale, and more specifically over the Porto-Vecchio area, the precipitation patterns are significantly different in size, location and intensity. Among the four simulations initialized on Oct.22, 18 UTC, **EC 18-6** and **AR 18-6** show a good positioning but only the former provides accumulated values within the range of the observations. Both **AW 18-6** and **AW 18-3** produce precipitation in excess of 100 mm but place the maximum too far south. These latter two experiments only differ by their coupling frequency. The displacement of the maximum from north Sardinia in **AW 18-6** to south Corsica in **AW 18-3** reveals that the precipitation fields are not only sensitive to the initial conditions but also to the boundary conditions in spite of the large domain size used in this study. The simulation initialized 3 hours later, **AW 21-3**, is fairly similar to its counterpart initialized at 18 UTC (**AW 18-3**). The maximum is slightly shifted westward but is still too far south compared to the observations. None of the simulations initialized on 23 October at 00 UTC produces a localized and intense maximum over Corsica. In both **EC 00-6** and **AR 00-6** the precipitating area is confined to the south-western coast whereas it spreads over most of the island in the two simulations driven by AROME WMed. After 12 hours of integration, the impact of the boundary conditions is less visible than it was after 18 hours and **AW 00-6** and **AW 00-3** yield almost identical results.

To illustrate the boundary layer flow before the observed event, 950 hPa wind vectors at 04 UTC are overlaid in Fig. 6.4. The variability in the upstream conditions is fairly large ranging from northwest to northeast flow depending upon the analysis and initialization time. However, most of the simulations show clear

indication of flow splitting around the island and the simulation associated with the highest precipitation exhibits strong convergence in the lee of the island. An important parameter for the expected flow regime (flow over or around an obstacle) is the upstream Froude number (Fr), which is given by

$$Fr = \frac{U}{NH}, \quad (6.1)$$

where U is the upstream wind velocity, N is the Brunt Väisälä frequency, and $h = 2000$ m is the mountain height used for the calculation ($H_{max}=2039$ m for the model orography). To calculate Fr from simulation output the horizontal mean of the wind velocity and Brunt Väisälä frequency were taken within a box from 8.5 to 9.5° east and 43.25 to 43.5° north, and their average over the lowest 2 km were used to compute Fr . For all ensemble members and simulation times Fr remains between 0.1 and 0.3, indicating a regime which favors flow around rather than over the Corsican mountains. For **EC 18-6** Fr remains smaller than 0.16, clearly favoring flow around Corsican orography.

Besides the intensity and location of the precipitation, the ability of the model to reproduce the timing of the event is an additional criterion to determine the quality of the simulations. This point is examined in Figs. 6.5 a and b which show the temporal evolution of spatially-averaged precipitation rate and accumulated values for all nine simulations together with the radar-derived values. To focus on the Porto-Vecchio event, the comparison is limited to the area marked by the black rectangles in Fig. 6.4 and values are compared between 23 Oct 00 UTC and 12 UTC.

The most striking feature of the two **AW 00** simulations is the early onset of the HPE and the overestimation of the maximum precipitation rate. While the observed event occurred mainly between 04 and 09 UTC, both **AW 00** simulations produce the bulk of the precipitation between 03 and 05 UTC. Despite their

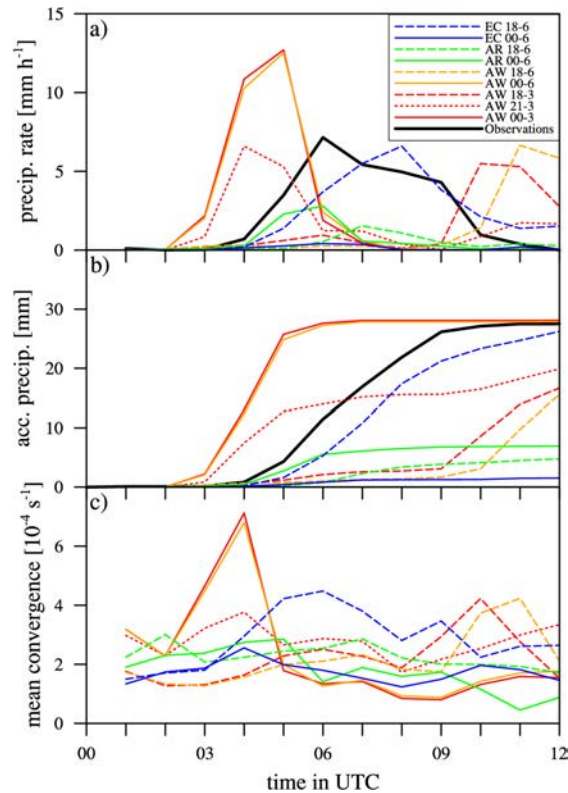


Figure 6.5: Average accumulated precipitation (a) and precipitation rate (b) over southeastern Corsica (region marked in Fig. 6.4). Values are averaged over the entire marked region for each simulation and the radar estimated precipitation. Mean convergence for the same region (c) for the initial condition ensemble members.(figure published in Scheffknecht et al., 2016)

different coupling interval the simulations develop almost identically. **AW 21-3** shows similar timing but only about 50% of the precipitation values seen in **AW 00**. Both **AW 18** simulations delay the precipitation by about four to five hours depending upon the coupling interval. Both simulations produce only about 50% of the observed accumulated values with the precipitation being cut off by the end of the simulation. Thus, the underestimation might in fact be lower. The **AR 00** and **AR 18** simulations both strongly underestimate the total precipitation. Of the two **AR** simulations, **AR 00-6** shows the better timing with regard to the start of the HPE but underestimates both its duration and its intensity by over

60%. **AR 18-6** performs even worse, delaying the precipitation by 3 hours and underestimating it even more. The two simulations using ECMWF data differ strongly from each other. The **EC 00-6** simulation produces less than 5% of the observed precipitation over the examined area while **EC 18-6** performs well, producing accumulated values within 10% of the radar estimate with a delay of about one hour. The maximum of the precipitation rate is delayed by two hours.

To further investigate the role of the lee-side convergence as triggering mechanism, Fig. 6.5c shows the time evolution of the low-level wind convergence computed on the first model level and averaged over the same area as the precipitation. It is clear that for all the simulations which produced a significant amount of precipitation, the rainfall increase is preceded by an increase of the lee-side convergence.

The discrepancies found between the nine simulations are fairly substantial both in intensity and timing of the event. Only six of them produce significant precipitation over the considered area and all but one fail to reproduce the correct timing. Moreover, depending upon the analysis system, the best results are not consistently obtained for the same initial time. Also surprisingly, none of the experiments driven with the highest-resolution analysis is able to capture the observed timing. All these results confirm the predictability issues associated with this event. Based on the results in this section, **EC 18-6** is chosen as reference simulation and starting point for further experiments.

6.4 High Resolution Simulations

Bryan et al. (2003) argued that simulations with a horizontal grid spacing of 1 km show unacceptable values of subgrid turbulent kinetic energy (TKE). However, they acknowledged that such simulations can yield valuable information to fore-

casters. Yet, they strongly recommended a grid spacing of about 100 m for research purposes. Even with the increase in computational resources, such grid spacings are expensive and thus not yet widely used for real cases. Langhans et al. (2012) tested cloud resolving simulations with grid spacings of 0.55 to 4.4 km. They concluded that within their tested range bulk physical properties converged towards the 0.55 km simulations. Honnert et al. (2011) used the Meso-NH model to test different turbulence parametrizations by looking at TKE, boundary layer height and height of the cloud layer for horizontal grid spacings from 62.5 m to 8 km. Their experiments showed that for 500 m simulations, a mixing length based upon Deardorff (1972) with either 3D or 1D turbulence scheme performs best in terms of TKE. However, for the boundary layer height as well as cloud layer height, different configurations performed better. Due to the simple setup in Honnert et al. (2011), their results may not be fully applicable to real case simulations and in particular for moist convective planetary boundary layers. Especially the mixed results in Honnert et al. (2011) show that there is a large degree of uncertainty associated with the treatment of turbulence in Meso-NH within the gray zone. This study provides a chance to test the performance of different model settings for turbulence parametrization for a real case.

Two high resolution simulations with a horizontal grid spacing of 500 m are presented in this section. The model configuration of the 2.5 km and the 500 m simulation is identical except for the turbulence formulation. The 500 m simulations use 3D turbulence while the outer model uses 1D turbulence. While the outer model is run using a mixing length formulation based upon Bougeault and Lacarrère (1989) (BL89), the inner model is tested with both, BL89 and a formulation based upon Deardorff (1972) (DEAR). The two high resolution simulations are named **BL89** and **DEAR** after the corresponding mixing length formulation.

6.4.1 Qualitative Comparison and Evolution of the HPE

The precipitation fields obtained in **BL89** and **DEAR** are shown in Figs. 6.6a and b zoomed in over southern Corsica, with Figs 6.6c and d showing a zoom of the observations and the reference simulation to aid comparison. In **BL89** the precipitation pattern is less localized than in the observations. While **BL89** locates a precipitation maximum only about 10 km south of Porto-Vecchio, it underestimates its intensity by about 30%. On the other hand, precipitation values of over 40 mm extend too far west. In comparison with **BL89**, **DEAR** shows a westward displacement of the heaviest precipitation, with the maximum located over central southern Corsica. However it also produces a secondary maximum just above Porto-Vecchio. Figures 6.6a and b suggest that a change in the mixing length formulation does impact the small scale features of the precipitation field but leaves its overall structure fairly unchanged. The differences seem to mainly arise from differently simulated individual cells. In comparison with the reference simulation, the 500m simulations exhibit a more diffuse pattern with narrower and less intense banded structures. Another notable feature of this comparison is the anchoring of a precipitation band above Porto-Vecchio, present in all three simulations (in agreement with the observations) whereas the second band to the west is fluctuating in its position (but never found where it was really observed).

A detailed comparison of **EC 18-6**, **BL89**, and **DEAR** is shown in Fig. 6.7. Panels a-f show the boundary layer (950 hPa θ_e and wind) and panels g-i show vertical cross sections of the convective event at 07 UTC (meridional wind and θ_e). Before going into detail on the differences, it should be noted that overall the event is simulated similarly in all three simulations, **EC 18-6**, **BL89**, and **DEAR**. All of them show warm, moist air present east and southeast of the island at 04 UTC which is fed into a convergence line southeast of the island by northerly winds east of Corsica. In all simulations the event has a similar duration and the

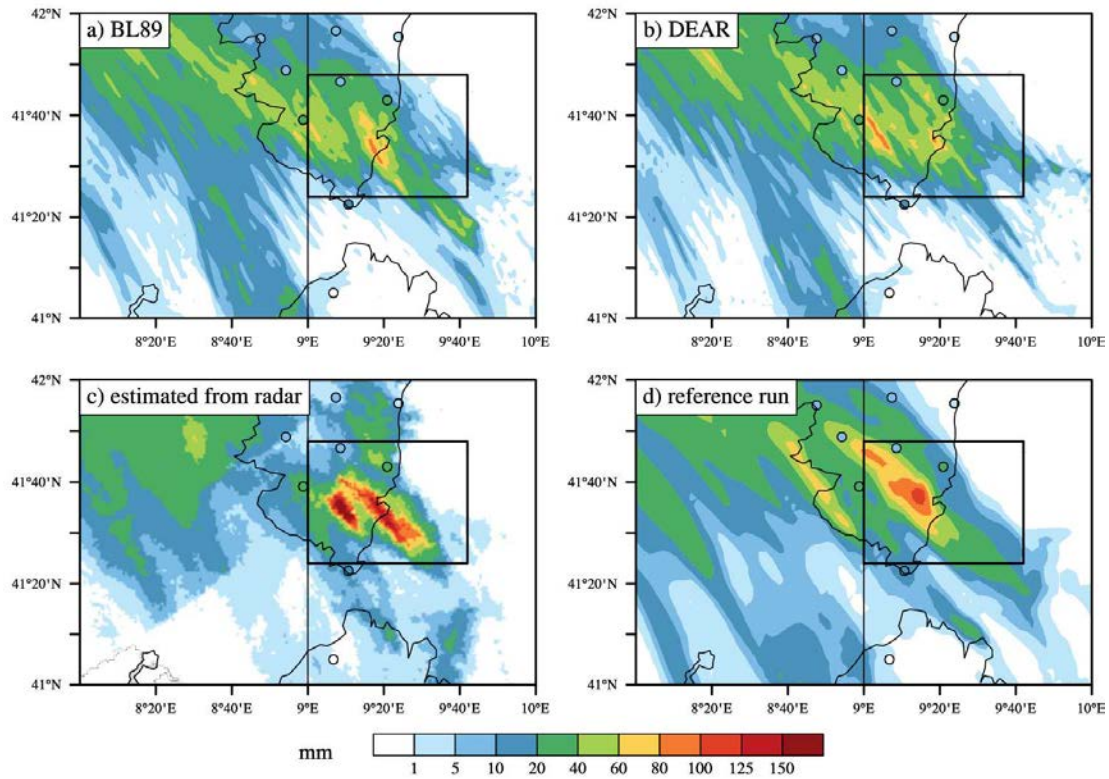


Figure 6.6: Like Fig. 6.4, zoomed over southern Corsica, for the radar estimated precipitation (a) **BL89** (b) and **DEAR** (c). Surface station values shown in circles. (figure published in Scheffknecht et al., 2016)

limiting factor is the advection of cooler air from the north (Figs. 6.7a-f, marked by $\theta_e < 324$ K east of Corsica).

Figure 6.7 further investigates the dynamical and thermodynamical structure of the low-level fields. Starting with **BL89** Figs. 6.7a and b show the distribution of the equivalent potential temperature (θ_e) at 950 hPa at 04 and 06 UTC respectively. The source of energy for the convective system is located east and southeast of Corsica at 04 UTC, characterized by values of θ_e between 326 and 333 K. This places the upstream region of the HPE north of the convergence line and east of Corsica as opposed to the more common cases described by Ricard et al. (2012), where it is located southeast of the island. This warm wedge is gradually fed into the convective system as northerly winds advect it along the eastern coast. Visible north of the warm air, the northerly winds east of the island also advect colder air which reaches the convergence line between 06 and 07 UTC, reducing moisture supply and weakening the system, which dissipates between 08 and 09 UTC. From the southwest the convergence line is fed by slightly cooler and dryer air with θ_e between 320 and 324 K, which originates from northerly flow west of the island. Both air masses are conditionally unstable.

As already suggested by the 2.5 km simulation results presented in section 6.3, the two branches of northerly flow are the result of flow splitting around Corsican orography with the resulting lee side convergence acting as trigger and feeding mechanism for the convective system. While the western branch appears to be weaker at 06 UTC in Fig. 6.7b, it is still present and well developed on lower levels. This is clearly shown by the vertical cross section in Fig. 6.7g. Here, the western branch is shallower and dryer than the eastern branch. However, its northerly component is stronger (12 m s^{-1}) than for the eastern branch (8 m s^{-1}). The western branch might be strengthened by cold air approaching from the west resulting from previous convection offshore. This might also explain how convection west of

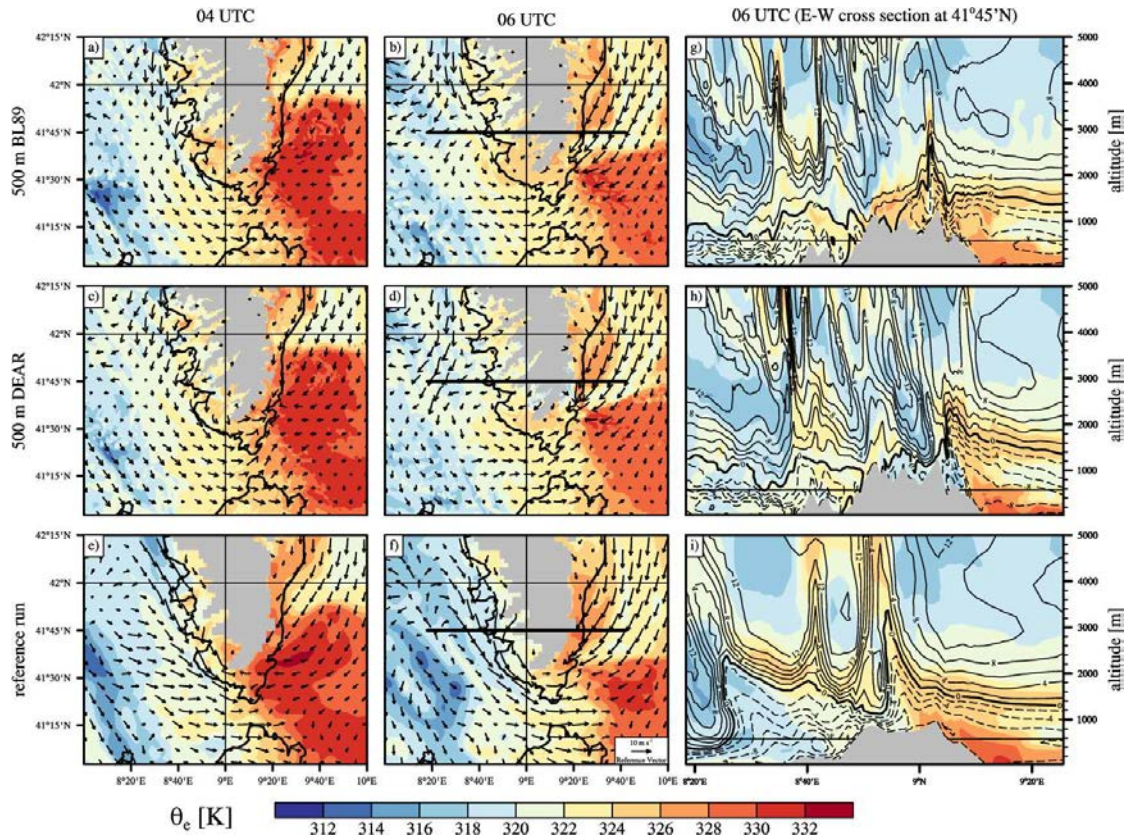


Figure 6.7: 950 hPa wind (vectors) and θ_e (color) (a-f) for the two 500 m simulations and the reference simulation **EC 18-6** on 23 October 2012. Vertical cross section of θ_e (color) and the meridional wind v (black contours) (g-i). (figure published in Scheffknecht et al., 2016)

Corsica is able to influence the strength and location of convergence over the south of Corsica. Figure 6.7g also reveals vertical wind shear of about 15 m s^{-1} east of Corsica between 0 and 3 kmASL for the meridional wind alone. Factoring in the zonal wind (not shown) yields a 0 to 3 km shear of over 20 m s^{-1} . This southerly wind caused convective cells, which initiated over the coast, to move away from the convergence zone and inland over higher orography, allowing the formation of multiple cells over the same region and the accumulation of high precipitation values during the event.

Figures 6.7c and d show that the 950 hPa wind and θ_e for **DEAR** are fairly similar to the corresponding fields in **BL89**. The main discrepancies are found over the topography and west of the island. In Fig. 6.7d, cool outflow is visible in the valleys, as indicated by the lower values of θ_e between 316 and 320 K, and is associated with downvalley flows. This colder air mass is more visible in the vertical cross section shown in Fig. 6.7h, where it is located over the mountains and along the eastern slope. The origin of the stronger cold pool in **DEAR** is stronger convection and more precipitation over the orography around 04 UTC, which also produces the precipitation maximum above 80 mm visible over central southern Corsica in Fig. 6.6c. A second area of discrepancy is found along the western branch of the low-level flow. At 06 UTC in **DEAR** (Fig. 6.7d), the 950 hPa wind west of Corsica is easterly, obscuring the northerly flow along the coast. It is likely associated with the outflow of cold air to its east also due to more active convection over the sea. However, Fig. 6.7h shows that the northerly wind is still present below 950 hPa in **DEAR** and still able to contribute to the convergence in the lee of the island.

Figures 6.7e and f show the corresponding pictures for the 2.5 km reference simulation. Even at 2.5 km grid spacing the model is able to capture the important process of flow splitting and lee side convergence due to the Corsican orography. Initiation and movement of the convective band over Corsica is similar to that in the 500 m simulations. However, the winds along the southwestern coast at 04 UTC in Fig. 6.7e are stronger and closer to high orography in the reference simulation ($\approx 12 \text{ m s}^{-1}$) compared to the 500 m runs ($\approx 8 \text{ m s}^{-1}$). Figure 6.7i reveals that this difference is mostly due to a deeper northerly flow. The highest wind speed is located closer to the island, which might be a consequence of the smoother and shorter terrain along the coast. The difference in orography is clearly visible at $8^\circ 40'$ east, where orography is almost 50% shorter in the reference

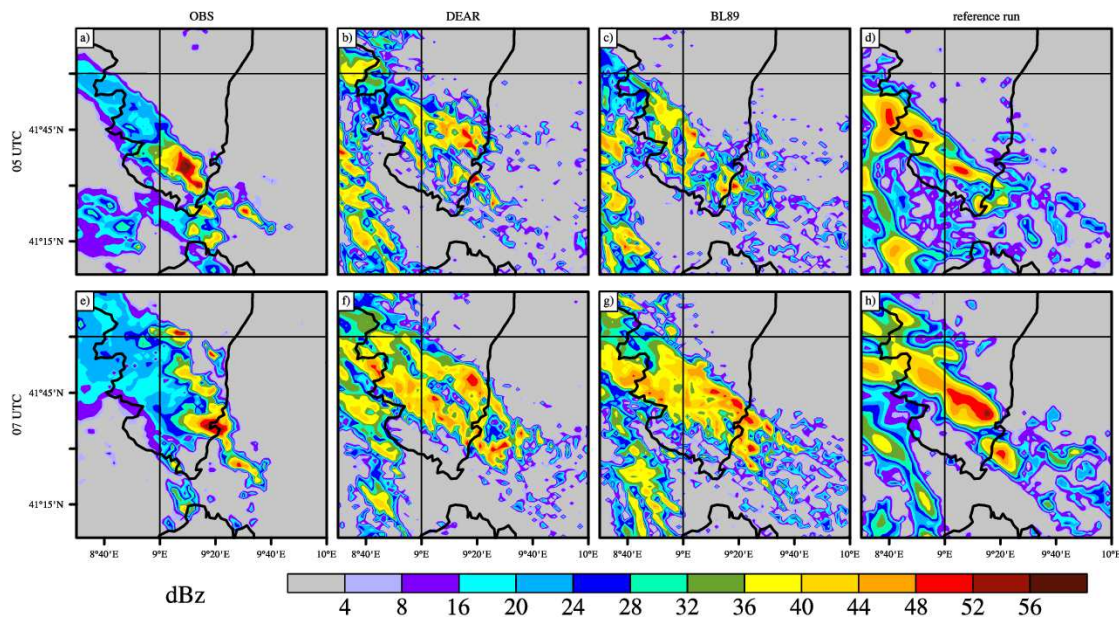


Figure 6.8: Observed (a, e) and simulated (b-d, f-h) radar reflectivity on 23 October 05 and 07 UTC. Figure shows **DEAR**, **BL89**, and **EC 18-6**. (figure published in Scheffknecht et al., 2016)

simulation. The flow west of Corsica is also enhanced by the cold air deposited by earlier convection west of Corsica. The precipitation maximum over southwestern Corsica, visible in Fig. 6.6d, and the corresponding convection is most intense in the reference run. This leaves more cold air along the west coast of Corsica, explaining the difference seen in the θ_e fields and higher wind speeds in Fig. 6.7f.

Radar observations allow to directly localize the strongest convection and heaviest precipitation. Fig. 6.8 compares observed and simulated radar reflectivities. The observations in Figs. 6.8 a and e show the slow movement of the convective system during the two hours from 05 and 07 UTC. At 05 UTC **DEAR** shows the cells smaller, weaker, more widespread and slightly too far north. The cells in **BL89** are better placed but also too small and too weak. On the other hand, the cells in the reference run are bigger than in the observation and also too intense over the west coast (although radar data might not be entirely reliable in this

area). At 07 UTC, both 500 m simulations show a well developed convective band which is more than twice the width of the observed one and show signs of two parallel lines of cells. Only the reference simulation produces a single band and is with that respect closer to the observations. Figure 6.8 clearly illustrates the issues associated with resolution. The convective cells are found too large at 2.5 km horizontal grid spacing, which might result from under-resolved processes. However, smaller grid spacing instead of simply reducing this bias, makes convection too scattered whatever mixing length is considered.

6.4.2 Impact of the Mixing Length Formulation

Calculation of the Mixing Length in Meso-NH

To understand how the differences arise, it is necessary to understand the calculation methods. The formulation of BL89 is a non-local formulation, which evaluates the mixing length upward and downward separately, depending on the subgrid TKE found along the vertical column, where l_{up} and l_{down} are given by

$$\int_z^{z+l_{up}} \frac{g}{\theta_{v.ref}} (\theta(z) - \theta(z')) dz' = -e(z)$$

$$\int_{z-l_{down}}^z \frac{g}{\theta_{v.ref}} (\theta(z') - \theta(z)) dz' = -e(z)$$

where l_{down} is limited by the distance to the surface and $e(z)$ is the TKE at level z , g is gravitational acceleration and θ_v is the virtual potential temperature. The total mixing length L is then calculated from

$$L = \left[\frac{(l_{up})^{-\frac{2}{3}} + (l_{down})^{-\frac{2}{3}}}{2} \right]^{-\frac{3}{2}}. \quad (6.2)$$

It is apparent from eq. 6.2 that the integration depends on the stability not only at level z but also the stability above and below. Even though the mixing length L is generally higher when stability is low, remote stable layers can limit L , such that unstable layers can have low values of L even if they are neutrally stratified. In comparison, DEAR calculates the mixing length purely locally, using

$$L = 0.76e^{\frac{1}{2}} \left(\frac{g}{\theta_l} \frac{\partial \bar{\theta}_l}{\partial z} \right)^{-\frac{1}{2}}, \quad (6.3)$$

where θ_l is Betts' liquid water potential temperature, which is given by

$$\theta_l = \theta \left(\frac{L_v \theta}{c_p T} \right) q_l, \quad (6.4)$$

where θ is potential temperature, L_v is the latent heat of vaporization, c_p is the specific heat at constant pressure, T is the absolute temperature, and q_l is the specific liquid water content. In DEAR, L is limited by the grid size such that

$$L \leq (\Delta x \Delta y \Delta z)^{\frac{1}{3}}. \quad (6.5)$$

DEAR is thus limited by local stability and the grid size whereas BL89 is limited by the stability at, above, and below z . Given a sufficiently deep unstable layer, BL89 can evaluate L to be larger than the grid size. In addition, the two mixing length formulations use different temperatures to evaluate stability. BL89 uses the virtual potential temperature

$$\theta_v = \theta (1 + 0.61r - r_l), \quad (6.6)$$

where r is the mixing ratio of water vapor and r_l is the mixing ratio of liquid water. Thus, the liquid water content is part of the stability calculation in both

mixing length formulations. While the qualitative development of the convective system is similar in **DEAR** and **BL89**, there were differences in the distribution and magnitude of mixing length throughout the model domain. The mixing length formulation was only changed in Domain 2, while the settings for Domain 1 are identical for both simulations. In addition to the two simulations **BL89** and **DEAR**, the 08 UTC output of **DEAR** was used to do a restart run using **BL89**, which was stopped after one time step of integration (4 seconds) to examine the change in mixing length distribution between the two formulations. In the comparison below, this single time step simulation is referred to as **DEARtoBL89**.

Differences in Mixing Length in the Model Fields

Figure 6.9 shows horizontal cross sections through the convective system on 23 October 2012 08 UTC during its intense phase at two levels (2000 and 5000 mASL). The bold black lines shown in Fig. 6.9 show the locations of the cross sections in Fig. 6.10. The simulations which are shown in this section produced a series of convective cells embedded in a cloud band. The lower horizontal cross sections in Fig. 6.9 at 2000 mASL show L and w at the cloud base whereas the cross sections at 5000 mASL cut through the convective updrafts in the mid troposphere.

At 2000 mASL, roughly the level of the cloud base, the most striking difference between the two simulations **BL89** and **DEAR** (Figs. 6.9a and c) is the increased mixing length over large parts of the shown area in **DEAR**. The distribution is inhomogeneous and mixing length is above 300 m over large parts of the domain. In comparison, **BL89** shows much lower values of L over most of the shown area. Even where cells are present, **BL89** does not evaluate L as high as **DEAR** does. In places where **BL89** (Fig. 6.9a) shows increased L , the values remain well below those seen in **DEAR** (Fig. 6.9c). Where the mixing length formulation was changed from **DEAR** to **BL89** (Fig. 6.9e) the values are reduced by about

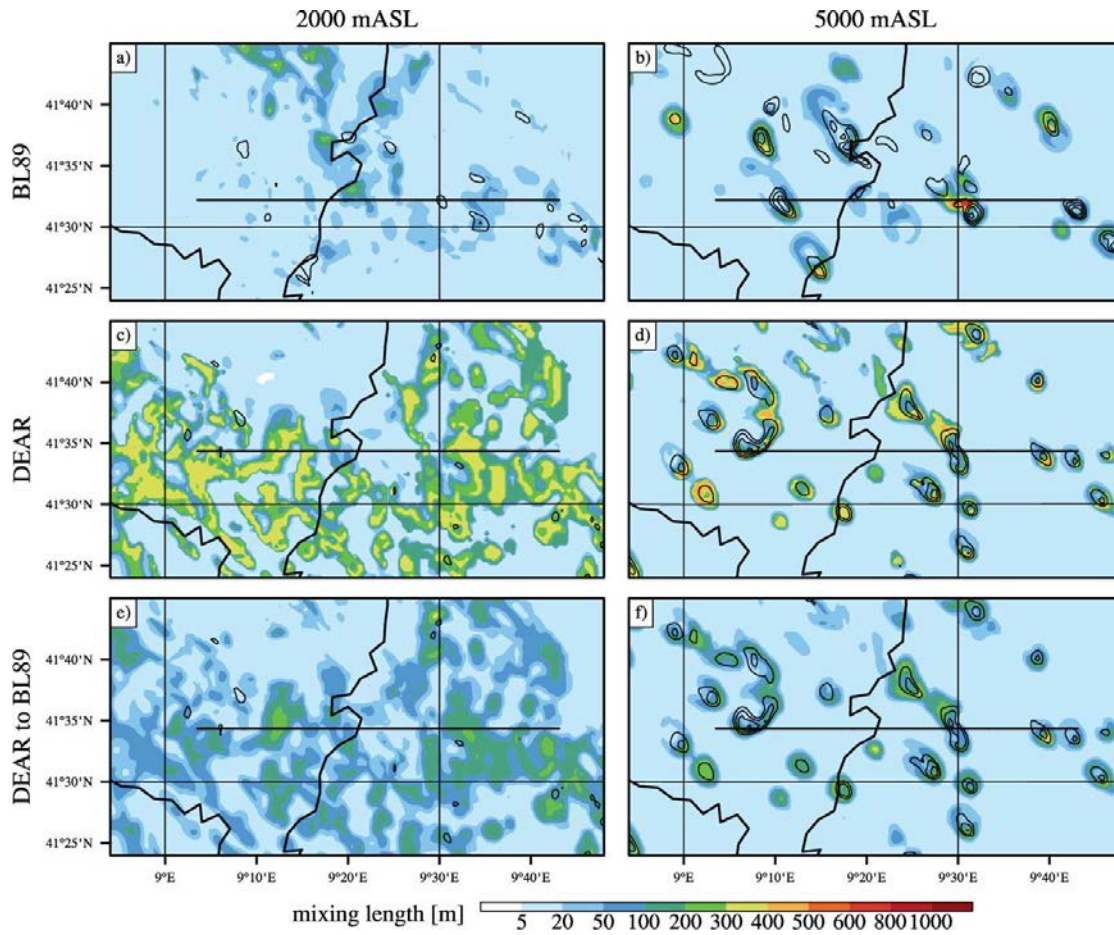


Figure 6.9: Horizontal cross sections of mixing length at 2000 (a, c, e) and 5000 (b, d, f) mASL for BL89, DEAR, and DEAR to BL89 on 23 October 08 UTC. Black contours show positive vertical velocity in intervals of 5 m s^{-1} starting at 5 m s^{-1} . Values are taken from Domain 2. The thick black line marks the location of the cross sections in Fig. 6.10.

25 to 75% and the extended areas of $L > 300$ m are not present. Nevertheless, the structure of the mixing length field from **DEAR** (Fig. 6.9c) can be recognized in **DEARtoBL89** (Fig. 6.9e), showing that the two mixing length formulations produce qualitative differences in the simulations. At 2000 mASL zones of elevated L do not coincide with zones of upward vertical velocity.

In the mid troposphere (5000 mASL, Figs. 6.9b, d and e) **BL89** and **DEAR** show less extreme differences. Convective cells are well visible in the vertical velocity (black contour lines) as well as in the mixing length (color) field. Counting purely the number of visible updrafts (as shown by the first contour of $w = 5 \text{ m s}^{-1}$), the number of visible updrafts is 22 for both simulations **DEAR** and **BL89**. However, L seems to be more correlated to w in **DEAR**, where almost every visible updraft has a visible signature of $L > 100$ m whereas **BL89** shows several updrafts which have no visible signal in L . Interestingly, these signatures in L are retained in **DEARtoBL89** (Fig. 6.9f). There must thus be a difference between the simulated updrafts in **DEAR** and **BL89**.

As was stated above, **BL89** is non-local, meaning that the stability at levels above and below each grid point is taken into account when evaluating L . Therefore information on multiple levels in the vertical is necessary to understand the mixing lengths at any given height. Figure 6.10 shows vertical cross sections, where L , w and stability shown by $d\theta_v/dz$ is visible for entire columns. For **BL89** Fig. 6.10a shows that the updrafts with visible signatures in L at 5000 mASL are those which reach a height of at least 8000 mASL, whereas weaker and shallower convection shows only has weaker or no visible impact on L . On the other hand, **DEAR** shows visible signatures in L for all convective updrafts and even the shallower cells show updrafts of over 10 m s^{-1} , which is not seen in **BL89**. The strongest updrafts are taller and stronger in **BL89** than in **DEAR**, indicating that **BL89** favors stronger and deeper updrafts at the cost of weaker and smaller ones while

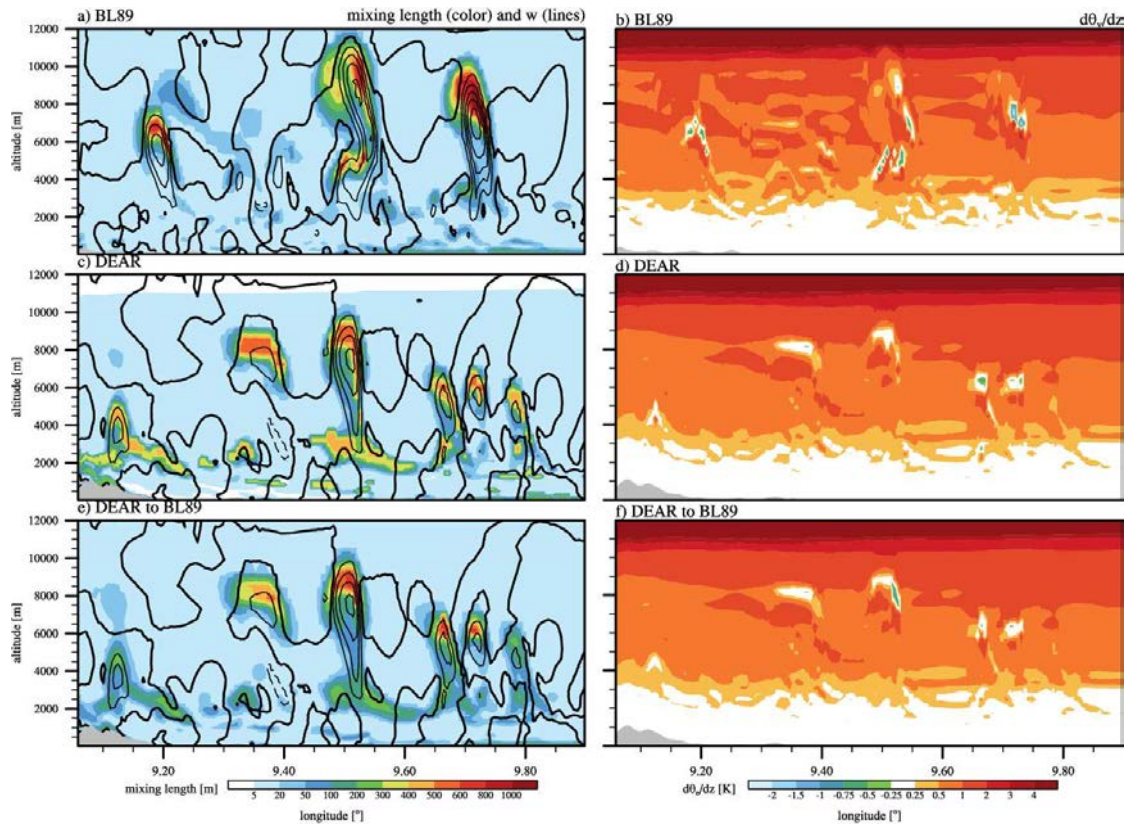


Figure 6.10: Vertical cross sections of mixing length (color) and w (black lines) (a, c, e) and $d\theta_v/dz$ (b, d, f) for BL89, DEAR, and DEAR to BL89 on 23 October 08 UTC. Values are taken from Domain 2.

hardly influencing the overall number of updrafts. In **DEAR** L is limited by the grid size around the cloud base as well as in the upper troposphere around the top of convective updrafts. **BL89** produces the highest values around the top of deep convective updrafts while L remains mostly below 200 m around the cloud base. This shows how DEAR allows large L even when the unstable layers are shallow, as opposed to BL89, where a deep unstable column is necessary for large L . This condition is only fulfilled within deep convective updrafts.

Switching from DEAR to BL89 (Fig. 6.10e) changes the mixing length instantly. **DEARtoBL89** still shows close resemblance to **DEAR**. Within the shallow layer of low stability around the cloud base BL89 immediately limits L

while it produces higher values than DEAR around the tops of the deep cell in the center of the cross section. The cross sections of stability (Figs. 6.10b, d and f) show that overall stability, measured by $d\theta_v/dz$ is relatively similar in **DEAR** and **BL89**. BL89 allows stronger negative vertical gradients of θ_v in the mid and upper troposphere but both simulations show multiple zones where $d\theta_v/dz$ is negative, such that the atmosphere is absolutely unstable to the vertical displacement of an unsaturated parcel. However, all these zones are found close to convective updrafts, indicating that they are located within clouds, where liquid water has to be taken into account. **DEARtoBL89** changes the distribution of these unstable zones within only four seconds, indicating a profound impact of the mixing length on stratification.

The results in this section show, that the mixing length formulation does have a strong impact on the distribution of the mixing length around convective clouds. While BL89 produces the highest values (>1000 m) around the top of deep convective updrafts, DEAR reaches its limit of L , given in Eq. 6.5, around the top of updrafts as well as the cloud base. As a consequence of the vertical grid stretching DEAR produces higher values of L in the upper troposphere (around 500 m) than at the cloud base (around 350 m). BL89 favors deep and strong updrafts at the cost of smaller ones while the updraft strength in DEAR is more evenly distributed. Despite producing significantly different distributions of mixing length around convective plumes, the results for the HPE of 23 October 2012 for both mixing length formulations are fairly similar. The comparison to radar data does not reveal if any of the mixing length formulation produces a more realistic cell size distribution, as both of them appear similar in size and number in the simulated radar images.

6.5 Sensitivity to physical parametrizations

The experiments discussed in section 6.3 show the decisive influence of model initial conditions. On the other hand, higher horizontal resolution does not change the overall development of the event. However, it does change the precipitation distribution. To further explore the sensitivity of the simulated system, a stochastic ensemble of nine members is obtained by introducing random perturbations to the microphysics and turbulence parametrizations using the same method as Fresnay et al. (2012) and Hally et al. (2014a,b). The ensemble is obtained by applying random factors to the time tendency in the microphysics and turbulence schemes (for details, see Fresnay et al., 2012; Hally et al., 2014a)). The results of the individual ensemble members are not discussed. The goal is to assess the importance of model physics relative to changes in initial conditions as well as obtaining a general measure of sensitivity of the simulated event.

Figure 6.11a and b show the 40 mm isohyets of the accumulated precipitation for both, the initial condition and the model physics ensembles. For the initial condition ensemble (Fig. 6.11a) there is a large spread in the distribution of precipitation among the different members. The variability is particularly high over the southeast of Corsica, where the HPE was most severe. West of Corsica the sensitivity is lower. In the model physics ensemble (Fig. 6.11b), the most notable feature is the persistence of the HPE over the southeast of Corsica, which was captured with variable intensity but at roughly the same location by all nine members of the ensemble. In this ensemble, larger variability is found over the west of Corsica, where the secondary precipitation maximum along the coast is not visible for every member or displaced further inland. To ease comparison, Fig. 6.11c shows the number of ensemble members which simulate more than 40 mm of accumulated precipitation for each given grid point. Only the maximum over Porto-Vecchio is represented in all members of the ensemble while the most

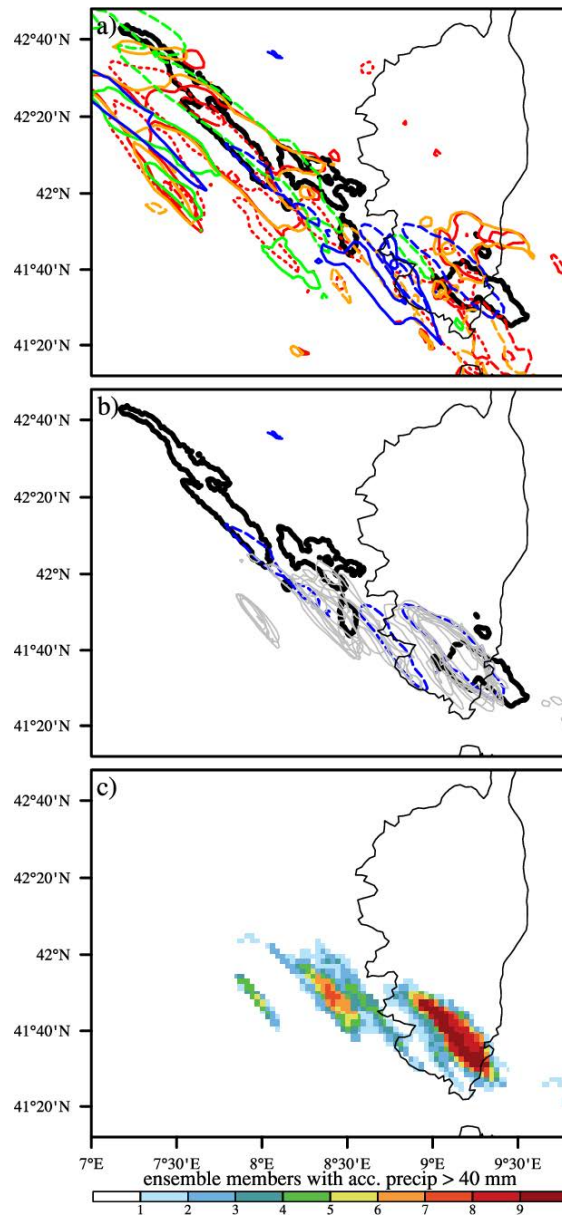


Figure 6.11: Comparison of the 40 mm isohyet for 00 to 12 UTC accumulated precipitation in the initial condition ensemble (a) and physics ensemble (b). Observation is recalled in black. Colors in (a) are the same as in Fig. 6.5. In (b) the reference simulation is represented in dashed blue and the nine perturbed members in gray. The colored contours in (c) show the number of ensemble members which simulate more than 40 mm of precipitation between 00 and 12 UTC of 23 Oct 2012 for each given location. (figure published in Scheffknecht et al., 2016)

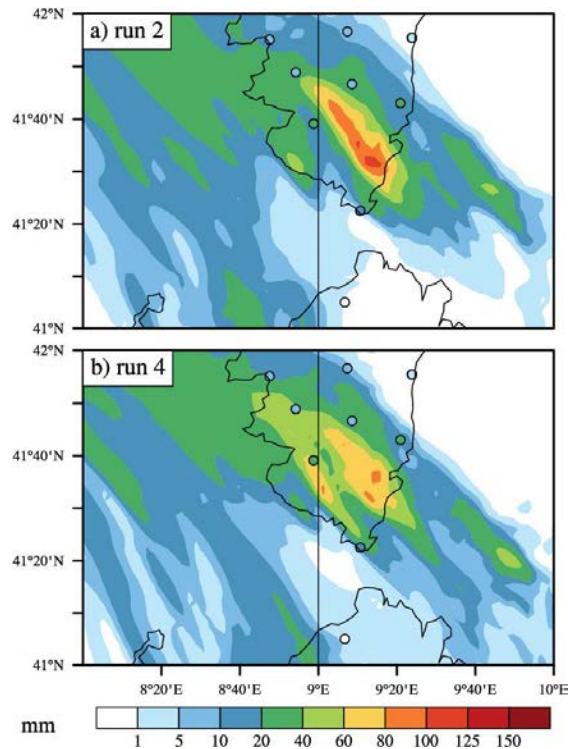


Figure 6.12: 23 October 00 to 12 UTC accumulated precipitation like in Fig. 6.4 for members 2 and 4 of the physical ensemble. (figure published in Scheffknecht et al., 2016)

persistent precipitation maximum West of Corsica is only captured by 7 ensemble members.

Even though Fig. 6.11b shows little sensitivity for the placement of the precipitation maximum over the southeast of Corsica, there are notable differences between the simulations. As an example, Fig. 6.12 compares the 00 to 12 UTC accumulated precipitation obtained for two of the nine ensemble members. The location of the maximum around Porto-Vecchio agree well for the two members. However, the maximum values are different. While member 2 produces a maximum of 106 mm, the precipitation in member 4 is more widespread and the maximum reduced to 86 mm. Another notable difference is the absence of a secondary maximum over the southwest of Corsica in member 2, while member 4 produces values

of over 80 mm. Over southwest Corsica, similar high sensitivity of the precipitation pattern was obtained when the resolution was increased or when the mixing length was switched from BL89 to DEAR.

In all members of both ensembles precipitation is organized along an about 70 km wide band ranging from the southeast of Corsica up to southern continental France. Despite the large spread between the members of the initial condition ensemble, all simulations redistribute precipitation only within this band but do not change its location. For the physics ensemble, the spread is much less. Here, the variability is mostly limited to changes in intensity. Fresnay et al. (2012) and Hally et al. (2014a,b) also found that in the presence of orography, perturbations to the model physics had less impact on the precipitation distribution than over lower terrain. The tests shown in this section suggest that the storm in Porto-Vecchio was primarily controlled by the interaction of the low-level flow with the topography and that its position was more sensitive to fine-scale initial condition uncertainties than to uncertainties in model physics.

6.6 Physical Process Study

6.6.1 Analysis Departures

The initial condition ensemble obtained in section 6.3 shows not only that predictability was low, but also presents an array of different developments for the HPE of 23 October. Thus, examining the initial conditions should yield some insight into which features of the analysis fields were important. This section discusses the differences between the input data sets and their impact on the development of the event. To examine the initial conditions, Fig. 6.13 shows CAPE and 950 hPa winds for 22 Oct 18 UTC and 23 Oct 00 UTC for each analysis data set.

Figure 6.13a shows the initial conditions for the reference simulation, the 18 UTC ECMWF analysis. When comparing them to the 18 UTC ARPEGE analysis, shown in Fig. 6.13b, three important differences are notable. Firstly, CAPE values east of Corsica are higher (more than 1500 J kg^{-1} up to the northern end of Corsica in ECMWF vs. less than 500 J kg^{-1} for ARPEGE) and extend further north. Together with the northerly wind, this provided more CAPE for a longer period of time via northerly advection into the convergence line. Secondly, the northerly wind east of Corsica was more developed and occupied a deeper layer in the ECMWF analysis. In Fig. 6.13b, the northwesterly wind west of Corsica is confined to lower levels and not visible at 950 hPa (similar to Fig. 6.7d and h). Lastly, west of Corsica, CAPE is higher in the ECMWF analysis, yielding stronger convection and reinforcement of the northerly flow west of Corsica by cold pools leading to an along-mountain low level jet and possibly shifting the convergence line further northeast.

At 00 UTC, elevated CAPE values are present east of the island for both, the ECMWF (Fig. 6.13d) and ARPEGE (Fig. 6.13e) analyses. Contrary to what is seen at 18 UTC, at this time the northerly winds are stronger and CAPE is higher in the ARPEGE analysis. West of Corsica none of the two analyses shows CAPE values much higher than 750 J kg^{-1} , restricting the energy available for convection. This also weakens the possible enhancement of northerly flow west of Corsica due to cold outflow, which explains in part why convergence and precipitation form further southwest and are weaker in **EC 00-6** and **AR 00-6** than in the reference simulation.

Even though AROME WMed is the model with the highest resolution and its analysis is the one with the highest amount of assimilated observations, the AROME-based simulations do not produce the best results. Explicitly represented convection has affected the fields of the AROME WMed analysis and depleted

the CAPE. At 18 UTC this is visible in Fig. 6.13c, west of Corsica and east of northern Sardinia, where CAPE values are below 500 J kg^{-1} . In comparison with the ECMWF and ARPEGE analyses, the zones of high CAPE are narrower and confined to the coastal regions. In **AW 18-3** and **AW 18-6**, spurious convection along the east coast consumes most of this available energy already before 00 UTC, thus greatly reducing the available moisture and energy at the time of the observed event. As a result, both **AW 18** simulations develop very differently from the other ensemble members and strongly delay the occurrence of the storm in Porto-Vecchio .

At 00 UTC, conditions in the AROME WMed analysis in Fig. 6.13f show moderate northerly wind east of Corsica with speeds of around 10 m s^{-1} and CAPE values between 1000 and 2000 J kg^{-1} . South of Corsica, the CAPE field is characterized by a sharp gradient (located at 41° north in Fig. 6.13f), which marks the northern end of a large cold pool. This cold pool is the result of earlier convection in the AROME WMed model which generated the analysis. The details on this earlier convection remain unknown as the temporal resolution of the analysis data is too low to examine the convection itself. This convection is not captured by the ECMWF and ARPEGE analyses. However, is not totally unrealistic as satellite images indicate that deep convection is present at that time over the western coast of Sardinia. This convection might be overestimated in the AROME WMed analysis. In **AW 00-3** and **AW 00-6** the cold air west of Sardinia moves north and causes a convergence line, which propagates northward at almost 40 km h^{-1} hampering the development of a stationary system. The peaks in the convergence and precipitation shown in Fig. 6.5 mark the passage of this line over Porto-Vecchio. The analysis for 21 UTC is not shown here, however it is similar to the analysis at 00 UTC. The system in **AW 21-3** develops qualitatively similar to the to **AW 00** simulations but is less intense.

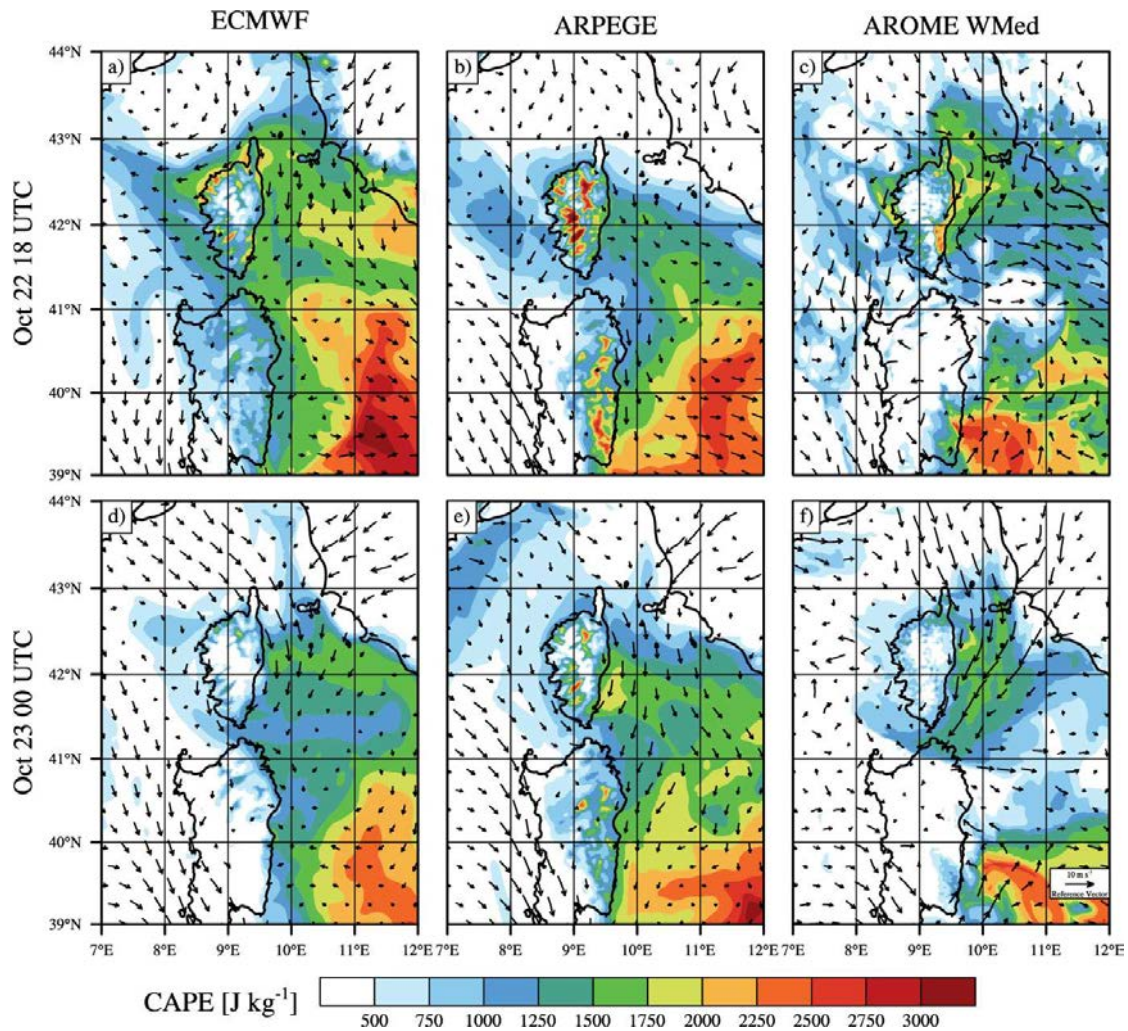


Figure 6.13: Comparison of CAPE and 950 hPa wind for ECMWF, ARPEGE and AROME WMed analyses at 22 Oct 18 UTC and 23 Oct 00 UTC. (figure published in Scheffknecht et al., 2016)

The differences in the mesoscale fields around Corsica seem sufficient to explain most of the differences seen between the members of the initial condition ensemble. However, an influence from the larger scales can not be ruled out. While it is tempting to attribute differences on the mesoscale to differences in the mesoscale initial fields, several studies have shown that error propagation from the large to the small scale is capable of strongly changing mesoscale processes within only six hours of simulation time (e.g. Reinecke and Durran, 2008; Nuss and Miller, 2001). In both of these studies, the large scale flows interact with complex orography via nonlinear processes. This is also the case for the HPE over Corsica presented herein. However, even in much simpler models (Durran and Gingrich, 2014) the propagation of errors up and down the scales is equally fast. In fact, Durran and Gingrich (2014) show that even small errors on the large scale can greatly limit mesoscale predictability. Thus, an impact of the large scale differences of the initial fields can not be ruled out, even if they appear to be well captured in all of the analyses.

While the differences between the four **AR** and **EC** simulations seem to be closely linked to the low level wind direction and distribution of CAPE before the onset of the HPE, **AW** is strongly influenced by earlier convection and the resulting cold pools. This clearly shows one possible problem when initializing from a data set where convection is already resolved. Potential gains through higher resolution input can be more than offset by misplaced or overestimated and underestimated convection. Even though initialized from the lowest resolution data set, **EC 18-6** produces the best results. The results shown in this section underline the importance of well captured upstream conditions and suggest that the Porto-Vecchio event was highly dependent upon advection of moisture and CAPE from north of the convergence line. In the next two sections, the role of

the topography is further investigated by conducting additional tests based upon **EC 18-6**.

6.6.2 Role of the Corsican Orography

A simple way of testing the sensitivity of an orographically forced HPE to the underlying orography is to run a simulation where terrain features are removed. The simulation in which the orography of Corsica is set to zero is designated **flat**. When the model orography is lower than the orography in the analysis the model extrapolates the conditions down to the new surface level. Even if the extrapolation is carefully designed and constrained by climatological relationships, this process tends to replace the terrain with warm and moist air. To account for this and to avoid the development of immediate spurious convection, moisture is corrected before the start of the simulation. This is done by interpolating the values over the island from moisture values over the surrounding sea, where the surface level remains unchanged. After four hours of simulation no artifacts are visible in the output fields.

Figure 6.14a shows the 00 to 12 UTC accumulated precipitation for the **flat** simulation. The maximum at Porto-Vecchio is no longer present when flattening the orography. Instead, more precipitation falls along a continued band over southwestern Corsica. The maximum is found along the west coast with intensity and location fairly similar to those reference simulation suggesting that the precipitation over the west coast is not controlled by orographic processes.

Figures 6.15a and b show the 950 hPa θ_e and wind at 06 UTC for the reference and flat simulations, respectively. In **flat**, the northerly wind over the island is already well established at 06 UTC and the boundary between high and low θ_e lies over Corsica. Along this boundary, multiple cells are initiated due to convergence, leading to the precipitation maximum over southwestern Corsica visible in Fig.

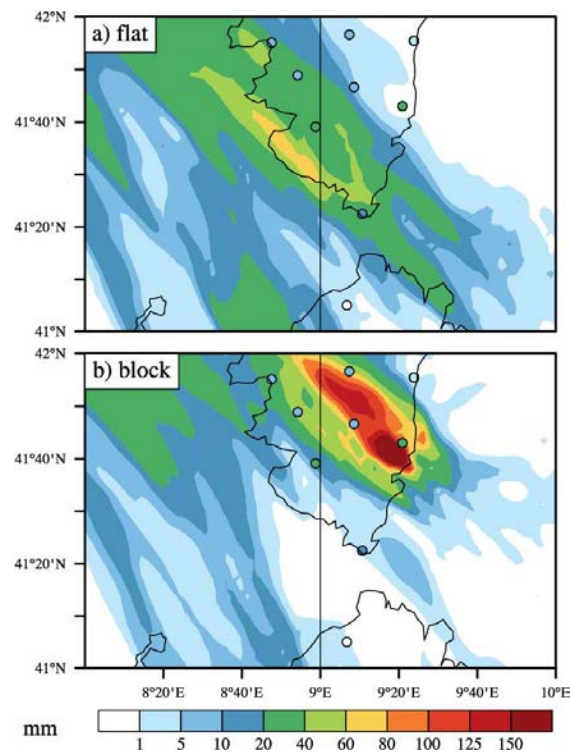


Figure 6.14: 23 October 00 to 12 UTC accumulated precipitation like in Fig. 6.4 for the **EC 18-6 flat** and **EC 18-6 block** simulations. (figure published in Scheffknecht et al., 2016)

6.14a. As cold air from the north approaches and flows over the flat island, the warm air over the southeast of the island is gradually replaced. However, as the western branch of the flow is no longer diverted and accelerated by the topography, the replacement is slower than in the reference simulation. Due to the absence of strong convergence in the lee of the island, no HPE is simulated over the southeast of Corsica. Contrary to the results of Barthlott and Kirshbaum (2013), the complete removal of the island (test not shown) does not reduce the precipitation notably compared to **flat**. These results show that the southeast of Corsica does not receive high values of precipitation if the island's orography is removed, which further supports the hypothesis that orographically induced lee side convergence was a necessary condition for the HPE of 23 October.

6.6.3 Role of the Gap Flows

In the reference simulation, the northerly flow around Corsica seems to be fed in part by the gap flows from the Genoa and Florence area and blocking these flows should weaken it. However, modifying this flow without directly changing the 3-D fields of the model requires a different approach. To block the gap flows, the height of the Italian mountain chains from the French-Italian border to central Italy is increased by up to 3000 m prior to the start of the simulation. Tests with different heights (not shown) showed that less drastic changes are incapable of blocking the inflow of cool air into the Mediterranean basin until the end of the HPE. This new simulation is referred to as **block**. Blocking these flows is achieved by adding the height of three bell shaped mountain ridges to the existing terrain. The resulting mountain range exceeds heights of 4000 m and is able to block the inflow of cold air into the western Mediterranean basin until the end of the precipitation event. No spurious downslope winds or other artifacts develop until 23 October 12 UTC.

The bell shaped mountains are defined by a line between two points P and Q , where P' is the closest point of the line between P and Q to the respective grid point $X_{i,j}$. Point X , given by model coordinates i and j is then altered by adding h to the local terrain height. The added height h is given by

$$h_{i,j} = h_{max} * e^{-\frac{\|X-P'\|}{a}}, \quad (6.7)$$

where $h_{max} = 3000$ is the maximum height and $a = 15000$ m defines the mountain width. Three of these mountains are placed along the Apennines before starting the simulation.

The **block** simulation shows higher values of accumulated precipitation than the reference simulation. Figure 6.14b shows values of over 150 mm (max. 260 mm) for the 12 hour accumulated precipitation. The event is four hours longer than

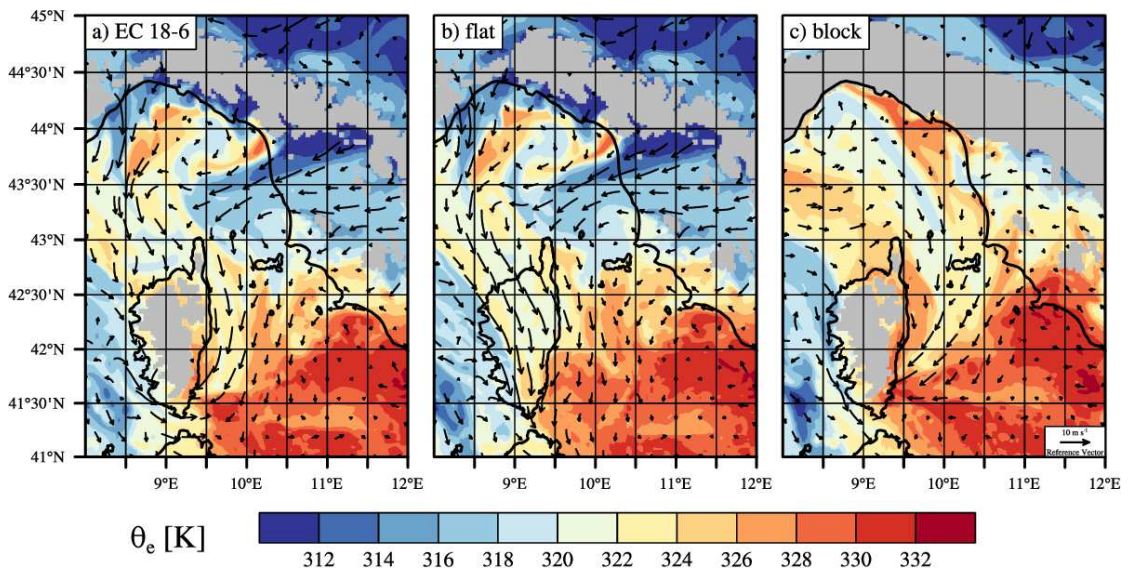


Figure 6.15: 950 hPa θ_e and wind vectors on 23 October 06 UTC for **EC 18-6**, **flat** and **block**. (figure published in Scheffknecht et al., 2016)

in the reference simulation. The 950 hPa wind vectors east of Corsica in Fig. 6.15a indicate that the northerly winds advect cooler air, which eventually leads to the dissipation of the system in the reference simulation. Figure 6.15c shows that the blocking of the gap flows north of Corsica results in a warmer boundary layer and weaker northerly winds east of Corsica. The gap flows are replaced by air from northwest of Corsica and, more importantly, from further southeast along the Italian coast where moist and highly buoyant air is located. Figure 6.15c shows that the inflow into the convergence line has a larger easterly component, resulting in a rich supply of warm and moist air. The convergence zone in **block** remains stationary for more than 7 hours and dissipates after 11 UTC.

This result suggests that the gap flows were indeed an important element for the HPE of 23 October. However, blocking them changes the flow east and north of Corsica, effectively changing the location of the upstream region for the HPE. Nevertheless, the **block** simulation shows northerly flow along the east coast and still contains elements of flow splitting around the Corsican orography. The HPE

which forms in **block** is qualitatively similar to the HPE in the reference simulation and its triggering time and location are almost identical. It is therefore possible that different synoptic conditions north of Corsica could have caused a more severe event by delaying its dissipation. On the other hand, a stronger pressure gradient over the Italian coast might have prevented the system from forming over the southeast by replacing most of the buoyant air before the start of the event. This shows that gap flows can have a crucial role in HPEs over Corsica and that they should be considered when assessing a potential threat.

6.7 Quantitative Precipitation Verification

The precipitation verification for the event of 23 October 2012 is based purely on visual comparison and the temporal evolution of the precipitation simulated by the model and estimated from radar. This was done because the quantitative comparison used in Chapters 4 and 5 was not feasible for the case of 23 October. The comparison is provided in this discussion for the sake of completeness and because it illustrates the limitations of the employed statistical methods.

The Taylor diagrams (Taylor, 2001) in Fig. 6.16 show the difficulties when using Person's correlation coefficient r on a small sample. For this case the precipitation was limited to the period from 00 to 12 UTC, requiring the use of only 25 hourly reporting rain gauges. This limitation results in a large spread of the ensemble members, which is especially apparent when looking at the 10 members of the microphysics ensemble, shown in gray. Their spread is almost as high as the spread of the initial condition ensemble, even though it was shown to have a smaller spread with respect to precipitation timing, location, and intensity. The bulk of the HPE was located between rain gauges, such that essential information on the HPE is not contained in the Taylor diagram for 23 October 2012.

6.7. QUANTITATIVE PRECIPITATION VERIFICATION

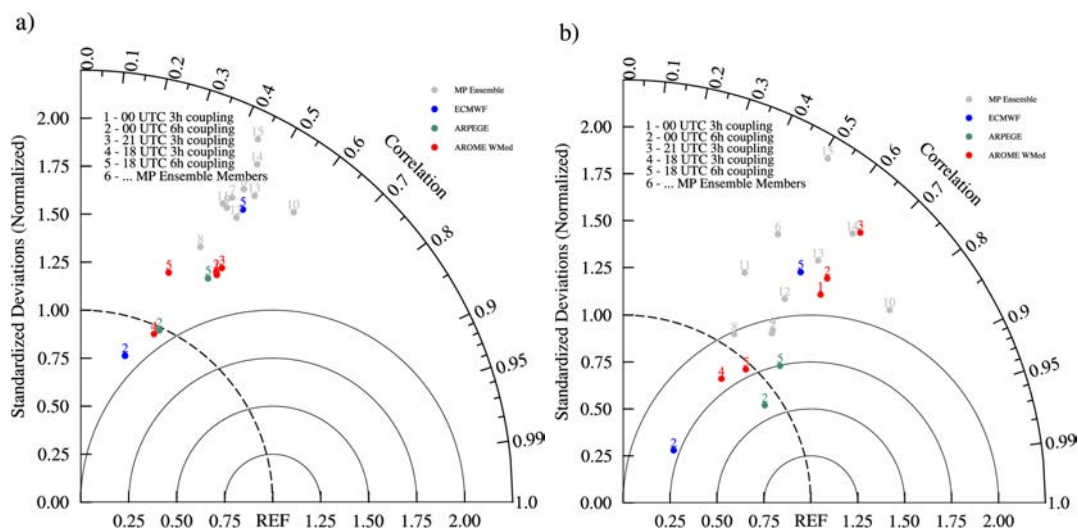


Figure 6.16: Taylor diagrams of the initial condition ensemble for 23 October 2012. The diagrams are based on the 00 to 12 UTC accumulated precipitation showing the results for the entire domain (a) and only the stations on Corsica (b).

Despite this limitation, certain features are consistent with the setup of the ensemble experiments. Namely, the members of the MP-ensemble are located around the reference simulation **EC 18-6**. Moreover, the two pairs of simulations which were initiated from the same data and at the same time but with different coupling interval (**AW 00-3** and **AW 00-6** as well as **AW 18-3** and **AW 18-6**) are found closer to each other than to any of the other simulations initiated from the same data set (Fig. 6.16b). **AW 00-3** and **AW 00-6** are represented by the red dots labeled 1 and 2 whereas **AW 18-3** and **AW 18-6** are represented by the red dots labeled 4 and 5. However, this does not hold for **AW 18-3** and **AW 18-6** for the entire domain (Fig. 6.16). Interestingly, the reference simulation **EC 18-6** (blue dot labeled 5) is identified to perform much worse than most of the other simulations when compared to the limited observations.

The values (r , MAE , and NB) are given in Table 6.1. They further underline the problem with sparse observations, as **ECM 18-6** has a higher MAE and NB and lower r than several other simulations which capture the HPE poorly.

Exp. Name	all stations in domain			stations on Corsica		
	<i>MAE</i>	<i>NB</i>	<i>r</i>	<i>MAE</i>	<i>NB</i>	<i>r</i>
AWM 00-3	0.38	0.86	0.51	7.79	2.47	0.69
AWM 21-3	0.41	1.30	0.57	5.47	1.69	0.66
AWM 18-3	0.46	1.45	0.48	4.86	1.37	0.56
AWM 00-6	0.37	0.84	0.51	7.71	2.40	0.67
AWM-18-6	0.49	1.56	0.47	5.20	1.55	0.65
ARP 00-6	0.41	0.84	0.42	2.47	0.69	0.82
ARP 18-6	0.52	1.54	0.43	3.33	0.74	0.76
ECM 00-6	0.34	0.37	0.29	3.57	0.28	0.69
ECM 18-6	0.67	2.04	0.38	5.11	1.58	0.61

Table 6.1: Mean absolute error (*MAE*), normalized bias (*NB*), and Pearson’s product-moment coefficient *r* for the initial condition ensemble members and rain gauges for the 23 October 00 to 12 hour accumulated precipitation.

Moreover, Fig. 6.16a and Tab. 6.1 reveal that over the entire domain, all other simulations outperform the chosen reference simulation. However, due to its outstanding performance over Corsica, this did not affect the choice.

6.8 Conclusions

The localized HPE of 23 October 2012 in Corsica was simulated using the Meso-NH model. Tests show that simulations initialized with different input data sets are all able to accurately capture the large scale features of the event. All members of this initial condition ensemble capture the precipitation band over the sea west of Corsica. However, the placement of the heavy precipitation zone around Porto-Vecchio shows a high sensitivity to both input data set and initialization time. All nine simulations capture the northerly flow in the boundary layer to a certain extent. Unless the conditions are perturbed by spurious or overestimated convection as in the simulations initialized from AROME WMed data, flow splitting around Corsica persists until the onset of a HPE over the south of Corsica. All

simulations produce precipitation over or close to the south of Corsica. However, only one out of nine simulations, **EC 18-6** performs well in terms of both timing and location of the precipitation. Like Ducrocq et al. (2002) and Fresnay et al. (2012), this study shows the great importance of well captured initial conditions. For this event, they were the most important factor for good accuracy.

Increasing the resolution does not clearly improve the simulation results for the presented case. Compared to observations, some features of the precipitation field improve (spurious maximum reduced) while other features (localization, timing, cell size) deteriorate. The grid spacing of 500 m is in a gray zone where turbulence parametrizations are not designed to operate, results must therefore be interpreted with caution. A comparison of two different mixing length formulations, BL89 and DEAR, yields no conclusive result as to which of the two formulations is better suited for operation at 500 m for this particular event. While none of the two tested mixing length formulations is designed to operate at 500 m horizontal grid spacing, both are able to produce reasonable results.

A second ensemble is obtained by adding random perturbations to model physics. The spread of the resulting model physics ensemble is less than the spread of the initial condition ensemble. None of the ensemble members misplaced the precipitation maximum over southeastern Corsica. However, sensitivity to microphysics was higher over the sea west of Corsica. Like in the 500 m simulations, the cells within the convective band react differently to changes in model physics while the system as a whole does not change notably. The model physics ensemble indicates that the maximum over southeastern Corsica was closely linked to orographic effects.

A test with flattened orography over Corsica causes the precipitation to be placed along a more continuous band with lower precipitation values. The maximum over the southeast disappears, showing the important role of orography in

the HPE of 23 October. A second test with modified orography blocks the inflow of cold air into the western Mediterranean basin by increased topography height in Italy north and northeast of Corsica. This change causes the system to remain stationary almost twice as long as in the reference simulation. With the inflow of cold air suppressed, the event is fed more by easterly winds which advect highly buoyant air from the Tyrrhenian sea between Italy, Corsica and Sardinia. The drastic increase in simulated precipitation shows the importance of the gap flows and the effect of cooling in the upstream region of the event. While the flow splitting is not drastically modified in the **block** simulation, the precipitation increases by over 100%.

The above studied case has proven to be very interesting and yields important insight into the way, processes can interact on different scales. While all the involved mechanisms (synoptic forcing, low level convergence, flow splitting) are relatively well understood, their interaction is still difficult to forecast and subject to many uncertainties. For the specific event, processes from multiple scales interacted to form a damaging localized HPE. The western Mediterranean was influenced by a relatively weak cut-off low over the Balearic islands. Even though its surface pressure signal caused less than 3 hPa sea level pressure difference between its core and all adjacent coasts, the high to its north induced gap flows over the orography along the northern coasts and over Italy. To the east over the Balkan, a trough was favoring northerly flow, possibly contributing to the gap flows. Between the cut-off low to the west and the trough to the east, the large scale forcing was comparatively weak. Thus, northerly low level winds occurred where one would often see southeasterly wind in a typical event. Aloft, the southeasterly wind was forced by the cut-off low, causing strong vertical wind shear.

The northerly flow was forced around the orography of Corsica, splitting to its north and converging over its south. The western branch was strengthened by the

outflow of convection over the sea west of Corsica, which was deflected south by the orography. With the presence of moisture and instability southeast of Corsica, the convergence of the two branches of the split flow provided sufficient lift to initiate convection. Since the first convection in both, model and observation, occurred over the south of Corsica, orographic lift might also have been involved. The resulting convective event remained stationary due to a combination of stationary lee side convergence and upper level wind, which moved triggered cells northwest over the island, where they dissipated without perturbing the convergence line.

The event shows not only the complexity which can arise during HPEs, but also how difficult it can be to obtain good initial conditions for regional models, since two of three input data sets and eight out of nine simulations in the initial condition ensemble missed either timing or location of the HPE or even both. Model initial conditions clearly are the most important factor for capturing this event. This further highlights the necessity of good operational analyses. The fact that the best results were obtained with the ECMWF analyses and not the high-resolution AROME WMed reanalyses should not be considered as a consolidated result as further improvement is expected from the on-going second HyMeX reanalysis which will take full benefit of the field campaign observations.

Chapter 7

Conclusions and Outlook

This thesis takes a detailed look at the mechanisms of heavy precipitation events over Corsica. Here, a condensed and sorted overview over the results obtained in the previous chapters is presented. Firstly, the findings of the climatology are summed up. After that, the results of the case studies are presented, separated into mechanisms of HPEs themselves and findings regarding the simulations and the model. Lastly, the section provides an overview of possible follow-up studies, which will deepen our understanding of the subject at hand.

7.1 Results

7.1.1 Climatology and Clustering

Chapter 2 presents a classification of HPEs on Corsica based on a 31 year sample of HPEs ($>100 \text{ mm day}^{-1}$). The classification is based on a principal component analysis of data obtained by calculating the EOFs for geopotential and equivalent potential temperature on a domain over the western Mediterranean sea. In addition, the precipitation distribution on Corsica is analyzed for the obtained clusters.

- The results in Chapter 2 reveal that Corsica is hit by an average of 5.6 HPEs per year. These HPEs occur predominantly during autumn and early winter with 55% of the events being observed from October to December and 19.6% in October, the most active month.
- The majority of events is linked to a cyclone west of Corsica at the surface and either a trough or a cut-off west of Corsica. Such situations favor the advection of warm and moist air from the Tyrrhenian sea southeast of Corsica toward the Corsican orography.
- Three well distinguishable clusters were identified, which correspond to an autumn, winter and mixed cluster. The autumn cluster shows the strongest seasonal peak of all three clusters in September and October while the mixed cluster is relatively evenly distributed from October to May. The events in the mixed cluster show the highest average precipitation but the lowest maximum precipitation. The highest maximum precipitation is found in the autumn cluster, which is also the cluster with the highest θ_e values and whose events take place over the highest SSTs.
- The mixed cluster is the cluster with the largest low pressure systems, whereas the winter cluster cyclones are mostly limited to the Mediterranean. The averaged fields of each cluster are all associated with a trough of variable depth, whose axis lies over western France and eastern Spain.
- The winter cluster shows the strongest east-west difference in precipitation distribution over Corsica, concentrating its precipitation mainly over the orography over the eastern half of Corsica. This indicates higher stability and thus less convection upstream of the mountains.

- The autumn cluster shows slightly higher precipitation over the western half of Corsica, but still places most of it over the eastern half. Compared to the winter cluster, the autumn cluster places more of its precipitation directly along the coast, upstream of the orography, indicating a lower fraction of the precipitation is directly linked to orographic lifting but found farther upstream due to convection.
- The larger cyclones of the mixed cluster, which are on average located further north, induce a mean westerly flow over Corsica. Consequently, it is the only cluster which does not concentrate the heaviest precipitation over the eastern half of the island. Instead, it shows the strongest precipitation over the orography of the island and low values all along the coasts.

In summary, the highly unstable autumn events tend to hit the east coast and the orography further inland, whereas more stable events in the winter primarily hit the orography but not the coast. Larger scale events force westerly flow over most of the western Mediterranean, including Corsica, causing mainly orographic precipitation throughout the colder season.

7.1.2 Results of the Case Studies

The Three Cases in the Context of the Climatology

Three case studies are presented in this work, representing different classes of HPEs. Case 1, 4 September 2012, is characterized by an almost stationary synoptic situation and a slow moving surface cyclone and cut-off southeast of Corsica. It has the highest duration of all studied cases (>30 hours) and falls into the autumn cluster. Case 2, 31 October 2012, falls into the winter cluster. It was caused by a fast moving cyclone which moved from north of the Balearic islands over the north of Corsica on toward northern Italy, first causing precipitation along the

orography over eastern Corsica and later over the orography inland of the west coast. The first phase of the case 4 October corresponds closely to what is seen for the mean fields of the winter cluster, i.e. primarily southeasterly advection of moist air toward the east coast of Corsica. As the cyclone approaches the north of the island, the conditions start to resemble the mean θ_e and wind fields of the mixed cluster, demonstrating one of the problems of the clustering, namely the ambiguous classification of transient events. The third case, 23 October 2012, was not detected by the method used in Chapter 2. It was a highly localized event caused by a combination of large scale convergence ahead of an approaching cyclone and lee side convergence of northerly split flow around the island. The resulting convective line remained stationary for around three hours, depositing over 150 mm of precipitation over an area of less than 100 by 30 km, hardly affecting the rest of the island.

Mechanisms in HPEs

- All three HPEs are the result of interaction between warm, moist low level advection, the orography on Corsica, and a cyclone in the vicinity of the island. While cases 1 and 2 are directly linked to orographic lifting, case 3 is caused by convection due to a convergence zone over the sea.
- In cases 1 and 2, where orographic lifting is the direct cause of a large part of the precipitation, the most intense rain was observed over the mountains of the island, primarily over the eastern half of the island. As a result, the precipitation distribution in cases 1 and 2 is directly linked to the orography and the highest values are found over higher terrain.

- In case 3, where convergence over the sea is the primary lifting mechanism, the rain shows no distinct correlation with the orography. Instead, its position depends on the position of the convergence zone.

The three cases also pose different challenges to the weather model. While cases 1 and 2 mainly rely on an accurate representation of the orographic lifting process, case 3 relies on an accurate positioning of the convergence zone, which is inherently more difficult.

- For cases 1 and 2 and at 2.5 km horizontal grid spacing, the model has difficulty to accurately place the precipitation along the coast and above the mountains of the island. During the phases of easterly wind toward the mountains of Corsica, the bulk of the precipitation shows a downstream, i.e. westward, shift. These are cases for which the correct combination of instability, mountain height and wind speed is essential for good placement of the precipitation.
- A decrease of horizontal grid spacing from 2.5 km to 500 m overcompensates the downstream displacement, shifting too much of the precipitation upstream over the sea. Despite this problem, the 500 m simulations produce a more realistic precipitation field by better representing terrain shading and the spatial scale of the precipitation features themselves.
- In case 3, where convergence over the sea is the primary mechanism, the simulation results are extremely sensitive to the initial conditions, such that only one out of nine simulations of the initial condition ensemble is capable of capturing the HPE. On the other hand, changes in physical parametrization and horizontal grid spacing have little impact on the placement of the HPE, showing the importance of well captured initial conditions for cases which rely upon processes over the sea.

If the location of lifting is determined by orography, the model configuration is essential for a successful placement while over the sea initial conditions are more important. As a result, a reliable improvement of mesoscale precipitation forecasts requires both, sufficient resolution and good observational coverage of the upstream conditions. Along coasts, this includes knowledge of the state of the atmosphere over the sea, which is still a problem nowadays due to sparse observations. However, efforts are under way to alleviate the problem. In the near future, a second radar will be deployed in Ajaccio, at the west coast of Corsica. In addition, the lightning observation network SAETTA aims for permanent operation. These new additions to the operational observation network will make Corsica a highly attractive location for further case studies.

7.2 Outlook

Based on the results presented above, a number of follow-up research paths are available. The climatology of rainfall was based on a restrictive definition of HPE ($>100 \text{ mm day}^{-1}$ from 06 to 06 UTC). Generally a more sophisticated definition of HPE is desirable, such as using a minimum threshold of the hourly observed precipitation and defining an HPE as a minimum number of consecutive hours above the threshold. This would not only allow to detect HPEs longer than 24 hours but also to obtain a statistic of the duration and total precipitation of HPEs as well as detecting HPEs which are split over two 24 h measurement periods. In addition, the EOFs can be based on other variables than only geopotential and θ_e . While clustering based either purely on θ_e or purely on geopotential was tested, the results were not presented in detail. The impact of the domain used for the calculation was not presented either. All of these could potentially yield additional information and allow to differentiate better between classes of HPEs.

The results of the case studies pose a series of additional questions. In the context of current mesoscale modeling the most pressing issue is the question about horizontal grid spacing. The increasing availability of computational resources allows more operational models to run in the gray zone while the related questions have not been answered. It is generally assumed that the models perform sufficiently well even when quantities like the subgrid TKE produce unacceptable values (see, e.g. Bryan et al., 2003). Limited area models will operate in the grid spacings of the terra incognita for years to come. Considering the unequal distribution of resources, many countries' weather services will not be able to circumvent the problems of the gray zone by running LES simulations, probably for decades. Once limited area models can reasonably be run in LES mode, continental and even global models will eventually run into the same problems. In the light of this, waiting for the problem to solve itself does not appear to be a reasonable solution, and research on new parametrizations could greatly benefit the modeling community.

The results in this work show that problems seen at 2.5 km (in this case the downstream displacement of orographic precipitation) can be addressed by increasing the horizontal resolution or increasing the orography height. Even if such resolutions are not considered optimal, this work shows that they have the potential to solve the most pressing issues, namely the precise placement of precipitation for the purpose of flood and severe weather warnings. Several methods of generating the model orography could be tested for a number of different events and geographical settings to find an optimal configuration. The problem of sparse observations over the sea can only be addressed by extended field campaigns which provide the measurements necessary. Ideally, measurements should be available at all altitudes of the troposphere, as densely spaced as possible, but the boundary layer is the most crucial part. Satellite measurements are already filling this gap

7.2. OUTLOOK

to a certain extent, and they are widely used in operational analyses. However, especially case 3 shows that the conditions are not known accurately enough to predict events which are linked to mesoscale distributions of wind, temperature and moisture over the sea. Lastly, case 3 showed an interesting mechanism for the triggering and sustaining of convection, namely lee side convergence. The findings from Scheffknecht et al. (2016) have led to the development of idealized simulations which test the capability of downstream convergence behind an elliptical mountain to trigger and sustain deep moist convection. While these tests are not presented in the scope of this manuscript, they are scheduled as part of the follow-up work.

Résumé de la conclusion en français

Au cours de ce travail les épisodes météorologiques conduisant à de fortes précipitations en Corse ont été analysés en détail. Nous résumons ci-dessous les principaux résultats issus de notre étude climatologique d'une part et de nos trois cas d'études d'autre part. Pour conclure, nous discutons des perspectives de nos travaux.

Climatologie et classification des épisodes précipitants

Une classification des événements conduisant à de fortes pluies Corse a été effectuée. Celle-ci a reposé sur une analyse des composantes principales des champs météorologiques de la zone méditerranéenne auxquelles ont été appliqué un algorithme de classification. Cette étude a mis en évidence les résultats suivants:

- En moyenne la Corse subit 5 à 6 épisodes de fortes précipitations par an. Ces événements se produisent principalement en automne et en début d'hiver. 55% des événements surviennent d'octobre à décembre, octobre étant le mois le plus actif avec 19.6% des événements.

- La plupart des évènements sont associés à une dépression de surface et un talweg ou une goutte froide d'altitude positionnés à l'ouest de l'île. De telles conditions favorisent l'advection d'air chaud et humide depuis la mer Tyrrhénienne en direction du relief corse. C'est principalement l'est de la Corse qui est affecté par les fortes précipitations.
- Trois groupes d'évènements bien distincts ont été identifiés par l'algorithme de classification. Les deux premiers référencés comme groupe d'automne et groupe d'hiver exhibent un pic marqué à la saison correspondante alors que le troisième référencé comme groupe mixte est présent tout au long de l'année à l'exception des mois d'été.
- C'est dans le groupe d'hiver qu'on trouve les précipitations moyennes les plus fortes mais dans le groupe d'automne qu'on observe les précipitations maximales les plus intenses et que se trouvent donc les situations les plus dangereuses.
- Le groupe d'automne contient les évènements associées aux températures de surface de la mer les plus élevées. Les précipitations maximales se produisent sur les reliefs mais aussi à la côte suggérant la présence de convection en amont du relief. Par contre, les précipitations du groupe d'hiver sont principalement localisées sur les pentes est du relief suggérant une contribution plus importante du soulèvement orographique.
- Le groupe mixte est caractérisé par un vent du sud-ouest qui vient se heurter à l'orographie de la Corse. Il est associé à un système dépressionnaire plus vaste en partie localisé sur l'Atlantique. Les membres du groupe mixte ont une plus forte variabilité. Les précipitations se trouvent principalement sur les sommets, suggérant que ce groupe est composé d'évènements avec peu d'instabilité et une direction du vent plus variable.

Études de cas

Les trois cas analysés dans cette thèse correspondent à des situations météorologiques contrastées. Le premier cas d'étude (4 septembre 2012) est associé à une dépression quasi-stationnaire et correspond à une situation classique du groupe d'automne. Il a généré de très fortes précipitations principalement le long de la côte est de l'île. Le deuxième épisode (31 octobre 2012) est associée à une dépression qui s'est rapidement déplacée depuis les îles Baléares jusqu'à la Corse. Il est identifié par l'algorithme de classification comme appartenant au groupe d'hiver. Toutefois du fait du caractère très évolutif de la situation, il n'en possède pas toutes les caractéristiques. Ceci révèle une faiblesse de notre méthodologie pour les situations très non stationnaires. Enfin le cas du 23 Octobre 2012 correspond à un épisode de convection profonde quasi-stationnaire qui s'est développée sur une ligne de convergence située en mer au sud-ouest de la Corse. Le caractère très local de la zone précipitante ainsi que la chronologie de l'évènement (à cheval sur 2 journées) font qu'il n'est pas détecté par l'algorithme. Il possède néanmoins les caractéristiques du groupe d'automne.

Le modèle numérique Mésos-NH s'est montré globalement capable de simuler l'intensité et l'évolution générale des trois évènements discutés ci-dessus. Toutefois pour les deux premiers épisodes les résultats montrent un manque de précision quant à la localisation des précipitations et à leur positionnement vis à vis du relief. Plus spécifiquement, alors que les pluies observées sont concentrées à la côte, les pluies simulées sont décalées à mi-pente. Ce problème est corrigé tant dans les simulations à haute résolution que dans les simulations qui décrivent mieux la pente mais toutefois un trop puisqu'elles tendent à placer les précipitations en amont de la côte.

Les résultats obtenus pour le cas du 23 Octobre illustrent clairement la faible prévisibilité de certains épisodes. Parmi les 9 simulations réalisées pour cet épisode une seule est capable de reproduire correctement la localisation et la chronologie des précipitations. L'analyse des résultats a néanmoins permis de mettre en évidence un mécanisme déclencheur propre au caractère insulaire. Celui-ci fait intervenir la déviation de l'écoulement de basse couche de part et d'autre du relief et sa convergence à l'aval de l'obstacle.

Perspectives

À partir des résultats présentés ci-dessus, plusieurs perspectives de travail sont possibles. L'étude climatologique effectuée repose sur un critère trop restrictif (au moins une observation >100 mm jour⁻¹ dans la période allant 06 à 06 UTC le jour suivant). Ce choix a été contraint par le nombre et la nature des observations disponibles. Un critère plus élaboré fondé sur l'utilisation des précipitations horaires serait souhaitable. Il permettrait notamment de mieux caractériser la durée de l'épisode pluvieux ainsi que son rapport intensité/durée. En Corse, le nombre de stations horaires disponibles est clairement insuffisant pour une telle approche mais une méthode combinant les observations des stations horaires aux estimations radar mériterait d'être explorée.

L'analyse des résultats obtenus pour les trois situations étudiées soulève de multiples questions. Dans le contexte actuel des simulations à meso-échelle l'accroissement de la maille horizontale pose un problème. Bien que les modèles soient fréquemment utilisés avec des mailles comprises entre 2 km et 100 m, les paramétrisations qui gèrent la turbulence n'ont pas été conçues pour ces résolutions et sont utilisées loin de leur domaine d'application. Différentes pistes d'amélioration ont été récemment proposées dans la communauté Meso-NH et évaluées à partir

d'une référence de type LES obtenues sur des situations idéalisées. Les épisodes corses constitueraient un excellent banc d'essai pour tester en vraie grandeur les améliorations proposées.

Enfin l'analyse du cas de 23 octobre 2012 a mis l'accent sur un nouveau mécanisme pour la formation de la convection profonde stationnaire. Dans le cadre d'un stage effectué à Montréal, une série d'expériences idéalisées a été effectuée pour tester dans quelles conditions ce type de convection est possible et quels en sont les paramètres directeurs. Bien que les résultats de ces expériences ne soient pas présentés dans cette thèse, ils sont prévus comme une piste de travail à approfondir.

Bibliography

- Alpert, P., Neeman, B., and Shay-El, Y. (1990). Climatological analysis of mediterranean cyclones using ecmwf data. *Tellus A*, 42(1):65–77.
- Barthlott, C. and Kirshbaum, D. J. (2013). Sensitivity of deep convection to terrain forcing over mediterranean islands: Sensitivity of deep convection to terrain forcing. *Quart. J. Roy. Meteor. Soc.*, 139:1762–1779.
- Bjerknes, J. (1919). On the structure of moving cyclones. *Mon. Wea. Rev.*, 47(2):95–99.
- Bjerknes, J. and Holmboe, J. (1944). On the theory of cyclones. *Journal of Meteorology*, 1(1):1–22.
- Bjerknes, J. and Solberg, H. S. (1921). *Meteorological conditions for the formation of rain.* na.
- Bjerknes, J. and Solberg, H. S. (1922). *Life cycle of cyclones and the polar front theory of atmospheric circulation.* Grondahl.
- Bjerknes, V. (1916). *Über Wellenbewegung in kompressiblen schweren Flüssigkeiten.* B. G. Teubner.
- Blanchet, J., Molinié, G., and Touati, J. (2016). Spatial analysis of trend in extreme daily rainfall in southern france. *Climate Dynamics*, pages 1–14.

- Bougeault, P. and Lacarrère, P. (1989). Parameterization of Orography-Induced Turbulence in a Mesobeta-Scale Model. *Mon. Wea. Rev.*, 117:1872–1890.
- Bryan, G. H., Wyngaard, J. C., and Fritsch, J. M. (2003). Resolution Requirements for the Simulation of Deep Moist Convection. *Mon. Wea. Rev.*, 131:2394–2416.
- Buzzi, A., Tartaglione, N., and Malguzzi, P. (1998). Numerical Simulations of the 1994 Piedmont Flood: Role of Orography and Moist Processes. *Mon. Wea. Rev.*, 126:2369–2383.
- Campins, J., Genovés, A., Picornell, M., and Jansà, A. (2011). Climatology of mediterranean cyclones using the era-40 dataset. *International Journal of Climatology*, 31(11):1596–1614.
- Charney, J. G. (1947). The dynamics of long waves in a baroclinic westerly current. *J. Meteorol.*, 4(5):136–162.
- Charney, J. G. (1949). On a physical basis for numerical prediction of large-scale motions in the atmosphere. *J. Meteorol.*, 6(6):372–385.
- Charney, J. G. and Eliassen, A. (1949). A numerical method for predicting the perturbations of the middle latitude westerlies. *Tellus*, 1(2):38–54.
- Charney, J. G., Fjörtoft, R., and Neumann, J. v. (1950). Numerical integration of the barotropic vorticity equation. *Tellus*, 2(4):237–254.
- Cuxart, J., Bougeault, P., and Redelsperger, J.-L. (2000). A turbulence scheme allowing for mesoscale and large-eddy simulations. *Quart. J. Roy. Meteor. Soc.*, 126:1–30.
- Davolio, S., Mastrangelo, D., Miglietta, M. M., Drofa, O., Buzzi, A., and Malguzzi, P. (2009). High resolution simulations of a flash flood near Venice. *Nat. Hazards Earth Sys. Sci.*, 9:1671–1678.

- Davolio, S., Volonté, A., Manzato, A., Pucillo, A., Cicogna, A., and Ferrario, M. (2016). Mechanisms producing different precipitation patterns over north-eastern Italy: insights from Hymex-Sop1 and previous events. *Quarterly Journal of the Royal Meteorological Society*.
- Deardorff, J. W. (1972). Theoretical expression for the countergradient vertical heat flux. *J. Geophys. Res.*, 77:5900–5904.
- Doswell, C. A. (1987). The Distinction between Large-Scale and Mesoscale Contribution to Severe Convection: A Case Study Example. *Weather and Forecasting*, 2:3–16.
- Doswell, C. A., Brooks, H. E., and Maddox, R. A. (1996). Flash Flood Forecasting: An Ingredients-Based Methodology. *Weather and Forecasting*, 11:560–581.
- Doswell, C. A., Ramis, C., Romero, R., and Alonso, S. (1998). A Diagnostic Study of Three Heavy Precipitation Episodes in the Western Mediterranean Region. *Weather and Forecasting*, pages 102–124.
- Drobinski, P., Ducrocq, V., Alpert, P., Anagnostou, E., Béranger, K., Borga, M., Braud, I., Chanzy, A., Davolio, S., Delrieu, G., et al. (2014). Hymex: a 10-year multidisciplinary program on the Mediterranean water cycle. *Bulletin of the American Meteorological Society*, 95(7):1063–1082.
- Ducrocq, V., Braud, I., Davolio, S., Ferretti, R., Flamant, C., Jansa, A., Kalthoff, N., Richard, E., Taupier-Letage, I., Ayrat, P., Belamari, S., A., B., Borga, M., Boudevillain, B., Bock, O., Boichard, J.-L., Bouin, M.-N., Bousquet, O., Bouverier, C., Chiggiato, J., Cimini, D., Corsmeier, U., Coppola, L., Cocquerez, P., Defer, E., Delanoë, J., Di Girolamo, P., Doerenbecher, A., Drobinski, P. and Dufournet, Y., Fourrié, N., Gourley, J., Labatut, L., Lambert, Le Coz, J., Marzano,

- F., Molinié, G., Montani, A., Nord, G., Nuret, M., Ramage, K., Rison, B., Rous-sot, O., Saïd, F., Schwarzenboeck, A., Testor, P., Van Baelen, J., Vincendon, B., Aran, M., and Tamayo, J. (2014). HyMeX-SOP1, the field campaign dedicated to heavy precipitation and flash-flooding in the northwestern Mediterranean. *Bull. Amer. Meteor. Soc.*, 95:1083–1100.
- Ducrocq, V., Nuissier, O., Ricard, D., Lebeaupin, C., and Thouvenin, T. (2008). A numerical study of three catastrophic precipitating events over southern France. II: Mesoscale triggering and stationarity factors. *Quart. J. Roy. Meteor. Soc.*, 134:131–145.
- Ducrocq, V., Ricard, D., Lafore, J.-P., and Orain, F. (2002). Storm-scale numerical rainfall prediction for five precipitating events over France: On the importance of the initial humidity field. *Weather and Forecasting*, 17:1236–1256.
- Duffourg, F. and Ducrocq, V. (2011). Origin of the moisture feeding the heavy precipitating systems over southeastern France. *Nat. Hazards Earth Sys. Sci.*, 11(4):1163–1178.
- Durrán, D. R. (1990). *Atmospheric processes over complex terrain: [outgrowth of the Workshop on Atmospheric Processes over Complex Terrain, sponsored by the American Meteorological Society, in Park City, Utah from 24 - 28 October 1988]*, chapter Mountain Waves and Downslope Winds. Meteorological monographs. American Meteorological Society.
- Durrán, D. R. and Gingrich, M. (2014). Atmospheric Predictability: Why Butterflies Are Not of Practical Importance. *J. Atmos. Sci.*, 71(7):2476–2488.
- Egger, J. (1988). Alpine lee cyclogenesis: Verification of theories. *J. Atmos. Sci.*, 45(15):2187–2203.

- Ehmele, F., Barthlott, C., and Corsmeier, U. (2015). The influence of Sardinia on Corsican rainfall in the western Mediterranean Sea: A numerical sensitivity study. *Atmos. Res.*, 153:451–464.
- Ferretti, R., Low-Nam, S., and Rotunno, R. (2000). Numerical simulations of the Piedmont flood of 4-6 November 1994. *Tellus A*, 52:162–180.
- Fouquart, Y. and Bonnel, B. (1980). Computations of solar heating of the earth’s atmosphere: A new parameterization. *Beitr. Phys. Atmos.*, 53:35–62.
- Fresnay, S., Hally, A., Garnaud, C., Richard, E., and Lambert, D. (2012). Heavy precipitation events in the Mediterranean: sensitivity to cloud physics parameterisation uncertainties. *Nat. Hazards Earth Sys. Sci.*, 12:2671–2688.
- Froidurot, S., Molinié, G., and Diedhiou, A. (2016). Climatology of observed rainfall in southeast France at the regional climate model scales. *Climate Dynamics*, pages 1–19.
- Gao, X., Pal, J. S., and Giorgi, F. (2006). Projected changes in mean and extreme precipitation over the Mediterranean region from a high resolution double nested rcm simulation. *Geophys. Res. Lett.*, 33(3):n/a–n/a. L03706.
- Grubišić, V., Sachsperger, J., and Caldeira, R. M. (2015). Atmospheric wake of Madeira: first aerial observations and numerical simulations. *Journal of the Atmospheric Sciences*, 72(12):4755–4776.
- Hally, A., Richard, E., and Ducrocq, V. (2014a). An ensemble study of HyMeX IOP6 and IOP7a: sensitivity to physical and initial and boundary condition uncertainties. *Nat. Hazards Earth Sys. Sci.*, 14:1071–1084.

- Hally, A., Richard, E., Fresnay, S., and Lambert, D. (2014b). Ensemble simulations with perturbed physical parametrizations: Pre-HyMeX case studies. *Quart. J. Roy. Meteor. Soc.*, 140:1900–1916.
- Hanley, K. E., Kirshbaum, D. J., Belcher, S. E., Roberts, N. M., and Leoncini, G. (2011). Ensemble predictability of an isolated mountain thunderstorm in a high-resolution model. *Quart. J. Roy. Meteor. Soc.*, 137(661):2124–2137.
- Hannachi, A., Jolliffe, I., and Stephenson, D. (2007). Empirical orthogonal functions and related techniques in atmospheric science: A review. *Int. J. Climatol.*, 27(9):1119–1152.
- Hartigan, J. A. and Wong, M. A. (1979). Algorithm as 136: A k-means clustering algorithm. *Journal of the Royal Statistical Society. Series C (Applied Statistics)*, 28(1):100–108.
- Haurwitz, B. (1940). The motion of atmospheric disturbances on the spherical earth. *J. mar. Res.*, 3(5):254–267.
- Holton, J. R. (2004). *An Introduction to Dynamic Meteorology, Volume 88, Fourth Edition (International Geophysics)*. Academic Press, 4 edition.
- Homar, V., Ramis, C., Romero, R., and Alonso, S. (2010). Recent trends in temperature and precipitation over the Balearic Islands (Spain). *Climate Change*, 98:199–211.
- Honnert, R., Masson, V., and Couvreur, F. (2011). A Diagnostic for Evaluating the Representation of Turbulence in Atmospheric Models at the Kilometric Scale. *J. Atmos. Sci.*, 68:3112–3131.
- Houze, R. A. (2012). Orographic effects on precipitating clouds. 50:RG1001.

- Jansa, A., Genoves, A., and Garcia-Moya, J. A. (2000). Western mediterranean cyclones and heavy rain. part 1: Numerical experiment concerning the piedmont flood case. *Meteorological Applications*, 7(4):323–333.
- Jansa, A., Genoves, A., Picornell, M., Campins, J., Riosalido, R., and Carretero, O. (2001). Western mediterranean cyclones and heavy rain. part 2: Statistical approach. *Meteorological Applications*, 8(1):43–56.
- Kain, J. (1993). Convective parametrization for mesoscale models: The kain-fritsch scheme. *Meteorological Monography*, 46:165–170.
- Kelley, C., Ting, M., Seager, R., and Kushnir, Y. (2012). Mediterranean precipitation climatology, seasonal cycle, and trend as simulated by cmip5. *Geophys. Res. Lett.*, 39(21):n/a–n/a. L21703.
- Kolmogorov, A. N. (1941). The local structure of turbulence in incompressible viscous fluid for very large reynolds numbers. In *Dokl. Akad. Nauk SSSR*, volume 30, pages 301–305. JSTOR.
- König, M., Schmetz, J., and Tjemkes, S. (1999). Satellite intercalibration of {IR} window radiance observations. *Advances in Space Research*, 23(8):1341 – 1348. Calibration and Characterization of Satellite Sensors.
- Kotroni, V., Lagouvardos, K., Kallos, G., and Ziakopoulos, D. (1999). Severe flooding over central and southern greece associated with pre-cold frontal orographic lifting. *Quart. J. Roy. Meteor. Soc.*, 125:967–991.
- Lafore, J. P., Stein, J., Asencio, N., Bougeault, P., Ducrocq, V., Duron, J., Fischer, C., Hérel, P., Mascart, P., Masson, V., Pinty, J. P., Redelsperger, J. L., Richard, E., and Vilà-Guerau de Arellano, J. (1998). The meso-NH atmospheric simulation system. part i: adiabatic formulation and control simulations. *Ann. Geophys.*, 16(1):90–109.

- Lambert, D. and Argence, S. (2008). Preliminary study of an intense rainfall episode in Corsica, 14 September 2006. *Adv. Geosciences*, 16:125–129.
- Lambert, D., Mallet, M., Ducrocq, V., Dulac, F., Gheusi, F., and Kalthoff, N. (2011). CORSiCA: a Mediterranean atmospheric and oceanographic observatory in Corsica within the framework of HyMeX and ChArMEx. *Adv. Geosciences*, 26:125–131.
- Langhans, W., Schmidli, J., and Schär, C. (2012). Bulk Convergence of Cloud-Resolving Simulations of Moist Convection over Complex Terrain. *J. Atmos. Sci.*, 69:2207–2228.
- Lascaux, F., Richard, E., and Pinty, J.-P. (2006). Numerical simulations of three different MAP IOPs and the associated microphysical processes. *Quart. J. Roy. Meteor. Soc.*, 132:1907–1926.
- Leutbecher, M. and Palmer, T. (2008). Ensemble forecasting. *Journal of Computational Physics*, 227(7):3515 – 3539. Predicting weather, climate and extreme events.
- Lin, Y.-L., Chiao, S., Wang, T.-A., Kaplan, M. L., and Weglarz, R. P. (2001). Some Common Ingredients for Heavy Orographic Rainfall. *Weather and Forecasting*, 16(6):633–660.
- MacQueen, J. (1967). Some methods for classification and analysis of multivariate observations. In *Proceedings of the Fifth Berkeley Symposium on Mathematical Statistics and Probability, Volume 1: Statistics*, pages 281–297, Berkeley, Calif. University of California Press.
- Maheras, P., Flocas, H., Patrikas, I., and Anagnostopoulou, C. (2001). A 40 year objective climatology of surface cyclones in the mediterranean region: spatial and temporal distribution. *International Journal of Climatology*, 21(1):109–130.

- Masson, V., Le Moigne, P., Martin, E., Faroux, S., Alias, A., Alkama, R., Belamari, S., Barbu, A., Boone, A., Bouyssel, F., Brousseau, P., Brun, E., Calvet, J.-C., Carrer, D., Decharme, B., Delire, C., Donier, S., Essaouini, K., Gibelin, A.-L., Giordani, H., Habets, F., Jidane, M., Kerdraon, G., Kourzeneva, E., Lafaysse, M., Lafont, S., Lebeaupin Brossier, C., Lemonsu, A., Mahfouf, J.-F., Marguinaud, P., Mokhtari, M., Morin, S., Pigeon, G., Salgado, R., Seity, Y., Taillefer, F., Tanguy, G., Tulet, P., Vincendon, B., Vionnet, V., and Voldoire, A. (2013). The SURFEXv7.2 land and ocean surface platform for coupled or offline simulation of earth surface variables and fluxes. *Geosci. Model Dev.*, 6(4):929–960.
- Mehta, A. V. and Yang, S. (2008). Precipitation climatology over mediterranean basin from ten years of trmm measurements. *Adv. Geosciences*, 17:87–91.
- Metzger, J., Barthlott, C., and Kalthoff, N. (2014). Impact of upstream flow conditions on the initiation of moist convection over the island of Corsica. *J. Atmos. Sci.*, 145-146:279–296.
- Miglietta, M. M. and Rotunno, R. (2005). Simulations of moist nearly neutral flow over a ridge. *J. Atmos. Sci.*, 62(5):1410–1427.
- Miglietta, M. M. and Rotunno, R. (2009). Numerical simulations of conditionally unstable flows over a mountain ridge. *J. Atmos. Sci.*, 66(7):1865–1885.
- Miglietta, M. M. and Rotunno, R. (2010). Numerical simulations of low-cape flows over a mountain ridge. *J. Atmos. Sci.*, 67(7):2391–2401.
- Miglietta, M. M. and Rotunno, R. (2014). Numerical Simulations of Sheared Conditionally Unstable Flows over a Mountain Ridge. *J. Atmos. Sci.*, 71(5):1747–1762.

- Mlawer, E. J., Taubman, S. J., Brown, P. D., Iacono, M. J., and Clough, S. A. (1997). Radiative transfer for inhomogeneous atmospheres: RRTM, a validated correlated-k model for the longwave. *J. Geophys. Res.*, 102:663–682.
- Morel, C. and Sényesi, S. (2002a). A climatology of mesoscale convective systems over europe using satellite infrared imagery. I: Methodology. *Quart. J. Roy. Meteor. Soc.*, 128:1953–1971.
- Morel, C. and Sényesi, S. (2002b). A climatology of mesoscale convective systems over europe using satellite infrared imagery. II: Characteristics of european mesoscale convective systems. *Quart. J. Roy. Meteor. Soc.*, 128:1973–1995.
- Nissen, K., Leckebusch, G., Pinto, J. G., Renggli, D., Ulbrich, S., and Ulbrich, U. (2010). Cyclones causing wind storms in the mediterranean: characteristics, trends and links to large-scale patterns. *Nat. Hazards Earth Sys. Sci.*, 10(7):1379–1391.
- Nuss, W. A. and Miller, D. K. (2001). Mesoscale predictability under various synoptic regimes. *Nonlinear Proc. Geoph.*, 8(6):429–438.
- Orlanski, I. (1975). A rational subdivision of scales for atmospheric processes. *Bulletin of the American Meteorological Society*, 56:527–530.
- Pichler, H., Steinacker, R., and Lanzinger, A. (1990). Cyclogenesis induced by the alps. *Meteorology and Atmospheric Physics*, 43(1-4):21–29.
- Pinty, J.-P. and Jabouille, P. (1998). A mixed-phase cloud parameterization for use in a mesoscale non-hydrostatic model: simulations of a squall line and of orographic precipitations. In *Tenth AMS Cloud Physics Conference*, pages 217–220, Everett, WA, USA. American Meteorological Society.

- Pontrelli, M. D., Bryan, G., and Fritsch, J. M. (1999). The Madison County, Virginia, Flash Flood of 27 June 1995. *Weather and Forecasting*, 14(3):384–404.
- Reinecke, P. A. and Durran, D. R. (2008). Estimating Topographic Blocking Using a Froude Number When the Static Stability Is Nonuniform. *J. Atmos. Sci.*, 65:1035–1048.
- Ricard, D., Ducrocq, V., and Auger, L. (2012). A Climatology of the Mesoscale Environment Associated with Heavily Precipitating Events over a Northwestern Mediterranean Area. *J. Appl. Meteor. Climatol.*, 51:468–488.
- Richardson, L. F. (1922). *Weather prediction by numerical methods*. Cambridge University Press, London.
- Rossby, C.-G. et al. (1939). Relation between variations in the intensity of the zonal circulation of the atmosphere and the displacements of the semi-permanent centers of action. *Journal of Marine Research*, 2(1):38–55.
- Rotunno, R. and Ferretti, R. (2001). Mechanisms of intense alpine rainfall. *Journal of the atmospheric sciences*, 58(13):1732–1749.
- Rysman, J.-F., Lemaître, Y., and Moreau, E. (2016). Spatial and temporal variability of rainfall in the alps–mediterranean euroregion. *Journal of Applied Meteorology and Climatology*, 55(3):655–671.
- Saunders, R., Matricardi, M., Brunel, P., English, S., Bauer, P., O’Keeffe, U., Francis, P., and Rayer, P. (2005). Rttov-8 science and validation report. *NWP SAF report, Met Office, Exeter, UK*.
- Schär, C. and Smith, R. B. (1993a). Shallow-water flow past isolated topography. part i: Vorticity production and wake formation. *Journal of the atmospheric sciences*, 50(10):1373–1400.

- Schär, C. and Smith, R. B. (1993b). Shallow-water flow past isolated topography. part ii: Transition to vortex shedding. *Journal of the atmospheric sciences*, 50(10):1401–1412.
- Scheffknecht, P., Richard, E., and Lambert, D. (2016). A Highly Localized High Precipitation Event over Corsica. *Quart. J. Roy. Meteor. Soc.*, pages n/a–n/a.
- Sénési, S., Bougeault, P., Chèze, J.-L., Cosentino, P., and Thépenier, R.-M. (1996). The Vaison-La-Romaine Flash Flood: Mesoscale Analysis and Predictability Issues. *Weather and Forecasting*, 11:417–442.
- Smith, R. B. (1989a). Hydrostatic airflow over mountains. *Adv. Geosciences*, 31:1–41.
- Smith, R. B. (1989b). Mountain-induced stagnation points in hydrostatic flow. *Tellus A*, 41(3):270–274.
- Tapiador, F. J., Tao, W.-K., Shi, J. J., Angelis, C. F., Martinez, M. A., Marcos, C., Rodriguez, A., and Hou, A. (2012). A Comparison of Perturbed Initial Conditions and Multiphysics Ensembles in a Severe Weather Episode in Spain. *J. Appl. Meteor. Climatol.*, 51(3):489–504.
- Taylor, K. E. (2001). Summarizing multiple aspects of model performance in a single diagram. *J. Geophys. Res.*, 106(D7):7183–7192.
- Thornes, J., Brandt, J., and Geeson, N. (1998). Mediterranean desertification.
- Trapero, L., Bech, J., Duffourg, F., Esteban, P., and Lorente, J. (2013). Mesoscale numerical analysis of the historical November 1982 heavy precipitation event over Andorra (Eastern Pyrenees). *Nat. Hazards Earth Sys. Sci.*, 13:2969–2990.
- Trigo, I. F., Bigg, G. R., and Davies, T. D. (2002). Climatology of cyclogenesis mechanisms in the mediterranean. *Monthly Weather Review*, 130(3):549–569.

Wilks, D. S. (2011). *Statistical methods in the atmospheric sciences*, volume 100. Academic press.

Wyngaard, J. (2004). Toward numerical modelling in the "Terra Incognita". *J. Atmos. Sci.*, 61:1816–1826.

Characterization of Heavy Precipitation on Corsica

by

Phillip SCHEFFKNECHT

Abstract

Heavy precipitation is one of the primal meteorological reasons for property damage, injuries, and deaths. In the framework of the Hydrological Cycle of the Mediterranean (HyMeX) program, heavy precipitation is analyzed throughout the entire Mediterranean basin with a special focus on the northwestern Mediterranean. This work studies in particular the mechanisms of high precipitation events (HPEs) on Corsica. For this purpose, a 31 year (1985 – 2015) climatology of HPEs on Corsica is presented. In addition, three HPEs during autumn 2012 are analyzed in detail using observations and numerical modeling.

A climatology of 173 events shows that the eastern half of Corsica, specifically the orography, is most affected by high precipitation events. The months from September to December, most of all October, are identified as most prone to heavy precipitation events over Corsica. A principal component analysis is used to classify the events into three categories, which correspond to warm autumn and cold winter Mediterranean cyclones as well as a mixed category which contains also larger scale Atlantic cyclones. The heaviest precipitation is observed when warm moist southeasterly flow encounters the Corsican orography.

In addition, three case studies are presented, each with different mechanisms involved. A stationary cyclone on 4 September 2012 led to widespread precipitation over Corsica with the most intense rain observed over the east of the island, along the coast and the orography. On 31 October, a fast moving cyclone caused a multi-phase event, which was characterized by low level wind turning from southeast to west while precipitation gradually changed from convective along the orography in the east of the island to stratiform mainly over the west and southwest. The last event, 23 October 2012, was comprised of a line convective cells which formed over stationary lee side convergence southeast of Corsica. The convective cells were advected toward the island by the mid- and upper level southeasterly wind. These conditions allowed the convective line to remain stationary, resulting in a highly localized and relatively short event.

The findings confirm that the numerical model Meso-NH is well capable of simulating such events with satisfactory precision at a grid spacing of 2.5 km. However, the studies also underline the importance of well captured initial conditions. Additionally, the spatial distribution of precipitation is highly dependent on the representation of the orography in the model as well as the horizontal grid spacing and is improved when using a horizontal grid spacing of 500 m instead.

Characterization of Heavy Precipitation on Corsica

par

Phillip SCHEFFKNECHT

Résumé

Les fortes précipitations sont parmi les phénomènes météorologiques les plus dangereux pouvant causer des dégâts matériels, des blessés et des morts. Le programme de recherche HyMeX (Hydrological cycle of the Mediterranean eXperiment) s'intéresse à leur étude sur le bassin méditerranéen et plus particulièrement sa partie nord occidentale. Les travaux réalisés dans le cadre de cette thèse ont porté en particulier sur l'étude des mécanismes associés aux événements de fortes précipitations (High Precipitation Events, HPE) se produisant en Corse. Une climatologie des HPE en Corse sur une durée de 31 ans a été réalisée ainsi que l'étude détaillée de trois HPEs de l'automne 2012 pendant la campagne de mesures d'HyMeX. Ces trois cas d'études sont abordés par le biais de l'analyse des données et par celui de la modélisation.

L'étude climatologique a montré que 173 HPEs (caractérisés par plus de 100 mm de précipitations en 24h) se sont produits en Corse sur la période 1985-2015. Ils sont principalement caractérisés par le fait qu'ils affectent plutôt la partie orientale de la Corse, plus particulièrement son orographie. Ces HPEs se produisent surtout de septembre à décembre avec un maximum en octobre. Une analyse en composantes principales a permis de classer ces événements en trois catégories. Les dépressions méditerranéennes chaudes d'automne, celles d'hiver froides, et une catégorie dite mixte associée aux dépressions atlantiques de grande échelle. Les précipitations les plus fortes sont observées quand l'orographie corse fait obstacle à un flux de sud-est chaud et humide.

Les cas d'études présentés sont tous les trois différents en terme de mécanismes impliqués. Le cas du 4 septembre 2012 est associé à une dépression stationnaire donnant des précipitations sur toute la Corse avec un maximum sur le littoral et le relief de l'est de l'île. Celui du 31 octobre correspond à une dépression se déplaçant rapidement et induisant une évolution en plusieurs phases associée à un flux de basse couche initialement de sud-est tournant à l'ouest, associé à des précipitations d'abord convectives le long du relief oriental puis évoluant au fur et à mesure en pluies stratiformes sur l'ouest et le sud-est de l'île. Le dernier cas, du 23 octobre, est composé d'une ligne de cellules convectives résultant d'une convergence stationnaire au sud-est, sous le vent de la Corse. Les cellules convectives sont advectées vers l'île par le flux de sud-est de moyenne et haute altitude. Cette configuration permet la stationnarité de la ligne convective, provoquant un épisode de précipitations relativement court et très localisé.

Les résultats de ce travail confirment que le modèle numérique Meso-NH permet de bien simuler ce type de phénomène avec une précision satisfaisante à une résolution horizontale de 2,5 km. Cependant, cette étude met également en évidence l'importance de la bonne représentation des conditions initiales. En outre, la distribution spatiale des précipitations dépend fortement de la représentation de l'orographie dans le modèle et de la résolution horizontale. Elle est améliorée quand on utilise une résolution de 500m.